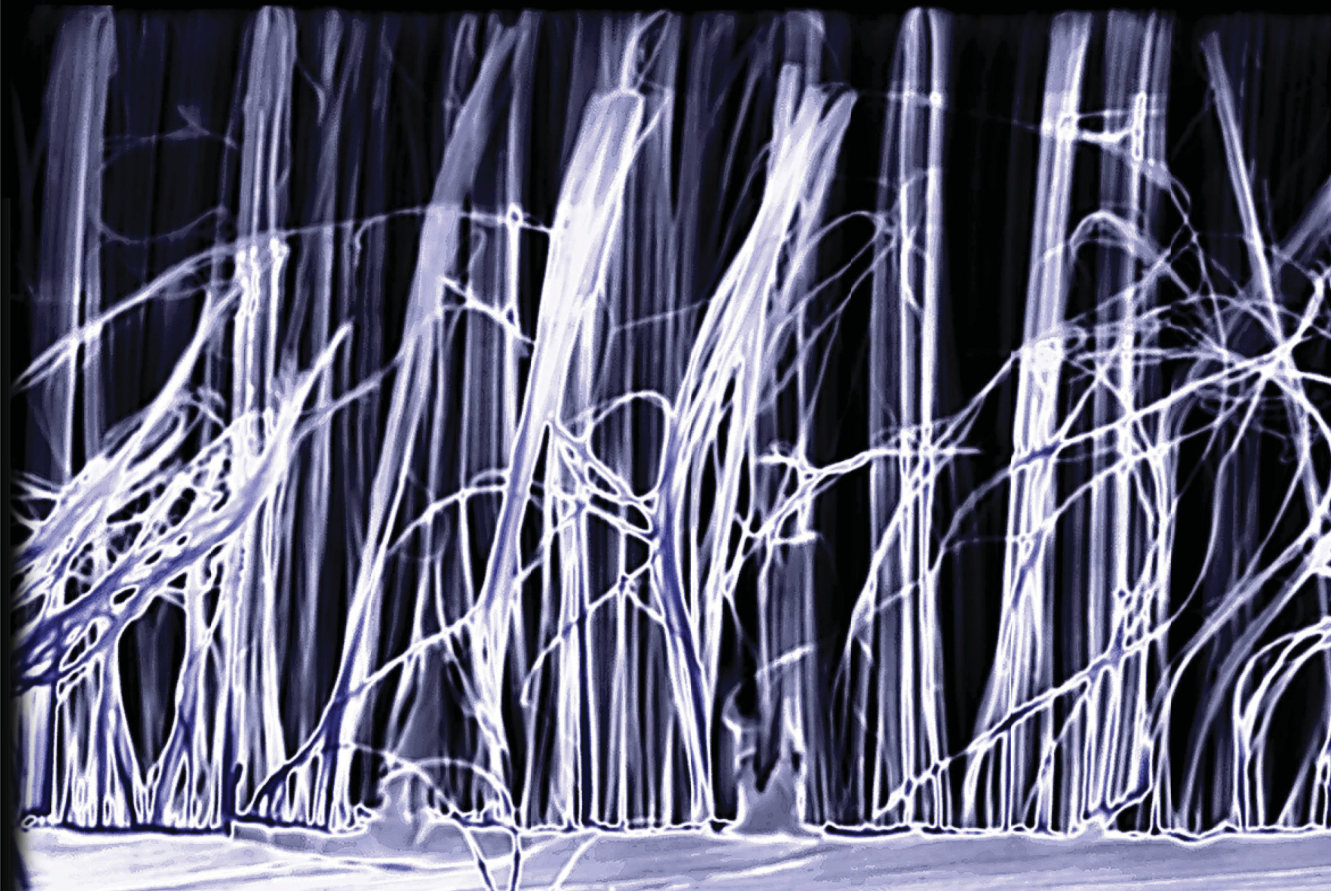Pietro Artoni

Silicon Nanowires by Metal Assisted Etching

Tutor: Chiar.mo Prof. Francesco Priolo
Supervisor: Dr. Alessia Irrera
Coordinatore: Chiar.mo Prof. Francesco Riggi

UNIVERSITÀ DEGLI STUDI DI CATANIA
DOTTORATO DI RICERCA IN FISICA - XXV CICLO

PIETRO ARTONI

Silicon Nanowires
by Metal Assisted Etching

TUTOR:

CHIAR.MO PROF. FRANCESCO PRIOLO

SUPERVISOR:

DOTT.SSA ALESSIA IRRERA

COORDINATORE:

CHIAR.MO PROF. FRANCESCO RIGGI

TESI PER IL CONSEGUIMENTO DEL TITOLO

Cover: Scanning Electron Microscopy (SEM) image of a cross section of Si nanowires fabricated by metal assisted etching.

A Laura e alla mia famiglia

Contents

Towards a nanoworld

In 1965, Gordon Moore, then director of the Fairchild Semiconductor's Research and Development Laboratories, first noted that the complexity of semiconductor chips has doubled every year since the first prototype integrated circuit was produced in 1959. This exponential increase in the number of components on a chip later became known as Moore's law, which has undergone several revisions over the decades. The time constant is nows 18 months, but Moore's law has gone from being the doubling of the number of transistors on a chip to the doubling of microprocessor power to the doubling of computing power at a fixed cost. After nearly 50 years, the information technology industry realizes that the end of Moore's law, whatever formulated, is on the horizon because of several physical limits. There are five different limits: fundamental, material, device, interconnections and system. Fundamental limits are imposed by the laws of physics and are thus absolute and independent of material properties, device structure, circuit configuration, or system architecture. Perhaps the most problematic of these limits is the fourth, i.e. interconnections. A significant performance limitation in integrated circuits has become the metal interconnect, which is responsible for depressing the on-chip data bandwith while consuming an increasing percentage or power. These problems will grow as wire diameters scale down and the resistance-capacitance product of the interconnect wires increases hyperbolically which threatens to choke off the computational performance increases of chips that we have come to expect over time. It is possible that computers in the future will be based on monolithically integrated nanoscale electronic/photonic circuits, with the information processing primarily relying on electrons and the majority of the information transfer

(above a particular architecture/dependent length scale measured in tens of micrometers) accomplished using photons. Such systems will be dramatically more capable and energy efficient than solely electronic systems. This is in general the dream of integrated photonics. Recent advances in the area of nanophotonics, such as photonic bandgap and negative index materials, have made possible the design and manufacture of integrated electronic photonic systems that utilize existing fabrication plants for silicon integrated circuits. If these systems can be realized, they have the potential to extend the 18-month doubling of computing capability at a fixed cost for many decades into the future. Such "photonic circuits" require different kind of materials for generating photons, controlling their flux and detecting them. Most of the material adopted are III-V or II-VI semiconductors, which are not fully compatible with Si technology. At the moment, only passive devices (i.e. waveguides or splitters) can be promptly made on Si, but the scenario concerning active devices (light sources or amplifiers) is still poor. Unfortunately bulk silicon is an inefficient light emitter, and despite the scientific results obtained with both optical gain and stimulated Raman emission, an electrically-driven laser in Si still doesn't exist. Hence, a nanostructured-silicon-based light emitter would be a natively integrable solution for photonic devices, and would be also cheaper than the III-V light sources adopted in contemporary integrated photonics. Fabricating, controlling and understanding a silicon nanowire system, its structure and its mechanisms of light emission are hence the main purposes of this thesis.

Outline of the thesis

Group-IV semiconductor nanowires (NWs) are attracting interest among the scientific community as building blocks for future nanoscaled devices. The aim of this thesis is to exploit a new method for Si NWs fabrication suitable for photonic applications, and to study the application of Si NWs in both photonics and optical trapping. Hopefully, all these three aims have been a scientific challenge for all the group I joined and for me. Silicon NWs are nowadays a promising system for both electronics and photonics. Let's consider that microelectronic industry recently moved to nanometric

processes, and the IC manufacturing roadmap set the length of the channel for ULSI to 14 nm in 2013. At the same time, this thesis demonstrates that Si NWs can have a big impact on silicon photonics, since they can emit light under both optical and electrical pumping. A prototype of light emitting device fully based on Si NWs has been fabricated, and it can emit light in the red at room temperature. Another part of the thesis is focused on the study of Si/Ge multi quantum well NWs, in which carriers can be both trapped in 2D Si whiskers and 3D Ge wells. The ending part of the thesis will be focused on optical trapping of Si NWs, and this study will confirm hypotheses on Si NWs hydrodynamics and on their brownian motion when they are dispersed into a liquid.

The thesis is organized as follows:

In **chapter 1** a broad discussion on the different top down and bottom up approaches on Si NWs fabrication will introduce us to the main peculiarities, issues and pros of each different approach, and the problems that will be encountered if trying to use these systems for photonic applications. Different techniques are currently used for Si NWs preparation, the bottom-up vapor-liquid-solid (VLS) mechanism or the top-down approach which uses the electron beam lithography (EBL). Moreover, literature shows that in the last few years Metal-assisted chemical etching (MACEtch) has become a powerful technique to obtain high density and low-cost Si NWs with high and controllable aspect ratio. It consists of an etching of a Si substrate in a solution containing dihydrogen peroxide, hydrogen fluoride and a metallic salt. Roughly speaking, the metal catalyzes the hole injection into the semiconductor, which is then oxidized, and subsequently removed by the hydrogen fluoride. The dihydrogen peroxide accelerates the process injecting more holes. NWs obtained by this technique have exactly the same structure and doping properties of the substrate; a size of 10 nm can be be obtained by using particular lithography techniques e.g. with anodized aluminum oxide masks (AAO). The fabrication of Si NWs can be aimed to several applications in different areas, such as field effect transistors for microelectronics, biological and chemical sensors, solar cells and photonics. Both their reduced size and high surface to volume ratio are fundamental for the first two ap-

plications respectively. High aspect ratio and randomness in the arrangement of the wires is a fundamental aspect to make solar cells in silicon nanowire attractive, because of their high absorption of light and their high capability to separate electron hole pairs before they are recombined. Anyway in this scenario a system which is natively suitable for photonics is still lacking. All the attempts made by oxidizing VLS grown or EBL made silicon nanowires are reported in this chapter, but with poor results. For these reasons MacEtch technique could be a valid candidate for making Si NWs of dimensions compatible with quantum confinement effects, with full controllable doping profile, which do not need any further oxidation to shrink the Si core size and where there is no gold diffusion (detrimental for optical properties) inside the NWs since the etching process is at room temperature.

Chapter 2 deals with the fabrication of ultrathin Si NWs by a modified metal assisted etching process. Instead of using metallic salts as catalysts (which leave metallic dendrites over the NWs after the etching process), ultrathin films of gold or silver have been evaporated at room termperature on a Si surface, and then etch is performed. Depending on the adopted substrate, vertical or tilted NWs can be obtained. Then, it will be shown that by using for the first time ultra thin films of gold or silver as catalysts for the etch, their main size becomes less than 10 nm, allowing quantum confinement effects. A Si core - SiO_2 shell structure is obtained and it is possible to tune the core of the NWs scaling them down to 5 nm. The size of the Si NWs scales down as the thickness of the metallic mesh (used as a catalyst for the etching process) becomes thicker. Both energy filtered TEM analyses and Raman analyses strictly confirm these data. Also, a more complex system has been realized, indeed by etching a multi quantum well made by stacks of 1 nm thick Ge and 54 nm thick Si it is possible to fabricate Si/Ge MQW NWs. In this way a structure made of Si NWs which confines carriers in two dimensions (leaving them free on the third one), and a structure of Ge disks (which confines carriers in three dimensions) can be obtained.

Chapter 3 is the demonstration that both MACetch Si NWs and Si/Ge MQW NWs are suitable for photonic applications. Obtaining

light from Si NWs at room temperature under optical and electrical pumping is still a big challenge and would have a tremendous impact on silicon photonics. It will be shown a detailed and complete study of the excitation and de-excitation properties as a function of the temperature and of the pump power, determining the excitation cross section, and both presence and origin of possible non-radiative phenomena. The influence of the structural properties on the mechanisms of light emission has been studied, in such a way to optimize the emission properties. A light emitting device based on Si NWs has been realized, showing the efficient electroluminescence emission at room temperature in the red (700 nm) under low voltage pumping. Finally, we realized Si/Ge NWs by the same synthesis approach, in order to obtain different confined structures of both Si and Ge inside each NW. Photoluminescence emission properties of Si/Ge NWs have been studied at room temperature.

Chapter 4 deals with the optical trapping of the single MACetch Si NW. Optical trapping (OT) of nanostructures has acquired tremendous momentum in the past few years. Manipulating nanoparticles with OT is generally difficult because radiation forces scale approximately with particle volume and thermal fluctuations can easily overwhelm trapping forces at the nanoscale. Hence, the role of size-scaling is crucial for understanding the interplay between optical forces and hydrodynamic interactions that change dramatically with size, therefore much affecting both force-sensing and spatial resolution in precision applications. A detailed study on how optical trapping and Brownian motion of very thin (7 ± 2 nm diameter) Si NWs depend on their size has been performed. The NWs length is the key parameter that regulates forces, torques, and hydrodynamics. The core of the chapter fully characterizes the three-dimensional translational and angular Brownian motion, deals with the measure of the root-mean-square displacements and shows the different size-scaling due to the interplay between radiation forces defining the trapping potential and hydrodynamics. Finally, a comparison with a full electromagnetic theory of optical trapping of SiNWs have been made, showing good agreement if aberration from the coverslip-water interface is considered.

x

Chapter 1

An Overview on Si NWs

Abstract

In this chapter a broad discussion on the state of the art of Si NWs realization and performances will be treated. First, different approaches of nanotechnology, i.e. the bottom-up and top-down approaches, will be shown. Then, how these paradigms can be focused on Si NWs realization will be elucidated. The most important bottom-up and top-down techniques of realization of Si NWs will be broadly discussed in the first section: the vapor liquid solid mechanism (VLS), the electron beam lithography and a special focus will be given on the metal assisted etching technique. This latter technique has been recently invented, and is promising since it is low cost, with a high throughput, and the process of fabrication is easy and controllable. The second section is then focused on the applications of these systems in different key areas of technology: sensors, nanoelectronics and solar cells. The world is changing, it continuously asks for energy, for faster electro-optical communication, and for safety and welfare. We will see how the specific physical and chemical peculiarities of Si NWs can make them unique and necessary for future applications in these key areas for the next years.
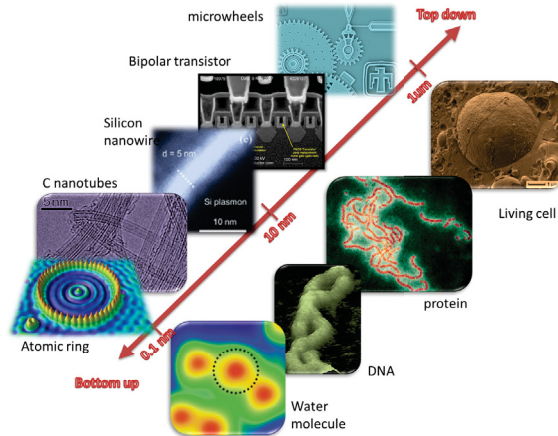
Figure 1.1: *Top-down and bottom-up strategies in both physical and life sciences.*

1.1 Bottom-up and top-down fabrication approaches for Si NWs realization

Nanotechnology represents the meeting place between engineering, physical and life sciences. Most of the new phenomena treated in this field of research arise from nanometer scale structures. In fact, these ideas have driven scientists to develop several methods for making different nanostructures. Making nanostructures is easier than it might be thought. In general, there are two approaches for creating small objects, which can be distinguished as top-down and bottom-up (fig.1.1). In the top-down approach, small features are "written" onto the material by a combination of different processes, i.e. lithography, etching and deposition, to form functional devices (fig.1.1, top-left corner). In other words, this strategy uses sculpting or etching to carve structures from a larger piece of material in a subtractive fashion. The top-down approach has been extremely successful in nanoelectronics, which is perhaps the best example of this approach nowadays. While developments continue to push the resolution limits of lithography, these improvements in resolution are associated with an increase in cost. This economic limitation and other scientific issues with the top-down approach motivated

several efforts to search new strategies for scaling down the dimensions of nanostructures in the next future [1]. On the other hand, the bottom-up approach consists in assembling chemically synthesized and well-defined nanoscale building blocks, much like the way nature employs proteins and other macromolecules to build complex biological and functional systems (fig.1.1, bottom-right corner). Most of the times this is a powerful alternative approach to conventional top-down methods [2], because it has the potential to go far beyond the limits of top-down technology by defining key nanometer scale metrics through synthesis and subsequent assembly - not by lithography. It is crucial for nanotechnology that each bottom-up approach focuses on three key topic areas. First, it necessitates nanoscale building blocks with precisely controlled and tunable chemical composition, morphology, structure and size, since these characteristics determine their physical properties. To meet this goal requires developing methods that enable rational design and predictable synthesis of building blocks. Second, it is critical (and needs much effort) to develop and explore the limits of functional devices based on these building blocks. It could happen that nanoscale structures don't behave like current electronic and optoelectronic devices, whereas some new and potentially revolutionary concepts will emerge from these building blocks, for example, due to quantum mechanical properties. Third, it will be the development of architectures that enable high density integration with predictable functions, and the development of hierarchical assembly methods that can organize building blocks into these architectures.

In the nanotechnology scenario, nanowires (NWs) represent a new class of nanostructures, which are promising for their physical and chemical properties. In this decade these systems are attracting the interest of scientists and of IC industry in a broad range of nanoscale devices. Their physical properties afford them applications in a vast network of active microelectronic research fields, including logic device scaling in very large scale integrated circuits (VLSI) [3], photonics [4], life sciences [5], biological sensor devices [6], solar cells [7] and energy storage [8]. They are quasi-one-dimensional systems with a high surface to volume ratio, in which carriers can be confined in two dimensions and are free on the third one (the axial one). Hence, their electrical, optical, thermal and magnetic
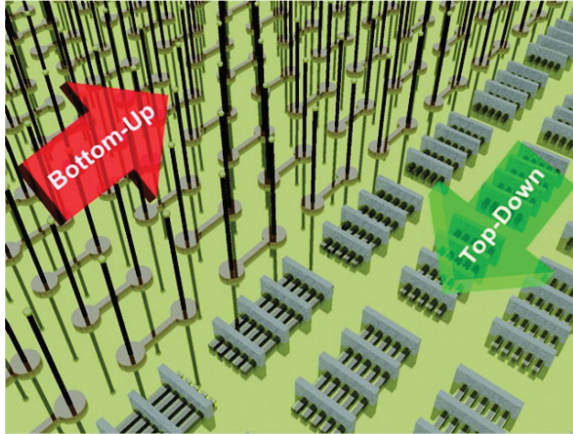
Figure 1.2: *A sketch of bottom-up and top-down paradigms applied to NWs fabrication [9]*

properties could undergo a tremendous change with respect to the bulk material. Also other physical features, such as their internal structure (i.e. their amorphous or crystalline phase) or their aspect ratio can affect these properties. All these features are dependent on the adopted synthesis technique. A range of routes to semiconductor nanowire production have opened up as a result of advances in nanowire fabrication techniques over the last number of decades.

There are both bottom-up and top-down approaches also for NWs fabrication. Figure 1.2 sketches of these two different approaches applied on nanowires [9]. Microelectronic systems typically rely on integrated device platforms, where each device and component thereof can be individually addressed. This requirement for precise addressability places significant demands on the mode of fabrication, specifically with regard to device definition, placement and density, which have typically been strengths of top-down fabrication processes. However, in recent years, advances in bottom-up fabrication processes have opened up the possibility of a synergy between bottom-up and top-down processes to achieve the benefits of both. Additionally, fabrication of nanowires of a wide range of materials has been demonstrated, which may not be readily produced in wafer form [10, 11, 12].

In the NWs scenario, silicon nanowires (Si NWs) are the most at-

tentioned system, since they are compatible with existing Si-based technology and can be readily integrated with CMOS technology. Si NWs are commonly fabricated by different bottom-up methods like vapor liquid solid growth [13, 14] and its analogues techniques, by seedless growth [15], template assisted growth [16], metal organic vapor phase epitaxy (MOVPE)[17], molecular beam epitaxy (MBE) [18], or by top-down methods like the electron beam lithography (EBL) followed by etching [19]. In the following sections the major fabrication routes to produce Si NWs in both paradigms will be discussed, while identifying recent advances and highlighting the benefits and drawbacks of these routes.

1.1.1 Vapor Liquid Solid-driven Si NWs growth

The most common technique to fabricate Si NWs is the vapor liquid solid (VLS) growth. This bottom-up technique was invented by Wagner and Ellis during the '60s [13] and uses metallic particles as catalysts for the growth. This method takes advantage of the specific binary alloy between silicon and some specific metals (e.g. Au, Cu, Pt.. etc.). The choice of an appropriate seed material has the benefit of allowing control over the diameter of the nanowires produced, while the seed material can also significantly affect the crystalline quality of the nanowire [20]. Typically, above the eutectic temperature (lower than the melting temperature of both silicon and of the metal), an eutectic liquid phase is formed at the interface between the metal droplet and the Si NW. Analogues of the VLS mechanism include supercritical fluid–liquid–solid (SFLS) [14], supercritical fluid– solid–solid (SFSS)[21], vapor–solid–solid (VSS)[22] and oxide assisted growth (OAG) [23] mechanisms. Common to all of these analogues is the existence of a collector or seed particle, which acts as a sink for the nanowire material, and from which unidirectional growth proceeds [24]. Conventionally, the seed particle is a metal with which the nanowire material or component thereof forms an alloy. Concerning the VLS process, when the temperature is above the eutectic temperature, providing Si atoms from a vapor phase (V), these can diffuse into the liquid phase (L) which is formed at the Si/metal interface, and can definitely segregate at the solid part (S) of the NW. Hence the Si/metal interface moves
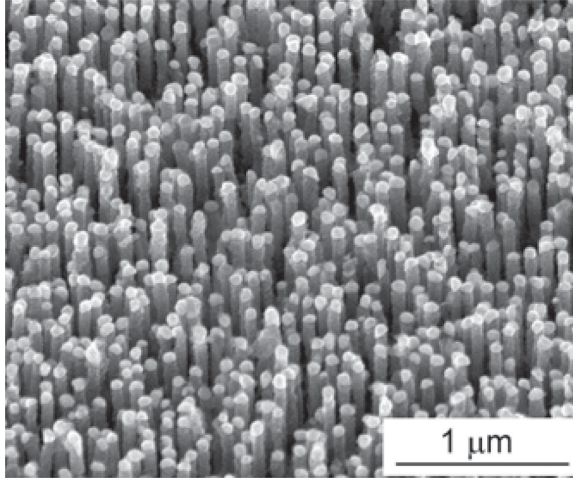
Figure 1.3: *Densely packed Si NWs fabricated by VLS using an alumina template [16]*

and the NW grows axially[13]. These Si NWs grow epitaxially on the substrate, with a mean diameter of the order of tens of nanometers. The resulting structure is visible in fig. 1.3. The Si percentage into the Si/metal alloy is a key parameter for the growth. This percentage depends on the *liquidus* curve (in blue) on the alloy phase diagram, as shown in fig. 1.4.a for the Si/Au alloy. Gold is commonly used as a catalyst for VLS-type nanowire growth, thanks to its low eutectic temperature (363°C) and since it is inert. It is prepared either as colloidal Au nanoparticles or as an evaporated
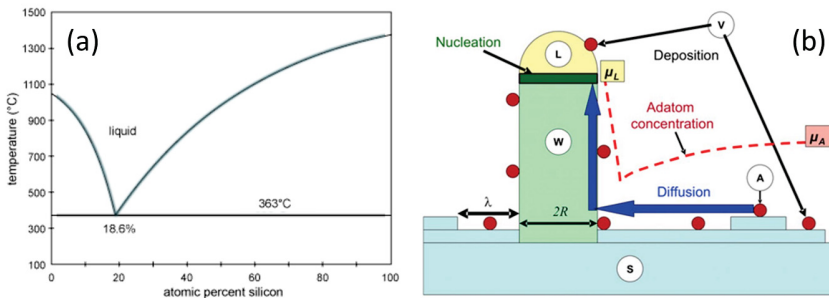
Figure 1.4: *(a) Phase diagram of the gold-silicon alloy. (b) Kinetics in VLS growth of Si NWs [28]*
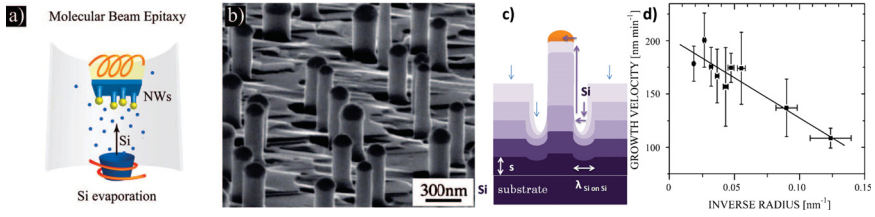
Figure 1.5: *(a) A sketch of a MBE chamber. (b) A tilted SEM image of VLS-type Si NWs grown by MBE [30]. (c) A scheme for the dip formation around each Si NW during the growth [31]. (d) Growth velocity of Si NWs as a function of the inverse of the radius [30].*

or sputtered thin film followed by a subsequent annealing in such a way to form droplets. The thermodynamical region in fig. 1.4.a under the blue curve is the supersaturation region: when the temperature is above 363°C and the Si percentage in the alloy is more than 18.6% then the thermodynamic state is inside this region and Si NW growth occurs. Hence, the droplet supersaturation is the origin of the growth. Two mechanisms lead to the supersaturation in VLS process: direct absorption of Si atoms from the vapor phase and ad-atoms diffusion from the Si surface through the sidewalls of each NW. These mechanisms are sketched in fig. 1.4.b. The contribution of these mechanisms has a different weight depending on the experimental technique adopted for VLS growth, i.e. physical vapor deposition (PVD) and chemical vapor deposition (CVD) techniques. In fact, a strong contribution to supersaturation from ad-atoms diffusion is typical for PVD techniques as Molecular Beam Epitaxy (MBE) [25] and Electron Beam Evaporation (EBE) [26]. The scheme of a PVD apparatus is shown in fig. 1.5.a in which a few atoms evaporated from a silicon crucible reach the heated surface of a silicon wafer covered by gold particles. In the model developed by V. Dubrovskii et al. there are five phases that have to be considered: the vapor, ad-atom, liquid, NW and surface phase, with their different chemical potentials, as shown in fig. 1.4.b. The difference between the vapor and the substrate chemical potentials is the thermodynamical *driving force* for gold droplet supersaturation and definitely for growth. It is controlled by the temperature T and by the deposition rate V [27, 28]:

$$\Delta\mu_{VS} = \mu_V - \mu_S = kT \ln\left(\frac{V}{V_0^S}\right) = E_A + \Lambda - kT \ln\left(\frac{h\nu_A}{V}\right) \quad (1.1)$$

where V_0^S is the deposition rate at equilibrium at the temperature in which absorption rate of atoms from the substrate is equal to its desorption rate, E_A is the activation energy for desorption, Λ is the latent heat in the ad-atom-substrate transition, ν_A is the vibration frequency, h is the thickness of a single monolayer (ML), and k is the Boltzmann constant. This model explains the occurrence of a bell-shaped curve of the growth velocity as a function of the temperature, observed in PVD growth by different groups [26, 29]. In fact, this curve arises from the compromise between two effects: diffusion of atoms which is thermally activated and has a relevant role at low temperature, and desorption of atoms from the NW which acts a relevant role at high temperatures. A fingerprint of diffusion is also visible in NWs obtained both by MBE [30] and EBE [26], where a dip all around each NWs is visible (see fig. 1.5.b). It has been demonstrated that the dimension of this dip is comparable with the diffusion length of silicon ad-atoms on Si surface [31]. The area around the NW acts as a reservoir for its growth, while far from the NW a 2D layer of Si is deposited, as shown in fig. 1.5.c. Finally, the particular behavior of the growth velocity as a function of the radius of the NW, shown in fig. 1.5.d, is another signature of the diffusion induced growth. Moreover, the diffusion induced NW growth is possible only when $\mu_A^\infty > \mu_L$. The term μ_A^∞ describes the chemical potential of the ad-atoms far from the NW, whereas $\mu_L = \mu_L^\infty + 2\Omega_L\gamma_{LV}/R_L$ is the droplet chemical potential, keeping count of the Gibbs-Thompson effect. Then, γ_{LV} is the surface energy at the vapor/liquid interface , Ω_L is the atomic volume of an atom in the liquid phase and $R_L = R/\sin(\beta)$ is the droplet radius. The Gibbs-Thompson effect is responsible of the minimal radius achievable with VLS technique. In fact, when R_L is too small, the chemical potential μ_L increases, it becomes higher than the chemical potential of the ad-atoms far from the NW ($\mu_L > \mu_A^\infty$) and the NW growth cannot occur. Au-catalyzed growth of Si NWs with diameters below 10 nm in the [110] growth direction was observed when the seeds were as small as 3 nm [32]. This is considered to be the thermodynamically allowed minimum diameter for the VLS
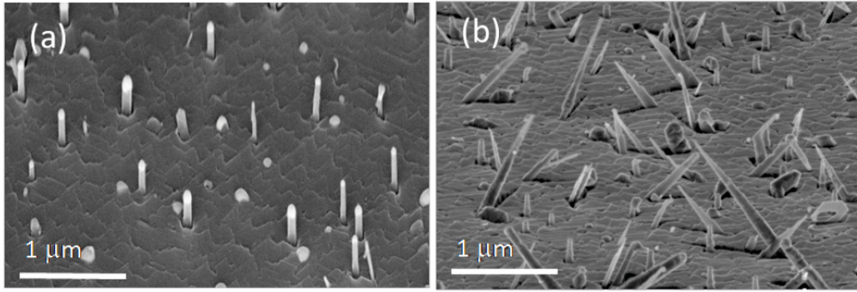
Figure 1.6: *(a) Tilted SEM image of vertical VLS type Si NWs grown by EBE at low fluences (b) Tilted SEM image of tilted VLS Si NWs grown al higher fluences [26]*

growth mode [33], however an integrated growth of sub-10nm Si NWs on a Si substrate with a high density and uniform size distribution is not easily obtained from densely packed Au nanoclusters.

One of the advantages of PVD on CVD technique is the possibility to control the direction of Si NWs with some specific techniques. For example, EBE allows to grow different families NWs epitaxial to the substrate with (111), (100) and (110) orientations and the growth rate is observed to have a strong orientation dependence. This suggests a microscopic growth mechanism based on the atomic ordering along (110) ledges onto (111) oriented terraces [26]. It has been shown that it is possible to control selectively the occurrence of vertical Si NWs rather than tilted ones by changing the evaporated silicon fluence. In fact, at the beginning of the evaporation, over a silicon fluence of 1.75 or 2×10^{18} atoms cm^{-2}, almost all of the NWs are perpendicular to the substrate, i.e. (111) oriented, with a relative population of this family being about 80 - 90%, as shown in fig. 1.6.a. By increasing the evaporated amount of silicon, the percentage of perpendicular NWs decreases, and (100) or (110) oriented NWs appear. The percentage of (111) oriented NWs can decrease to values as small as $\approx$ 20% at the maximum fluence of 2.5×10^{18} atoms cm^{-2} while the sum of (100) and (110) inclined NWs grows to values of $\approx$ 80% of the total population. The percentage of (111) oriented NWs at high Si fluence lowers because from one side the growth rate of (111) oriented NWs falls and 2D covering starts suppressing the shortest NWs and, at the same time
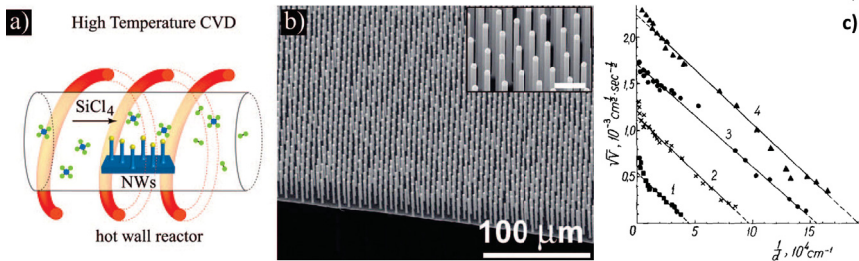
Figure 1.7: *(a) A sketch of a MBE chamber. (b) A tilted SEM image of VLS type Si NWs grown by CVD using a Cu catalyst [35]. (c) dependance of the velocity of etching on the diameter of the NWs in the CVD growth, at different supersaturations [36].*

(100) and (110) NWs appear at a later stages but grow much faster, becoming quite long. In fact, NWs longer than a micrometer are easily observed (see fig. 1.6.b).

The other most common technique for VLS-type growth is the CVD technique. This technique allows to have high throughput and high velocity of growth of NWs. As for PVD processes, a sample of Si with gold droplets on top is introduced into a CVD reactor with a base vacuum between 10^{-8} and 10^{-4} Torr. The sample is heated up to the growth temperature, and a transfer gas is introduced into the chamber (H_2, Ar or N_2). Then a precursor gas is introduced into the chamber, since it contains the chemical species that has to be deposited on the sample. The precursor gas partial pressure into the camber spans in the range between 10^{-5} and 1 Torr, while the total pressure can be from one up to three orders of magnitude more. The technique is depicted in fig. 1.7.a. Metal hydride precursors are commonly used in the growth of nanowires by CVD, given that metal hydrates such as SiH_4 generally exist as gas phase compounds [34]. Metal−organic precursors, such as diphenylsilane, often used in solution phase and supercritical fluid phase nanowire synthesis can produce carbonaceous byproduct, which may be difficult to completely separate from the nanowire product. For the most common metal hydride, i.e. SiH_4, at the surface of the metallic droplet the following reaction occurs:

$$SiH_4(g) \rightarrow Si + 2H_2(g)$$
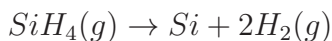
Hence, the SiH_4 molecule cracks preferentially on the liquid Si/metal droplet, diffuses into the droplet and segregates at the interface between the droplet and the Si NW. These chemical reactions are thermally activated and, at the low temperature adopted for growth (slightly above 360°C), the probability they occur at the substrate is low. The metallic catalyst instead, lowers the activation energy for breaking precursor molecules just on top of the droplet. This makes NWs to grow faster than the substrate, differently from PVD techniques, where the grow rate of NWs and of the 2D silicon overgrown layer are of the same order of magnitude [26, 30]. The SEM image of fig. 1.7.b shows an excellent example of Cu-catalized Si NWs grown by CVD technique on a (111) Si substrate at 850 - 1100 °C by using an atmosphere of H_2 and $SiCl_4$ [35]. The growth of thinner nanowires is typically slower than the growth of thicker ones. The dependence of the axial velocity of growth with the radius of the Si NWs has been studied for the first time by E. Givargizov [36], and is shown in fig. 1.7. The curves $1 \rightarrow 4$ of this figure correspond to increasing molar concentrations of $[precursor\ gas]/H_2$, hence to increasing supersaturations of the semiconductor in the droplet. The growth rate lowers because supersaturation vanishes. These results show the existence of a critical radius, typical of the material and of the growth conditions in the CVD growth, at which the growth stops. For thinner radii the growth doesn't occur. This is the so called Gibbs Thomson effect, which happens also in CVD VLS-type growth of Si NWs and has the same origin of the effect described for PVD growth.

One benefit of bottom-up nanowire growth over top-down processing is that nanowires grown by bottom-up methods may be doped in situ during crystal growth by incorporating dopant precursors in the nanowire synthesis procedure. Consequently, bottom-up grown nanowires may not require destructive techniques such as ion implantation to generate additional charge carriers. Ion implantation can destroy atomic ordering in the implanted region of the semiconductor crystal and requires subsequent thermal annealing steps to restore crystal ordering [37]. At high doses, a permanent bending of NWs in the direction of the beam after implantation has been observed, due to a plastic deformation of the amorphized Si NWs [38]. By the way, the understanding and control of doping concen-
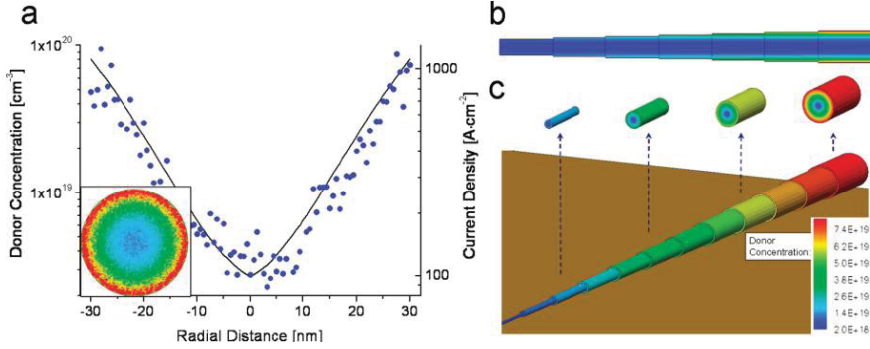
Figure 1.8: *(a) Radial distribution of the active dopant atoms in a VLS type Si NW. (b,c) 2D and 3D simulations of the calculated doping profiles. [40].*

tration, distribution, and activation is critical for the fabrication of high-quality electrical devices for various future applications. There are many nanowire systems in which the majority carrier type is controlled by intentional doping, but in all cases the actual dopant concentration, its spatial distribution, and the fraction of active dopants are unknown [39]. E. Koren et al. measured the radial distribution and diffusion of active dopant atoms in individual silicon nanowires grown by the vapor-liquid-solid (VLS) method [40]. For device fabrication, nanowires were suspended in solution by sonication in isopropyl alcohol and drop-cast onto degenerately n-doped silicon substrates with 200 nm of Si_3N_4 insulator on top, and contact regions were defined by electron beam lithography. The method they adopted for measurements is based on surface etching of a portion of a contacted nanowire, followed by measurement of the potential difference between the etched and the unetched areas using the Kelvin Probe Force Microscopy (KPFM). This process is repeated several times to gradually remove material, and the surface potential difference (between the etched and unetched parts) is measured for a number of nanowire radii. The radial dopant distribution is then obtained by fitting the measured potentials with a 3D solution of Poisson equation. They found that the radial active dopant distribution decreases by almost 2 orders of magnitude over a radial distance of 25 nanometers from the wire circumference to its center even when there is no indication for tapering. This is

Figure 1.9: *A dark field TEM image showing the gold diffusion from the droplet into the VLS type NW during the growth [42].*
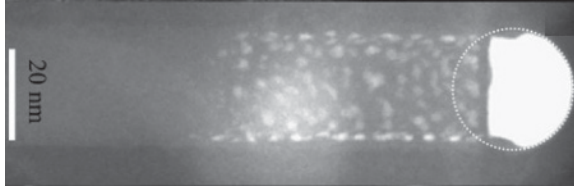
shown in fig. 1.8.a. In addition, the measured dopant profile is consistent with a diffusion coefficient of $D \approx 1 \times 10^{-19} m^2 s^{-1}$. Figures 1.8.b and 1.8.c show respectively the calculated 2D and 3D doping profiles in the NW for this diffusion coefficient. This implies that phosphorus (P) diffusion during the VLS growth is remarkably high and subsequent thermal annealing must be used when a homogeneous dopant distribution is required.

Another drawback of VLS-type grown Si NWs is diffusion of metal from the droplet into the wire during the Si NWs growth at the VLS growth temperature, as shown in the TEM image of fig. 1.9 [42]. As previously mentioned, gold is the main used catalyst for VLS-type NWs growth. Gold forms deep electronic states inside the Si electronic bandgap, and these middle-gap states increase the probability to achieve Shockley-Hall-Read (SHR) recombination in Si, hence this is detrimental both for electronic and photonic applications. It is a highly inert material, which makes cleaning of instrumentation contaminated with Au extremely difficult. For example, traditional Au etchants include aqua regia (concentrated nitric acid and hydrochloric acid solution), K_I/I_2 solution and alkali cyanide solutions, all of which would corrode stainless steel equipment and, in the case of alkali solutions, result in detrimental effects on semiconductor device performance, such as shifting of threshold voltage [41]. Consequently, from the electronics point of view, there has been significant research into alternative, complementary metal-oxide-semiconductor (CMOS) production compatible, metal seeds for catalyzed VLS semiconductor nanowire growth [43]. Acceptable metals should have ionization energies far from the mid band gap region of the semiconductor material. Si nanowire growth has been demonstrated using a number of Si CMOS compatible metals in-

cluding Bi [44], Al [45] and Cu [35]. Great care must be applied even when using CMOS compatible metals for nanowire growth, as these metals can still act as active dopants in the nanowire material. Al, for example, can readily migrate through Si via interstitial sites in the Si lattice, thus acting as an n-type dopant in Si. Furthermore, Si migration through the Al metal is also possible and may dramatically affect the electrical performance of the nanowire material.

From a photonics point of view, gold middle-gap levels are efficient states for carriers recombination, in fact the high probability of SHR recombination process suppresses the low probability phonon-assisted radiative recombination processes, hence there is no emission from VLS-type NWs. This means they are not generally suitable for photonics. Only few papers demonstrating luminescence by VLS-based Si NWs are present in literature, e. g. made using $TiSi_2$ catalyst as metallic seed [46, 47]. Top-down strategies have to be found in order to achieve light from silicon, e.g. EBL lithography or metal assisted etching. The first strategy allows to obtain NWs with diameters generally higher than the exciton wavelength of the electron-hole pair, hence the NWs radial dimension has to be subsequently shrinked via oxidation processes in order to obtain quantum confinement of carriers and definitely luminescence from NWs [19]. A promising possibility to obtain light from NWs is to fabricate Si NWs by metal assisted etching. This is a low cost, top-down etching technique, and allows to obtain structures potentially thin enough for quantum confinement, regardless of any further oxidation of the NW. Moreover, since the chemical process adopted is at room temperature, gold diffusion inside the NW is obviously negligible. For these reasons metal assisted etching could be a good candidate for low cost silicon photonics. Both of these techniques will be discussed in the following paragraphs.

1.1.2 Electron Beam Lithography and Reactive Ion Etching

Several lithographic processes are being considered to extend lithography scaling beyond current UV lithography capabilities for semi-
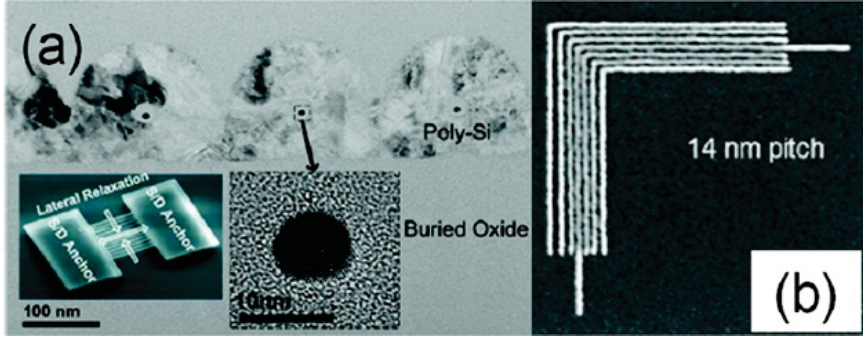
Figure 1.10: *(a) A n-Si NW Field Effect Transistor, made by Electron Beam Lithography (b) Different Si NWs separated by a pitch of 14 nm[52].*

conductor device manufacturing. These techniques include electron beam lithography (EBL) [48], electron beam induced deposition lithography (EBID) [49], X-ray lithography (XRL) [50], nanoimprint lithography (NIL) [51] etc. EBL is at the head of many of these techniques. It is generally used for fabrication of high resolution photomasks for deep ultraviolet lithography (DUV), extreme lithography (EUV), and XRL. EBL has been shown to be capable of producing sub-10-nm features at sub-20-nm pitches [52]. In fact, fig. 1.10.a displays examples of high-resolution EBL processes used to produce planar strained n-Si NWs with a diameter of 8 nm in order to make a NW based Field Effect Transistor (FET). Fig. 1.10.b shows that it is possible to create densely packed planar NWs with an intermediate pitch of 14 nm. Arrays of dot structures produced by EBL can be used to fabricate vertical nanowire arrays through the use of a deep anisotropic etch [19]. The use of an etch resistant material to form the dot structures is paramount to facilitate deep etching to form high aspect ratio nanowires. Typically, Al_2O_3, Al, and SiN_x have been used as etch masks for vertical Si nanowire fabrication. Figure 1.11.a shows an SEM image of arrays of vertical Si nanowires produced using an EBL process . In this work, Walavalkar et al. [19] fabricated top-down, etched, silicon nanopillars and further thinned them via self-terminating oxidation to demonstrate photoluminescence as well as measure radiative lifetime with respect to reduction in pillar diameter. Pillars were de-
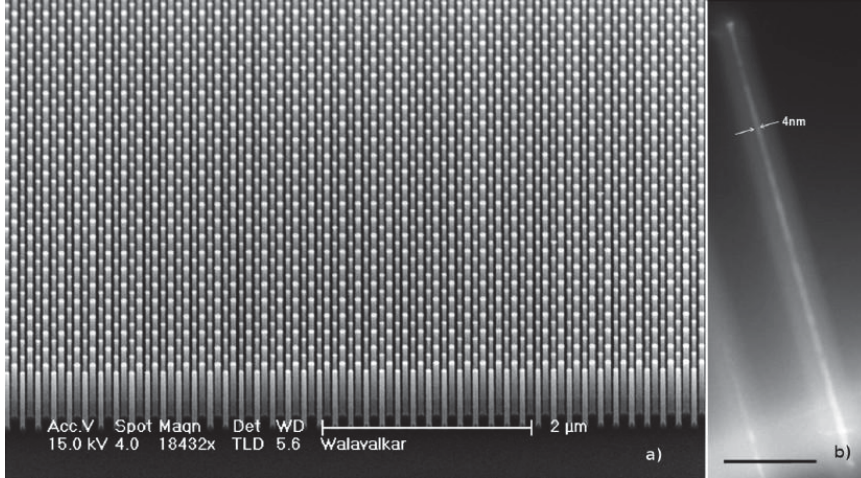
Figure 1.11: *(a) An tilted SEM image of an array of EBL made Si NWs (b) A TEM image of an oxidized Si NW showing a crystalline core of 4 nm [19].*

fined by e-beam patterning an array of 30 - 50 nm disks in 75 nm of polymethilmetacrhrilate (PMMA) resist on (100) Si. A 25 nm layer of Al_2O_3 was deposited as a hard-mask via DC-magnetron sputtering of aluminum with a 5:1 Ar/O_2 process chemistry and patterned via lift-off. Aluminum oxide is a resistant and chemically inert etch mask [53] providing a selectivity of greater than 60:1 for a fluorine etch chemistry. The anisotropic plasma etching is performed in a mixture of gases i.e. SF_6 (to etch) and C_4F_8 (to passivate). Sidewall profiles are controlled by adjusting the etch to passivation gas ratio. Figure 1.11.a shows the uniformity in postetch profile of a pad of nanowires. After etching, the pillars were oxidized in a dry ambient in the temperature range of 850 - 950 °C. Silicon core diameters were measured using transmission electron microscopy (TEM) with the silicon pillars positioned perpendicular to the incoming electron beam. In fig. 1.11.b it is possibile to observe a nm silicon core width by utilizing the diffraction contrast between the crystalline Si and the amorphous SiO_2. There has been extensive work regarding the two-dimensional oxidation of cylindrical silicon structures [19]. This work demonstrated that cylindrical silicon pillars exhibit a self-terminating core diameter and oxide thickness
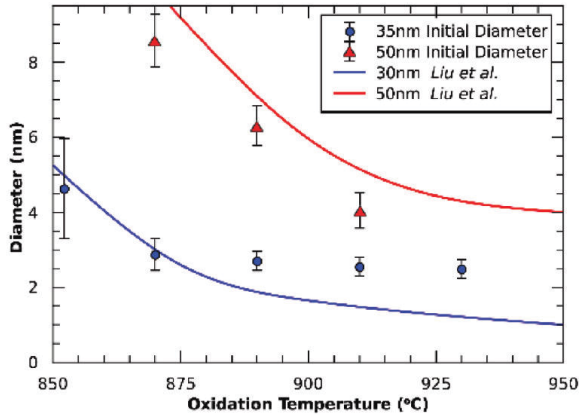
Figure 1.12: *Self-inhibited oxidation of EBL made Si NWs, at different starting diameters of the NWs [19].*

that is a function of the initial silicon diameter and the temperature of the oxidation [54]. Several mechanisms have been proposed to explain this effect predicated on the idea that during oxidation at temperatures below 950 °C there is a lack of viscous flow of the grown oxide. The lattice mismatch between the silica and silicon creates a thin high-stress region at the $Si - SiO_2$ interface preventing diffusion of oxygen molecules or kinetically ruling out further oxidation. Figure 1.12 shows the final pillar diameters as a function of initial diameter (35 or 50 nm) and oxidation temperature. By taking benefit of the self-terminating properties of nanopillar oxidation they fabricated uniform 1 μm tall pillars with diameters of the crystalline core between 2 and 8 nm. By varying the oxidation temperature it is possible to decrease the core diameter and definitely tune the light emission which is due to quantum confinement of carriers. However, even if EBL technique is in principle compatible with CMOS technology, the main issue in implementation of EBL-made NWs in VLSI is the low throughput of wafers due to the high exposure time required for full wafer layouts. The exposure time depends on several factors, e.g. the resist sensitivity, the electron energy and dose required to change the resist phase, etc. [55]. Multibeam EBL systems are under development, which will increase wafer throughput either through beam-splitting techniques, or through the use of instruments with multiple electron

19
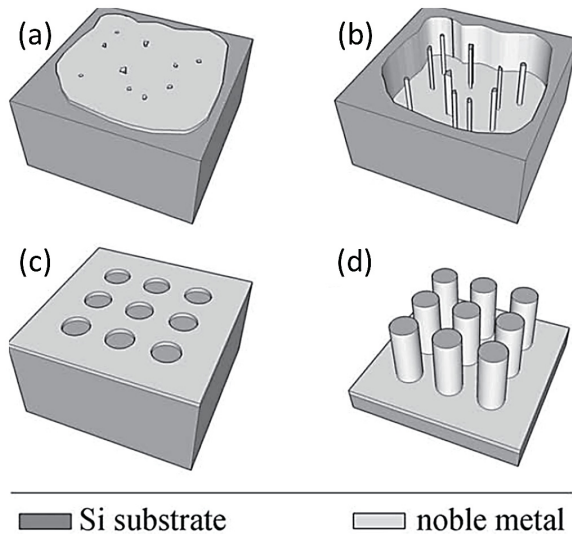
Figure 1.13: *(a) Self organized metallic mesh deposited before the MACetch process. (b) Si NWs after the MACetch. (c) Patterned metallic mesh deposited before the MAC etch process. (d) Si pillars with a uniform and controllable size[61].*

sources; however, the technology is still not mature and has yet to be implemented on a high volume manufacturing (HVM) scale at the moment.

1.1.3 Metal Assisted Chemical Etching

Metal assisted chemical etching (MACetch) is a method of preparation of Si NWs which in the recent years has demonstrated successful and attracted much interest for several reasons. In a typical metal-assisted chemical etching procedure, a Si substrate partly covered by a noble metal is subjected to an etchant solution composed of HF and an oxidant agent. Typically, the Si beneath the noble metal is etched much faster than the Si without noble metal coverage. As a result, the noble metal sinks into the Si substrate, generating pores in the Si substrate or, additionally, Si wires (see fig. 1.13). Let's sum up the strengths of MACetch on other techniques. First, MACetch is a simple and low cost method for fabricating various Si nanostructures with the ability to control vari-

ous parameters e.g. length, diameter, cross-sectional shape orientation, doping type and dopant concentration. Then, it is possible to control the orientation of NWs relative to the substrate. In contrast, in VLS-type growth of Si NWs, because of the existence of equivalent directions of growth, it is difficult to grow epitaxial Si nanowires with uniform orientation relative to the surface of the Si substrate. For example, the growth of [100] vertical NWs only on a (100) substrate isn't possible without a template. On the other hand, it is well known that electrochemical etching occurs on [100] directions and, although MACetch is intrinsically anisotropic, methods have been developed to control the etching direction also in non (100) substrates [56]. Moreover, the crystalline quality of Si nanowires fabricated by metal-assisted etching from single crystalline substrates is generally high. Although their surfaces are typically rougher than those of nanowires obtained by VLS growth, the nanowires do not contain the obvious crystallographic defects induced by solution-based etching, while dry etching (e.g. RIE) tends to introduce defects in a region close to the etched Si surfaces [57]. Furthermore, VLS based methods can only be used to grow structures with a circular cross section, while by MACetch is possible to make higher surface to volume ratio structures [58, 59]. Finally, there is no obvious limitation on the size of the diameter of these NWs. It is possible to realize NWs with diameters scaling down from 1 μm to 5 nm [60]. However, there is a well known rule that limits the feature size of structures obtained from MACetch, due to the presence of a space charge of width W_{sc} localized at the solution/Si interface [61].

Etching mechanisms

The first demonstration of MACetch in Si was reported in 1997. Porous Si was fabricated by etching an aluminum (Al) covered Si substrate in a solution composed of HF, HNO_3 , and H_2O. The incubation time necessary for the formation of porous Si was dramatically decreased due to the presence of the Al film on the surface of the Si substrate [62]. The widely used metal-assisted chemical etching method was first investigated in some detail by Li and Bohn, who found that a thin layer of noble metal (e.g., Au, Pt, or Au/Pd

Figure 1.14: *Hole injection processes during the MACetch. [61]*

alloy) sputtered on the surface of a Si substrate catalyzed the etching of Si in a mixed solution containing HF, H_2O_2, and ethanol, resulting in straight pores or columnar structures [63].

Fig. 1.14 depicts the scheme of MACetch process: a Si substrate is in contact with an isolated noble metal particle which is etched in an etchant consisting of HF and H_2O_2 . The chemical or electrochemical reactions occur preferentially near the noble metal. It is well accepted that H_2O_2 is reduced at the metal (1), which acts as a cathode:

$$H_2O_2 + 2H^+ \rightarrow 2H_2O + 2h^+ \tag{1.2}$$

Li and Bohn [63] and Harada et al. [64] proposed that the reduction of protons into hydrogen was another cathode reaction in addition to reaction 1.2:

$$2H^+ \rightarrow H_2 \uparrow +2h^+ \tag{1.3}$$

Then, holes generated due to the reduction of the oxidant diffuse through the noble metal (2) and are injected into the Si that is in contact with the noble metal. At the anode, the Si substrate is oxidized and dissolved (3). There are numerous models proposed for the dissolution process of Si (anode reaction), which can be catalogued into three groups:

22

$$Si + 4h^+ + 4HF \rightarrow SiF_4 + 4H^+ \tag{1.4}$$

$$SiF_4 + 2HF \rightarrow H_2SiF_6 \tag{1.5}$$

(RII) Direct dissolution of Si in divalent state [61]:

$$Si + 4HF_2^- \rightarrow SiF_6^{2-} + 2HF + H_2 \uparrow + 2e^- \tag{1.6}$$

(RIII) Si oxide formation followed by dissolution of oxide [61]:

$$Si + 2H_2O \rightarrow SiO_2 + 4H^+ + 4e^- \tag{1.7}$$

$$SiO_2 + 6HF \rightarrow H_2SiF_6 + 2H_2O \tag{1.8}$$
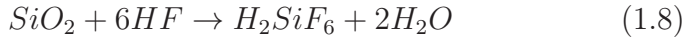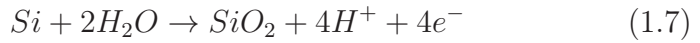
Model RI deals with the direct dissolution of Si in tetravalent state [61]. Model RII and RIII differ in whether Si oxide is formed at the surface of the Si substrate before the dissolution of Si (in RIII) and whether H_2 is generated accompanying the dissolution of Si (in RII). It seems that model RII happens because hydrogen is generated in a typical etching. However, whether model RIII occurs simultaneously remains an open question due to the difficulty in in situ exploration of the surface state and the uncertainty in ex situ study of the Si surface state (e.g., oxide might form during the handling of the etched structure for TEM characterization). Charge transfer is necessary for the oxidation and dissolution of Si. Hole injection is well-documented as a charge transfer process for metal-assisted chemical etching of Si. In addition, due to holes diffusion at the metal / Si interface (see fig. 1.14), the sinking in of a noble metal particle is sometimes surrounded by a microporous structure [65]. In this scenario, the noble metal acts as a microscopic cathode on which the reduction of the oxidant occurs (cathode reaction 1.2). The generated holes are then injected into the Si substrate in contact with the noble metal. Accordingly, the Si atoms under the noble metal are oxidized due to the hole injection and dissolved by HF (anode reactions 1.7 and 1.8). From the energy point of view, H_2O_2 can inject holes into the valence band of Si (fig. 1.15.a), independent of the doping type and doping level. The electrochemical
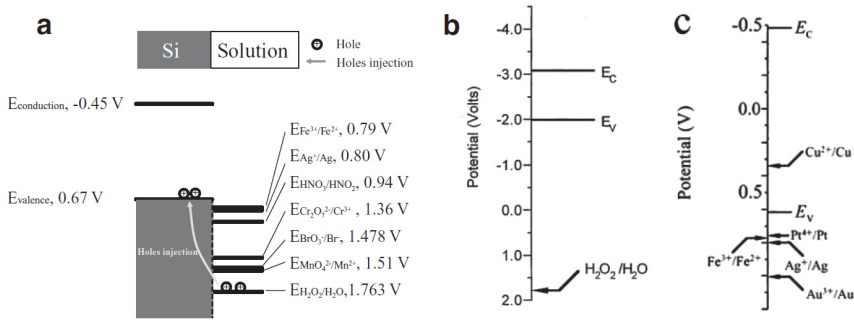
Figure 1.15: *(a) A comparison between the chemical potentials of different oxidants inf Si[61]. (b) Energy of the chemical potential of H_2O_2/H_2O compared to the silicon band edges[66]. (c) Energy levels of Si band edges compared to the potential of five redox metallic systems[68].*

potential of H_2O_2 is much more positive than the valence band of Si and more positive than oxidants usually used in stain etching of Si, e.g., HNO_3, $Fe(NO_3)_3$, $KMnO_4$, $KBrO_3$, $K_2Cr_2O_7$, etc.. [61]. It is important to know that the etching of Si by HF/H_2O_2 does occur, but the etching rate is lower than 10 nm/h in an etchant with a concentration of H_2O_2 much higher than that used in metal-assisted chemical etching [66]. The cathode reaction 1 occurs faster on the surface of noble metals than on a bare silicon surface. Several noble metals e.g. Au, Pt, Pd and Ag have been widely used to catalytically reduce H_2O and O_2. Once the oxidant is reduced on the surface of noble metal, holes are injected into the Si substrate. Chattopadhyay et al. [67] sketched the energy levels of Si substrate and the electrochemical potential of H_2O_2/H_2O and suggested that holes were injected deep into the valence band 1.15.b. Peng et al. qualitatively compared the electrochemical electron energy levels of the Si band edges and the electrochemical potential of five redox systems (Figure 1.15.c) and suggested that the reduction of Ag took place around existing Ag nuclei and Si was oxidized and dissolved [68]. The charge transfer between Si and noble metal would be heavily affected by the surface band bending of Si, which hasn't, however, been included in the models proposed by Chattopadhyay et al. and Peng et al. Meanwhile, the surface band bending of the Si substrate is determined by the doping type and doping level of
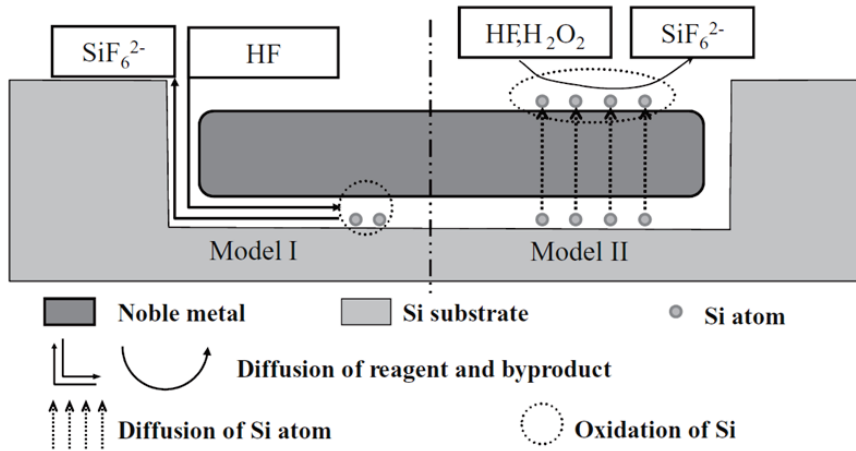
Figure 1.16: *Two mass transport mechanisms proposed for etching products during the MACetch process [61].*

the Si substrate, the surface state of Si substrate, the Fermi level and size of noble metal, and the component of the etchant. These factors have not been discussed in the etching mechanism of Si in literature. It has been speculated that the Si atoms are oxidized and dissolved at the interface between the noble metal and the Si substrate and that the reagent and byproduct diffuses along this interface (see Model I in fig. 1.16) [61]. This assumption is plausible for the specific case in which the etching is assisted by noble metal particles with small lateral size so that the diffusion of the reagent and the byproduct along the interface between the noble metal and the Si involves only a short distance and may be easily accomplished. On the other hand, there is another possibility concerning mass transfer during the etching. That is, the Si atoms that are in contact with a noble metal are dissolved in the noble metal and then diffuse through the noble metal to the noble metal/solution interface where the silicon atoms are oxidized and etched away at the noble metal/solution interface (see Model II in fig. 1.16). If the Si is covered with a noble metal with a relatively large lateral size (e.g., larger than 1 μm), lateral diffusion of the reactant and the byproduct along the interface of Si and the noble metal (Model I) is a long distance diffusion process, while diffusion of Si atoms through the metal involves a relatively short distance
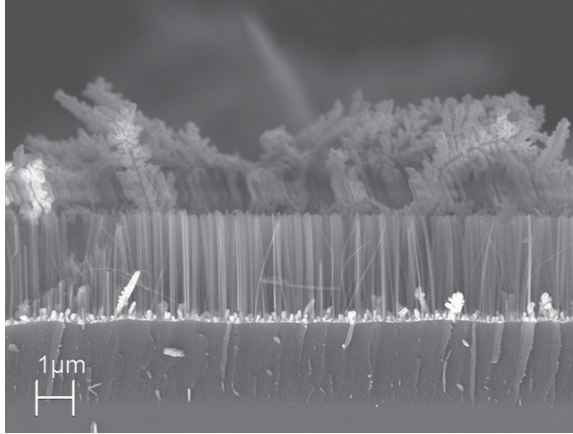
Figure 1.17: *A cross sectional SEM showing the dendrites formation over SI NWs occurring during the MACetch in $AgNO_3/HF$ solution.*

(few nanometers).

The most common (and easiest) way to obtain a metal deposition on a Si substrate is by using solution of metallic salts. Typical examples are $HF/AgNO_3$[69] or $HF/KAuCl_4$ [70]. Unfortunately dendrite structures of the deposited metal formed when a Si substrate was immersed in a solution containing HF and M_n^+(M = Ag or Au) for a relatively long time (e.g., longer than 30 min), in addition to the etching of the Si substrate (see fig. 1.17) [69]. After the formation of Si NWs these dendridic structures have to be removed via etching processes i.e. HNO_3 bath (for Ag removal), or acqua regia bath (for Au removal) or using KI/I_2 solutions (for both of them). As mentioned before, these additional chemical processes are detrimental for Si NWs because of their induced surface modification. These further processes can have detrimental effects both on optical and electrical properties of Si NWs. Due to their stability in the etchant solution, Au meshes allow the fabrication of Si nanowires with ultralarge aspect ratios (e.g., larger than 200) [60]. When fabricating Si nanowire arrays with a Ag mesh, which can slowly be dissolved by the etchant, new pores may form in the mesh leading to unintended Si nanowires at the location of these pores.

Zigzag nanowires

To realize the full potentials of Si NWs, new Si NWs building blocks with curved shapes are desirable, because they may be implemented into novel devices with fewer welding joints and improved electric connection. This kind of MACetch Si NWs may have unique advantages in device fabrication. Chen et al. reported the wafer-scale synthesis of single-crystal zigzag Si NWs with 150°, 125°, or 90° turning angle. These three type of zigzag Si NWs have been made by controlling the crystallographic orientation of the Si wafer, reaction temperature, and etchant concentration [56]. The SEM images of fig. 1.18.a-b-c show the scanning electron microscopy (SEM) images of a series of Si NW arrays that were synthesized on a (111)-oriented Si wafer by adjusting the etching temperature. All of these samples were prepared by putting a Si wafer in a etchant solution containing 4.6M HF and 0.04M $AgNO_3$ for 40 min. At low etching temperature, i.e. 15 °C, Ag nanoparticles (NPs) keep moving together along one direction and create arrays of straight Si NWs (see fig. 1.18.a). In sharp contrast, at the etching temperature of 55 °C, the movement directions of Ag NPs may change and curved Si NWs can be found (see fig. 1.18.b). Etching at 75 °C yields nanowires dominantly in the zigzag structure, as shown in fig. 1.18.c. Zigzag tracks are formed by periodic switches in the moving directions of the Ag NPs.The relative energies involved in Ag NP movements along various crystallographic orientations in Si wafer play a significant role in the formation of the curved Si NWs. The most preferred migration direction of Ag NPs in the Si wafer is the [100] direction[62, 71]. Indeed, when (100)-oriented Si wafer is used as a substrate, the products are mostly straight Si NWs even at relatively high etching temperatures and etchant concentrations. However, when a non-(100) surface, in particular the more inert (111) surface is used as the starting surface, the [100] etching orientations are no longer the only etching direction because of the large angle between the [100] and the [111] directions. Generally, the Ag NPs would first start moving perpendicular to the wafer along the [111] directions and then they either may keep moving along the [111] directions or may overcome higher potential barriers to move along other directions such as [100] or [113]. Two possible mechanisms
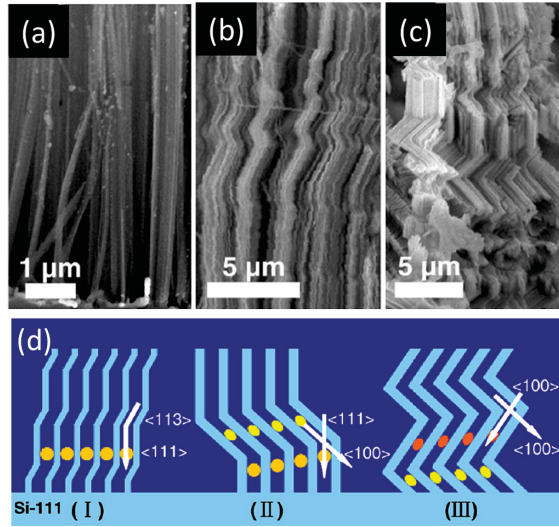
Figure 1.18: *(a,b,c) Cross sectional SEM images showing MACetch zigzag Si NWs at the temperature of 15°C, 55 °C, 75 °C respectively. (d) Possible mechanisms proposed for the formation of these zigzag structures by MACetch [56].*

for the formation of the novel zigzag structures are proposed below and schematically illustrated in fig. 1.18.d:

(1) Single-particle etching mechanism: due to perturbations at the reaction sites such as hydrogen bubbles, etc., individual Ag NPs moving initially along the [111] direction might switch to another nearby direction such as [113]. However, since the [113] orientation is not the most energetically favored orientation, as etching time increases, the Ag NPs may switch back to [111]. Repeating this perturbation process, the Ag NPs periodically switch their moving directions to etch out zigzag Si NW arrays as shown in fig. 1.18.d-I.

(2) Multiparticle etching mechanism: At higher etching temperatures/silver ion concentrations, the etching activity is enhanced, and more Ag NPs can overcome the potential barrier to change their moving directions from the original [111] direction to the lowest energy [100] direction and steadily move along the most preferred directions. Different Ag NPs at different locations might collectively move along one of the three different [100] directions. The merge of the moving tracks along the [100] and the [111] directions

would result in Si NWs with a 125° turning angle (see fig. 1.18.d-II). Similarly, the Si NWs with 90° bends are formed by the merge of Ag NPs moving along different [100] directions, as shown in fig. fig. 1.18.d-III.

Controlling nanowire dimensions

The question of the control of the position and the diameter of nanowires remains to be solved. Several efforts have been spent in making nanowires with a well defined radius, since the etching using metallic salts (e.g. $AgNO_3$) is a random process and therefore the mean radius of the NWs is not controllable. Huang et al. developed a simple but versatile method to fabricate highly ordered Si nanowires, enabling control of the diameter and length of the nanowire, as well as the density of nanowire arrays [72]. On the basis of this method, several approaches [73, 59, 74] have been developed to fabricate Si nanowire arrays with various diameters, Si nanowires with sub-10 nm diameter, vertically aligned non-(100) Si nanowire arrays relative to the substrate, as well as SiGe superlattice nanowire arrays [75]. Obviously, a key point is to control the features of the metal structure which will define the etched region. At the same time, the metal structure will define the position and features of the remaining structures of silicon after the etching. This approach is depicted in fig. 1.19.a. First, a monolayer of polystyrene (PS) spheres is assembled on a Si substrate. Subsequently, size reduction of the PS sphere is achieved by a RIE process. Each sphere becomes smaller, but they maintain their close packed order. Then, a noble metal film is deposited by thermal evaporation onto the substrate covered by these etched spheres. This process results in a continuous layer of noble metal with a periodic hexagonal array of pores. This is the metallic mesh for the etching. The diameter of the pores is determined by the remaining diameter of the RIE-etched PS spheres. Then, an etching process in HF/H_2O_2 occurs. During the etching, the noble metal mesh sank in the substrate, leaving the NWs-like unetched Si structures. Figure 1.19.b shows a typical SEM image of a Si NW array obtained by this method. The average diameter of Si NWs matches the diameter of the etched spheres. By using Langmuir–Blodgett PS NPs deposition technique
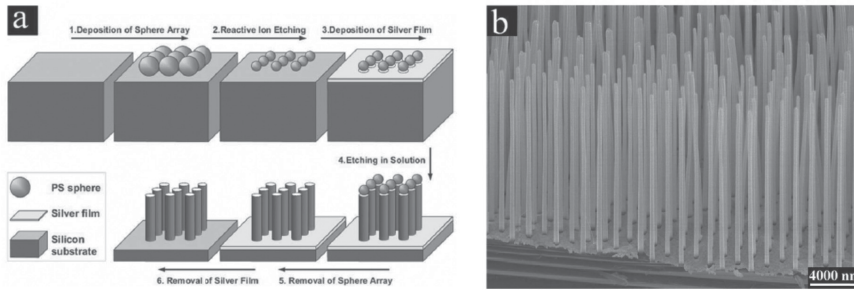
Figure 1.19: *(a) A versatile method to control diameter and position of MACetch Si NWs, by using PS lithography. (b) A tilted SEM of the obtained array of Si NWs* [72].

is possible to deposit PS densely packed spheres as small as 150 nm. Then, with RIE etching diameters of etched spheres (therefore of Si NWs) as small as 50 nm. This is roughly the resolution limit for the diameter of NWs by this technique. By this method, Si NWs with an aspect ratio larger than 30 could be obtained. Changing the length is trivially obtained by changing the etching time, since the length of the etched region goes linearly with the etching time. These structures, are slightly tapered. This can be attributed to a lateral etching occurring during the whole process, or to a shape evolution of the Ag mesh. However, the nanosphere approach is difficult to realize for Si NWs with diameters smaller than 20 nm.

A more performant method to obtain thinner NWs with radii below 20 nm consists in using an anodized aluminum oxide (AAO) template [76]. Ultrathin AAO membranes with regular hexagonal ordered arrays of pores were used as masks for the surface prepatterning of silicon substrates prior to MACetching of silicon and allowed to circumvent the problems associated with the conventional nanosphere-based lithographic approach. AAO membranes with pore sizes ranging from 20 to 350 nm and pore densities from $5 \times 10^8/cm^2$ to $3 \times 10^{10}/cm^2$ can conveniently be prepared by anodization of aluminum [77]. The experimental procedure is shown in fig. 1.20. First, an ultrathin AAO membrane/polystyrene (PS) composite (thickness about 300 nm) was placed on a (100) Si substrate (fig. 1.20.a), then PS that was spin-coated to stabilize ultrathin AAO membrane was removed by oxygen plasma. Subse-
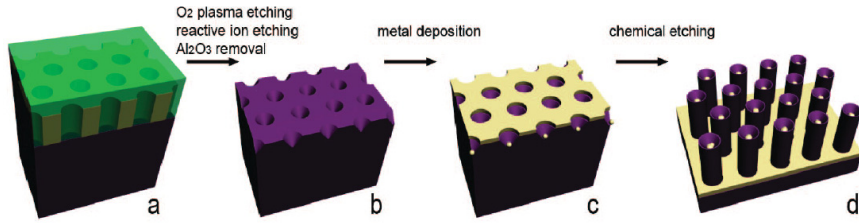
Figure 1.20: *Experimental procedure to make sub 10 nm Si NWs by using an Anodized Aluminum Oxide (AAO) template [76].*

quently, reactive ion etching (RIE) was performed to pattern the surface of Si (100) substrate under SF_6/O_2 plasma and the AAO template is removed (fig. 1.20.b). Subsequently, a thin layer of silver or gold was deposited onto the patterned Si (100) substrate. The sputtering process resulted in a uniform coating of metal both on the top surface and on the pore bottom of the patterned Si (100) substrate, but not on the side walls of the pores. The diameter of the pores in the metal film caused by the etchpits decreased as a function of deposition time (fig. 1.20.c). Finally, ordered arrays of vertically aligned Si NWs on Si (100) substrate were obtained by performing MACetching of silicon in a mixture solution ($HF/H_2O_2/H_2O$, volume ratio: 10/5/35) at room temperature, in dark conditions for 30 s (fig. 1.20.d). Figure 1.21.a shows a representative cross-sectional SEM micrograph of a sample after RIE treatment. It shows that the hexagonal pattern of the AAO mask was successfully transferred onto the underlying Si substrate with a high degree of fidelity. It is expected that both the silver film on the surface of silicon substrate and the silver particles at the bottom of the holes would participate in the chemical etching of the underlying silicon. Interestingly, however, it turns out that the rate of chemical etching by the silver film is much faster than that of silver particles, resulting in arrays of axially aligned Si NWs on a silicon substrate, as shown in the SEM image shown in fig. 1.21.b. where a silver particle on top of each Si NW can be seen. It can be argued that the Si/film contact has an energy barrier height smaller than the Si/particle contact one. Accordingly, it is easier for electrons to transport through the Si/film contact than through the Si/particle contact. Therefore, the etching assisted by the metal film might

31

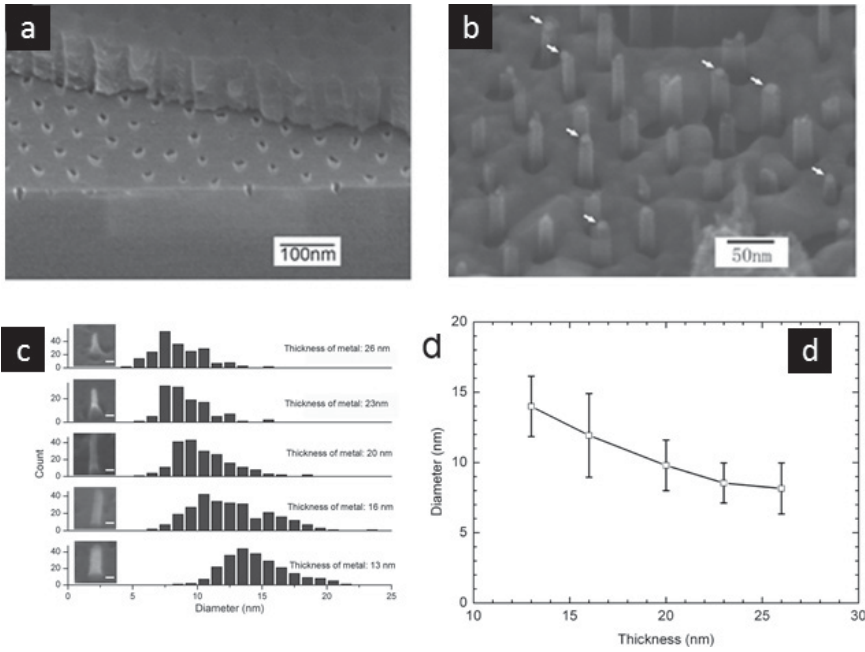Figure 1.21: *(a) Tilted SEM image showing a Si substrate partially covered by an AAO mask after a RIE process. Pits on Si surface are clearly visible. (b) Tilted SEM image of sub 10 nm Si NWs obtained by MACetch process in H_2O_2/HF applied to a Si substrate with a patterned silver layer. This pattern is transferred by the AAO mask. (c, d) Evolution of the Si NWs diameter as a function of the metal film thickness* [76].
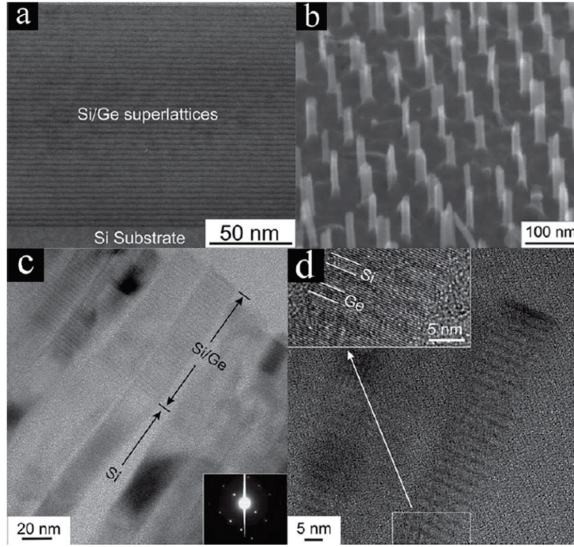
Figure 1.22: *(a) Cross-sectional TEM image of a layer of Si/Ge supper-lattice (40 periods) on Si substrate. (b) SEM image of Si/Ge nanowires fabricated by combining an AAO mask and a MACetch process. (c,inset of c, d, inset of d) Low, medium and high magnified respectively TEM images of a Si/Ge superlattice NW. The inset of c and the inset of d show the high crystallinity both of Si and of Ge and the maintained het-eroepitaxy also after the etching [75].*

be faster than that by metal particles. Alternatively, it might also be speculated that the surface of the etchpits were modified by the reactive ion etching process in such a way that metal-induced etch-ing is not possible any more. As discussed earlier, it is possible to control the diameter of Si NWs by varying the thickness of the metal film, since the diameter of Si NWs in the present process is determined by the diameter of the remaining pores in the metal film. Figures 1.21.c and 1.21.d show the evolution of the Si NWs diameter as a function of the metal film thickness. The average diameter is approximately inversely proportional to the thickness of the metal film, with a minimum achievable value of (8 ± 2) nm. In addition to Si nanowires, SiGe nanowires can also be fab-ricated using this method. Geyer et al. [75] applied the method to a substrate consisting of 40 periods of alternating Si (8.4 Å) and

Ge (2.1 Å) layers (fig. 1.22.a) and obtained sub-20-nm-diameter nanowires containing a Si/Ge superlattice (fig. 1.22.b). HR-TEM investigations showed a smooth surface of the Si/Ge superlattice nanowires (fig. 1.22.c) and a high-quality crystalline structure (fig. 1.22.d). After etching, the Si/Ge superlattice in an etched nanowire maintained the atomic structure and an abrupt Si/Ge interface exactly as in the unetched substrate. This result confirmed that the MACetching did not disturb the crystallographic structure of the Si/Ge superlattices.

Amorphous and Polycrystalline nanowires

It's clear that the MACetch technique is a performant technique to prepare Si NWs starting from crystalline Si. Moreover, S. Chang et al. demonstrated that the MACetch method when used with metal mesh with large hole spacings can be also extended to create arrays of polycrystalline and amorphous vertically aligned silicon nanowires by confining the etching to proceed in the normal direction to the substrate surface [74]. This is a fundamental aspect for low-cost nanotechnology, since the ability to pattern wires from polycrystalline and amorphous silicon thin films opens the possibility of making silicon nanowire array-based devices on a much wider range of low-cost substrates. Figure 1.23 shows etching results for both polycrystalline and amorphous silicon. In the case of isolated gold particles on polycrystalline silicon, etching proceeded in different directions for each particle. As shown in Figure 1.23.a, only a certain number of Au particles are able to sink into the polysilicon thin film and then sink into the underlying single-crystal (100) Si substrate. In fact, vertical etching was observed only in the underlying substrate. This was expected as isolated catalyst particles tend to move in the [100] direction. As a result of the random etching directions in the polycrystalline silicon, some of the Au particles never reached the polysilicon/substrate interface. For isolated gold particles on amorphous silicon, etching appeared to be mostly vertical with the particles moving collectively in the same direction. Although the actual etching direction could not be determined as the resulting structure lacked structural integrity and collapsed very easily, the vertical etching in the amorphous
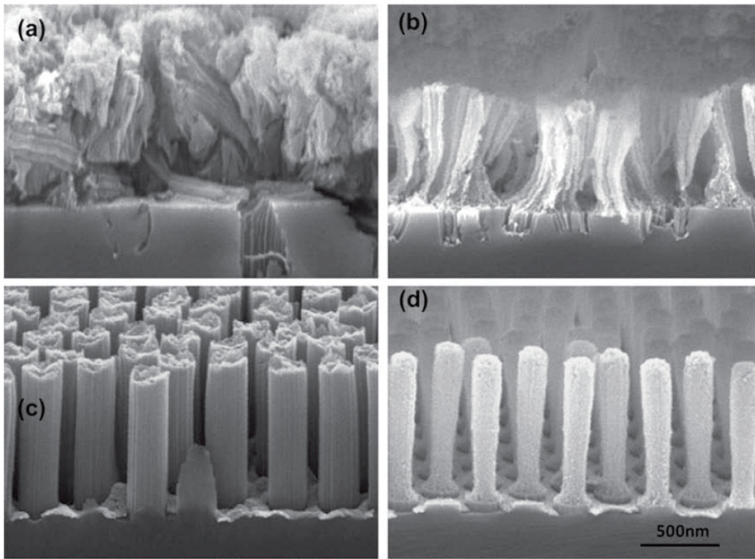
Figure 1.23: *(a) Cross sectional SEM image of the structure formed after a MACetch of isolated gold particles in polycrystalline Si, (b) or after a MACetch of isolated gold particles in amorphous Si. (c) Cross sectional SEM image of the structure formed after a MACetch of a template-prepared gold mesh in polycrystalline Si (d) or in amorphous Si[74].*

silicon layer can be confirmed by the relatively high ratio of Au particles that reached the amorphous/substrate interface and continued to catalyze etching into the (100) Si substrate, as shown in Figure 1.23.b. The collective movement suggested some type of interaction with neighboring particles. In the case of metal meshes with relatively large hole spacings, etching proceeded in the vertical direction for both polycrystalline and amorphous films, as expected. 1.23.c and fig. 1.23.d show polysilicon and amorphous silicon nanopillars, respectively. These pillars or wire arrays made from polycrystalline and amorphous films are of special interest for device applications because they can be formed on a very wide array of substrates, including large-area, conformable substrates, and are not restricted by the use of costly single crystal wafers. In addition, polycrystalline and amorphous films can be deposited at relatively low temperatures, allowing further flexibility in substrate selection and the possibility of stacking of nanowire arrays without severe constraints. For example, solar cells based on planar amorphous silicon [78] and microcrystalline silicon [79] have well-established commercial markets. High surface-to-volume ratio nanostructures based on amorphous and polysilicon patterned arrays may be desirable as potential materials for solar cell photoanodes. Detailed examples of low cost Si NWs made solar cells will be shown in the next section, together with other device applications of Si NWs in sensors, nanoelectronics and optics.

1.2 Device applications

The new optical and electrical properties due to the specific dimensionality and predominant surface phenomena in Si NWs have been used in the last decade for different applications. As an example, finding a way to decrease the cost of solar cells is a crucial aspect of energy harvesting. Although most commercial solar cells are fabricated from silicon, and are made of planar p-n junctions, silicon has a relatively low absorption coefficient throughout much of the visible and near-infrared parts of the electromagnetic spectrum. Since the vast majority of the light from the sun is in this range, silicon-based solar cells must be thick in order to collect most

of the incident photons. For example, a silicon cell must be several micrometers to millimeters thick to absorb 90% of the incident light at wavelengths from 700 to 1100 nm, respectively, which comprise about one-half of the solar energy available above the band gap of silicon. Si NWs are a good solution to use less silicon in solar cells . Inf fact, it has been demonstrated that forests or quasi random arrays of aligned Si NWs can trap light very well, due to light scattering in the NWs media. Moreover, the collection efficiency of charge carriers generated at a given distance from the junction depends on the minority carrier diffusion length in the n- and p-type quasineutral regions. The detrimental effect of the recombination current in solar cells, can be avoided by realizing radial junctions in NWs with a diameter less than the recombination length of the minority carriers. This can definitely increase the collection of photo-generated carriers. Then, the high surface to volume ratio and the large percentage of dangling bonds on the surface of Si NWs can increase their availability to be functionalized with suitable molecules which detect selectively other gases or biological molecules. Once functionalized and once inserted into an electronic device, Si NWs show different electronic conduction properties depending on the coupling with these molecules. This makes them promising sensors at the nanoscale. These surface effects, which will be treated in the next paragraph gave rise to a strong interest in the biological science which, in recent years, is mixing his knowledge with nanotechnology. Obviously, their small dimensions are interesting for nanoelectronics. Several attempts of making MOS-like devices with silicon nanowires have been made in the last years. In fact, scaling down CMOS technology is a key aspect of progress in IC factories, and has its paradigm on the Moore's law. On the other side, Si NWs with radii of a few nanometers are suitable for photonics, since their radial dimension are less than or comparable with the De Broglie wavelength of the electron-hole excitonic pairs in Si. In fact, light emission from Si NWs is achievable and has been demonstrated by different groups, with different explanations, i.e. quantum confinement[19, 46], impurities[80], defects and surface states, quantum shaped roughness and molecular complexes on their surface [81, 82]. Regardless of the origin of this luminescence, an aspect which is still lacking in literature is elec-

trical pumping of Si NWs. To this purpose, we will see in chapter 3 that electroluminescence in Si NWs is possible, and can give rise to low cost emitters for silicon photonics.

1.2.1 Solar cells

All the world is requiring more and more energy every second. Let's imagine that writing this thesis too on my laptop is requiring power in this very moment, printing it will require paper and ink, that have to be made, hence more energy and so on. Different renewable sources (wind, solar, water waves), or even low impact non-renewable energies (geothermal, hydrates, biofuels, nuclear power plants, etc..) have been proposed for energy harvesting in the last years. It's quite obvious that only the right combination of these different energetic solutions, together with an effort on lowering the energy demand (LED lighting, low power computers, high efficiency cars, etc.), could be the answer to the energetic problem. Crystalline silicon is perfect for outdoor light absorption and carriers collection but, in the visible and IR range has got a low absorption coefficient, hence generally a large amount of Si is required for conventional solar cells. On the contrary, Si NWs could be a promising solution for low cost and high efficiency 3rd generation solar cells. The idea, and the final goal, is to have a small amount of high purity and crystalline grade Silicon on whatever kind of low cost substrate. High aspect ratio nanorods allow the use of a sufficient thickness of material to obtain good optical absorption while simultaneously providing short collection lengths for excited carriers in a direction normal to the light absorption. The short collection lengths facilitate the efficient collection of photogenerated carriers in materials with low minority-carrier diffusion lengths [83]. On the other side a NWs medium in which light can scatter can increase light absorption and the efficiency to collect light not normal to the surface of the solar cell. In fact, sun is not a laser! Most of the times, light collected from solar cells is scattered by the clouds, or trivially sun is not perpendicular to the solar cells. Let's have a look on how a solar cells made of NWs can work, and let's start with the radial p-n junction. Figure 1.24.a and 1.24.b show a schematic picture and cross-sectional scanning electron micrograph (SEM) of a
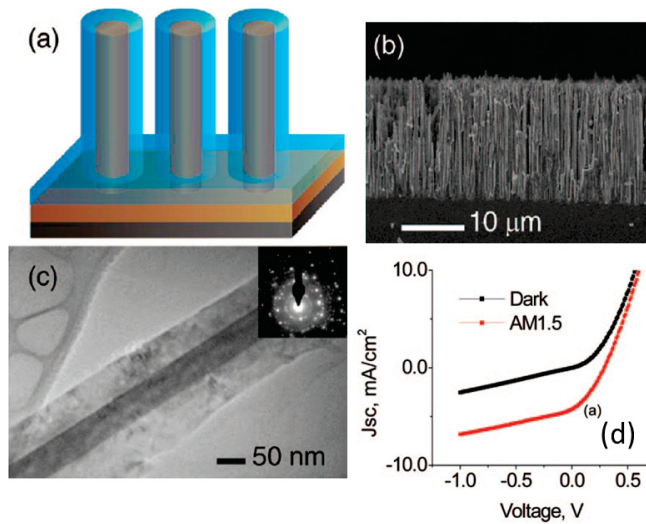
Figure 1.24: *(a) A scheme of a coaxial p-n junction based on Si NWs. (b) Cross-sectional SEM view of a Si NW n-p core-shell solar cell after the amorphous silicon deposition and crystallization. (c) BF TEM view of this coaxial p- junction. (d) Current-voltage characteristics of this solar cell [84].*

39

Si NW n-p core-shell solar cell after the amorphous silicon LPCVD deposition and crystallization. Such a device has been made by E. Garnet et al. [84]. The device shows 18 μm long nanowires with excellent vertical alignment, uniformity, and packing density, with about 50% areal density. The typical wire diameter (including the shell) from the SEM is 350-400 nm, which gives a shell thickness of about 150 nm on top of the 50-100 nm initial nanowire core. The coaxial junction of a thinner core-shell NW is clearly visible in the TEM image of fig. 1.24.c. In this bright field image, the single crystalline core is aligned to a zone axis, leading to much stronger diffraction and thus darker contrast compared to the polycrystalline shell. Figure 1.24.d shows the electrical output characteristics of a Si NW array PV. Under AM 1.5 illumination, the device has an open circuit voltage (V_{oc}) of 0.29 V, a short circuit current (J_{sc}) of $4.28 mA/cm^2$, and a fill factor (FF) of 0.33 for an overall efficiency of 0.46%. This low efficiency is probably due to a low V_{oc} due to an interfacial recombination. The high surface to volume ratio in the nanowire arrays is expected to exacerbate recombination, making surface passivation even more important for these devices than for bulk silicon solar cells. The large surface roughness could also lead to enhanced depletion region traps, especially since this surface is located directly at the p-n junction in the final device. Obviously, future studies will focus on limiting this interfacial recombination by passivating the surface and reducing roughness while increasing the p-Si conductivity to minimize the series resistance. Scattering of light in Si NWs media has been studied both theoretically [85] and experimentally [86]. Figure 1.25 shows an example wire array of each of the seven patterns of Si NWs investigated by Kelzenberg et al [86]. Following peel-off, the transmitted optical diffraction patterns (third row) were used to orient the wire lattice patterns relative to the tilt directions (θ_x, θ_y), and angularly resolved transmission measurements were carried out (bottom row). Owing to the vertical orientation of the wires, all of the arrays showed lower absorption at normal incidence ($\theta_x, \theta_y = 0$), than at other angles. The well-aligned rows and columns of wires produced by periodic arrangements led to greater areal packing fractions (and thus higher overall optical absorption) than were obtained by quasi-periodic or random arrangements. However, the periodic arrange-
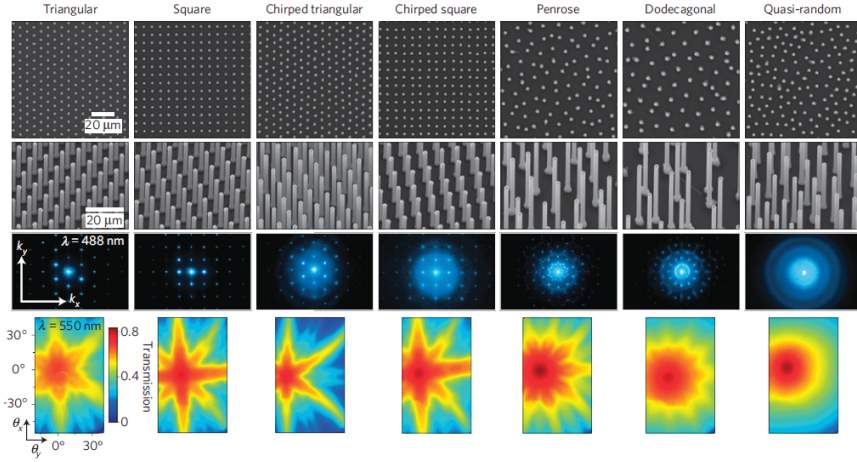
Figure 1.25: *(first and second rows) Top view and tilt-view SEM images of arrays of NWs made by EBL and RIE. Moving from the left to the right the grade of disorder in their distribution increases. (third row) Transmitted optical diffraction patterns of a laser light at 488 nm scattering on this arrays. (bottom row) Angularly resolved transmission measurements [86].*

ments also showed a strongly anisotropic angular absorption profile, which would produce low-absorbing "dead spots" in a photovoltaic device. For Si wire arrays to achieve maximal absorption over the relevant wavelengths and incidence angles of solar illumination, the reflectivity of the Si surfaces must be reduced, and the light passing between the wires must be randomized. Figure 1.26 shows the the light-trapping tricks that can be used to maximize the absorption of Si wires. The wire array can be placed in a mirror like Ag back reflector (fig. 1.26.a-b) to emulate a metal back contact as well to increase the optical path length within the array. Although this step substantially increases the absorption of the array, the normal-incidence absorption remains significantly weaker than that at off-normal-incidence angles. To further improve absorption, two more light-trapping measures can be implemented on a different portion of the wire array. For example, a SiN_x antireflective coating can be conformally deposited onto the tops and sides of these wires. In addition, Al_2O_3 particles (900 nm nominal diameter) were added to the polydimethylsiloxane (PDMS) infill, to scatter the light that
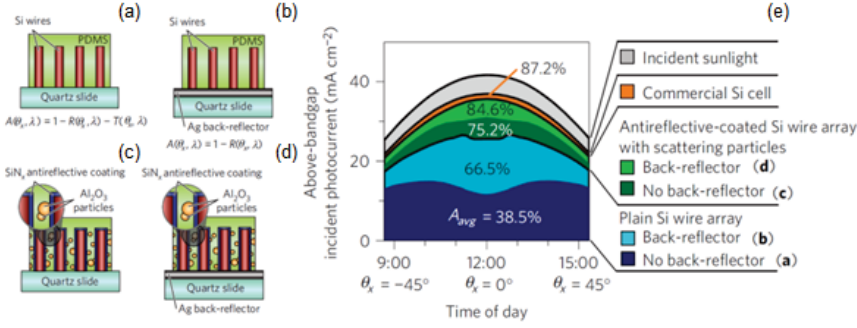
Figure 1.26: *(a) Some tricks useful to increase the path of the light in the Si NWs media, by using a back reflector (b), or a SiN_x antireflective coating and Al_2O_3 particles (c), or a combination of all these methods (d). (e) Above-bandgap incident photocurrent in a day by these different solar cells, compared to a commercial solar cell made by the same amount of Si of the Si NWs solar cell [86].*

might otherwise pass between the wires (fig. 1.26.c). These materials were chosen because they have negligible absorption across the visible, and thus enabled the direct observation of absorption enhancement within the Si wires themselves. These light-trapping measures virtually eliminate the angular sensitivity of the wire array's absorption, and increase the peak normal-incidence absorption to 0.92. When placed on a Ag back-reflector, the array's peak absorption increased to 0.96 (fig. 1.26.d). Figure 1.26.e shows the above-bandgap incident photocurrent (proportional to the mean number of photon absorbed) in different hours of the day for these different kinds of solar cells depicted in fig. 1.26.a-d. Data are compared to a commercial solar cell with the same amount of silicon. On the basis of bulk Si properties and neglecting interference effects, two theoretical absorption limits were calculated for the equivalently thick Si slab (fig. 1.27): A_{Si}, which results from the use of bare, non-textured Si surfaces (black), and A_{LT}, which results from ideal classical light-trapping at the Si surfaces (blue). The latter case, the "ergodic limit", is the maximally achievable absorption (in the ray-optic limit) of a planar-sheet absorber that uses ideally random (for example, Lambertian) light-trapping [87]. As shown in fig. 1.27.a, the wire array's absorption exceeded the
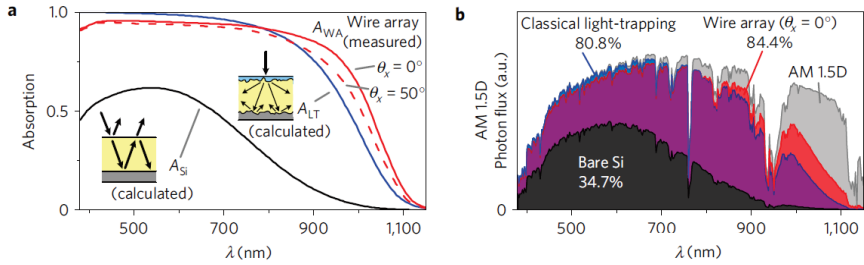
Figure 1.27:   *Theoretical calculations (a) and experimental measurements (b) of the wire array optical absorption, exceeding the ergodic limit (due to classic random scattering) at high wavelengths* [86].

planar light-trapping ergodic limit for infrared wavelengths (>800 nm). This behavior exemplifies a useful property of microstructured, non-planar absorber geometries (including wire arrays), in that they can achieve greater absorption per material volume than achievable by a randomly textured, planar-sheet absorber geometry. This effect has been simulated for Si wire arrays [85]. Figure 1.27.b shows, using the AM 1.5D spectrum at normal incidence, that the enhanced infrared absorption of the Si wire array yielded a greater overall absorption of above-bandgap photons than the equivalently thick, ideally light-trapping planar absorber. Taking all measured incidence angles into account, the day-integrated absorption of the wire array slightly exceeded that of the planar light-trapping case. Thus, the Si wire-array geometry can enable solar cells that reach, and potentially even exceed, the theoretical absorption limit, per volume of Si, of ergodic-limited random light trapping.

1.2.2   Sensors

The large amount of surface charge, which is a disadvantage in Si NWs junctions for solar cells, can be an important resource for sensing. The sensors based upon Si NWs could be generally understood in terms of change of surface charge of the NWs with the presence or absence of molecular species [88]. Because of the high surface-to-volume ratio of the NWs, their electronic conductance may be sensitive enough to the surface species that single molecule detection becomes possible. Z. Li et al. [88] demonstrated the detection
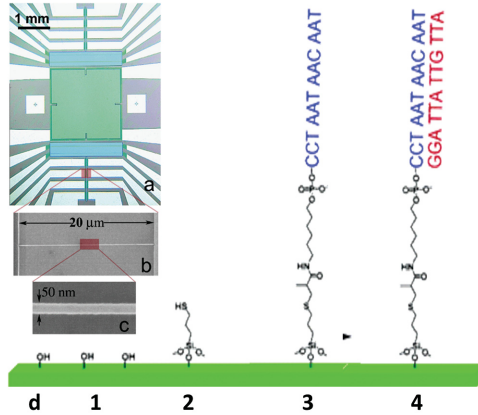
Figure 1.28: *Optical microscopy (a) and SEM top view images (b and c) of a DNA-sensor based on a Si NWs sensing part. (d) A scheme of the different steps of functionalizing this Si NW in order to link specific sequences of DNA [88].*

of DNA molecules based on their intrinsic charge by using Si NWs fabricated by a standard "top-down" process. Si-based nanoscale sensors with a set of Si NWs 50 nm wide, 60 nm high, and 20 μm long were fabricated using silicon-on-insulator (SOI) wafers. Figure 1.28.a-c shows a typical microscopic image of a sensor chip and the scanning electron microscope (SEM) images of the Si NW portion. Si NWs have been doped with boron concentration between 10^{16} and 10^{19} at/cm^3. Finally, to eliminate any interference from the electronic leads during sensor tests, the area outside of the Si NW regions was coated with a 100 nm silicon oxide layer. Thus, only the Si NWs were exposed to the environment during sensor testing. Surface modification of the Si NW is a crucial aspect of the final device. First, the surface of the Si NWs was treated with a water-vapor plasma. The plasma treatment cleaned the sample surfaces and generated a hydrophilic surface by hydroxy-terminating the silicon oxide surfaces (see fig.1.28.d.1) . A self-assembled monolayer with free thiols on the surface was then prepared using a gas-phase method, as shown in fig. 1.28.d.2. Then, the immobilization of ss-DNA probes was achieved by exposing the thiol-covered samples into a solution of oligonucletides (see fig.1.28.d.3). This device is
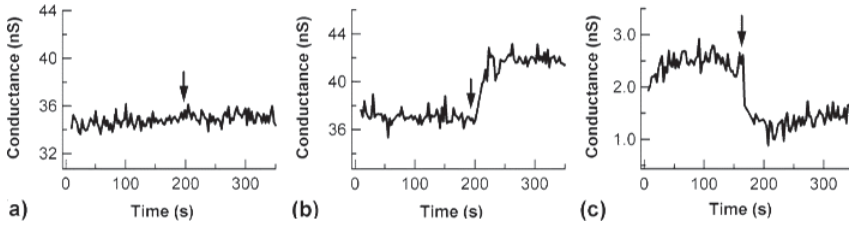
Figure 1.29: *Conductance measurements of a boron-doped p-type NW in a solution containing non-complementary DNA (a) and in another containing complementary DNA (b). (c) Conductance measurements for a phosphorous doped n-type NW in a solution containing complementary DNA [88].*

capable to link selectively to specific sequences of DNA, and then detect them via changes in the conductance. In fact, fig. 1.29.a-b and 1.29.c show the different conductance traces of a boron-doped p-type wire ($c = 10^{19} cm^{-3}$) and a phosphorus-doped, n-type sample ($c = 10^{18} cm^{-3}$) respectively. Control experiments with non-complementary DNA with a single-base mismatch did not change the conductance of the SiNWs above the noise level (as shown in fig. 1.29.a). On the other hand, the realtime increase of the conductance of the p-type Si NW upon the addition of complementary ss-DNA was observed (fig. 1.29.b). A similar change of the magnitude of the conductance was observed in n-type samples, but in the opposite direction (see fig. 1.29.c).

As another sensing application, Si NWs can also be used for detecting gases or materials with a very low vapor pressure (<10 ppb). In fact, they can be successfully applied on 2,4,6 trinitrotoluene (TNT) detection [89]. TNT is one of the most commonly used explosives. In general, a successful chemical sensor for TNT and other explosives must be extremely sensitive given that the vapor pressure at 25 °C is less than 10 ppb, must be highly selective, must have the ability to be easily miniaturized for field application and finally has to be able to perform real-time high throughput analysis based on arrays of multiple sensing elements. For NW sensors operated as field effect transistors (FETs), the sensing mechanism is the field-gating effect of charged molecules on the carrier conduction inside
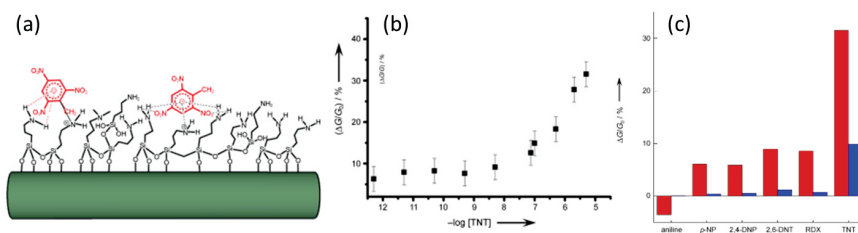
Figure 1.30: *(a) Schematic view of a Si NW functionalized structure for sensing of TNT molecules. (b) Sensitivity of the corespondent Si NWs TNT sensor array. (c) Reactivity of this sensor to other nitroaromatic chemical derivates of TNT [89].*

the NW. Y. Engel et al. demonstrated supersensitive and rapid detection of TNT in real time with the use of large-scale arrays of Si NW-FET devices (this electronic device will be described better in the next paragraph) [89]. Nanowire sensor arrays were fabricated and subsequently OH-terminated and chemically modified with a sensing array layer (fig. 1.30.a) useful for the detection of explosive species. When the electron-deficient TNT molecules bond with the sensing array molecules, their positive charge acts in the NW conduction the role of a gate charge in a MOSFET, hence it modifies the conductivity of the NW by bending his inner bands. Figure 1.30.b shows the sensing of TNT by the nanowire sensor array. The exceptional performance of the Si NW devices enables the detection of TNT with unprecedented sensitivities reaching sub-femtomolar ($< 10^{-15}M$) concentrations. Finally, they investigated also the reactivity of the sensor to structurally related nitroaromatic chemical derivatives (see fig. 1.30.c). The results clearly show a strong preference for binding TNT over these compounds. In fact, molecules such as TNT have a higher ability to create charge-transfer complexes with the amino-modified monolayer, hence they induce a stronger conductivity change than other nitrosubstituted aromatic molecules.
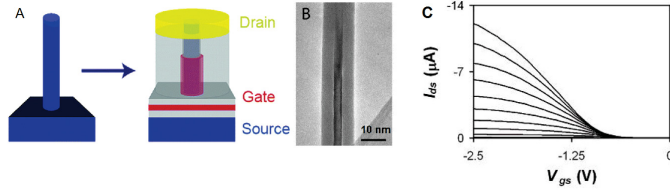
Figure 1.31: *(a) A sketch of the fabrication of a Si NWS FET device. (b) BF TEM image of a Si NW after oxidation process, with a crystalline core of 5 nm, which constitutes the channel of this FET device. (c) I_{ds} vs V_{gs} with V_{ds} ranging from -2.5 to -0.25 V from top to bottom [90].*

1.2.3   Nanoelectronics

Si NWs have received great attention as transistor components because they represent a simple route toward sub-10-nm single-crystalline Si features. The IC manufacturing roadmap of top IC factories is moving to the sub-10 nm scale ULSI in the next five years. Nanowire materials offer a number of benefits over conventional planar materials for field-effect transistor (FET) applications. First, nanowires offer the option of creating gate-all-around (GAA) architectures, which allow for more efficient control over charge carriers in the channel of FET devices, thus reducing short channel effects caused by drain induced barrier lowering (punch-through). From an applied research approach, J. Goldberger et al. demonstrated the direct vertical integration of Si nanowire arrays into surrounding gate field effect transistors without the need for postgrowth nanowire assembly processes [90]. The FET device fabrication allows Si nanowire channel diameters to be readily reduced to the 5-nm regime. Figure 1.31.a is a schematic of the FET design. This device has been fabricated using conventional very-large-scale integration (VLSI) processing. Vertical silicon nanowire arrays were thermally oxidized to create uniform SiO_2 layers as dielectrics. A typical device has a 20-30 nm diameter Si nanowire surrounded by 30-40 nm of high-temperature gate oxide, a Cr metal gate length of 500-600 nm, and nanowire channel lengths that range from 1.0 to 1.5 μm. The gate-oxide thickness and channel diameter are visible in the TEM image of fig. 1.31.b. Significantly, the channel diameter can be readily reduced below 5 nm. Typical drain-source
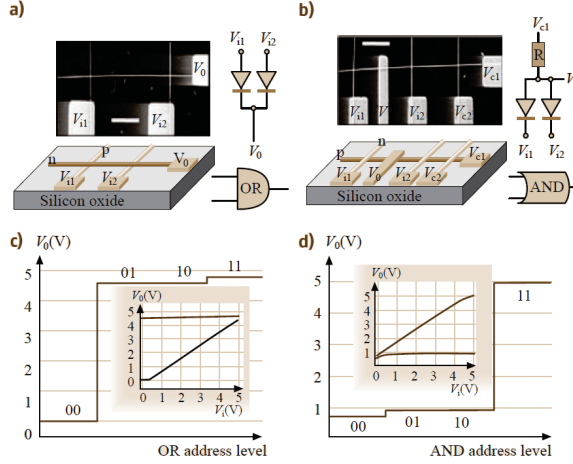
Figure 1.32: *(a) Two p-type Si NWs and one n-type GaN NW form two crossed p-n junctions, and realize an OR logic gate. (b) Coupling a p-type Si NW and three n-type GaN NWs and AND logic gate is achieved. (c and d) Output voltage at the four different input conditions at the OR and AND gates respectively [91].*

current (I_{ds}) vs drain-source voltage (V_{ds}) measurements at various gate voltages (V_{gs}) indicated that B-doped Si NW FET behaves as accumulation-mode p-type transistors. The application of a negative (positive) V_{gs} results in an increase (decrease) of I_{ds}, due to the increase (decrease) of majority hole carriers. carriers. The V_{gs} value at which the I_{ds} is effectively turned on and accumulation begins is defined as the threshold voltage (V_t). V_t is clearly seen in the plot of I_{ds} vs V_{gs} at different V_{ds} values for the same device (fig. 1.31.c). These first-generation vertically integrated Si NWs FET exhibit electronic properties that are comparable to other horizontal nanowire field effect transistors (FETs) and may, with further optimization, compete with advanced solid-state nanoelectronic devices. Another approach to make nanoelectronic devices with silicon nanowires is try to couple these system with other NWs made by different materials and with a different doping type. In this way, uniformly doped Si NWs can be the base bricks for many electronic devices. Silicon NWs FETs doped with boron or phosphorous have performances similar to the best planar devices made with the same materials [90, 91]. Moreover, a high electronic mobility in InAs NWs

48

FETs has been observed. These two kind of NWs can be assembled and cross-coupled in order to form logic gates. Figure 1.32.a shows two p-type Si NWs and one n-type GaN NW that form two crossed p-n junctions, and realize an OR logic gate. Coupling the same kind of NWs in a different manner, i.e. coupling a p-type Si NW and three n-type GaN NWs, as shown in fig. 1.32.b an AND logic gate can be achieved. The output voltages [0; 5V] of the device in different input conditions [i.e. (0,0); (0,1); (1,0); (1,1)] are represented in figure fig. 1.32.c and fig. 1.32.d for both the OR and the AND gate respectively.

1.2.4 Photonics

As an indirect band-gap semiconductor, bulk Si is an inefficient light emitter relative to its direct-gap counterparts, with photoluminescence PL external quantum efficiencies (EQE) reaching 10% in only specially prepared high-quality substrates [92]. However, efficient PL has been observed in various nanostructured Si material systems, such as porous Si and Si nanocrystals (Si-nc) within dielectric matrices [93, 94]. At the same time, Si NWs have great optical properties, which make them suitable for photonic applications. Different groups have already reported in literature a light emission from Si NWs grown by a variety of synthesis techniques [46, 19, 47]. In this scenario, different interpretations of the origin of photoluminescence (PL) have been given in these years, i.e. quantum confinement of excitons supported by PL lifetime studies and the tuning of photoluminescence by changing the diameter of the NW [47, 19], radiative recombination from surface states at $Si-SiO_2$ interfaces, impurity-center recombination within the crystal, defects in the passivating oxide, and chemiluminescence from linear Si-chain molecules, as syloxene composites [95]. As an example, Guichard et al. *[47]* presented an in-depth study of the optical emission from $TiSi_2$-catalyzed VLS-made Si NWs and showed that the data are fully consistent with the NW PL being due to radiative recombination of quantum-confined excitons inside the Si NWs. They demonstrated for the first time that Si NWs photoluminescence can be tuned by controlling the NW diameter. To this end they performed a combined TEM, PL, and a time-resolved
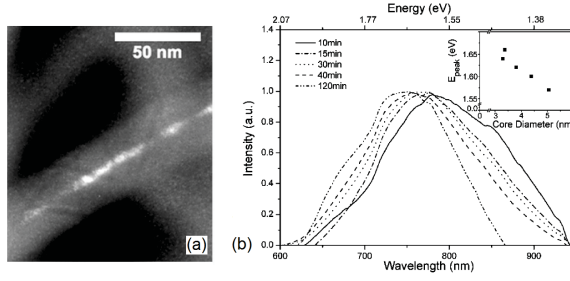
Figure 1.33: *(a) DF TEM image of a $TiSi_2$ catalyzed VLS grown Si NW, a silicon crystalline core is clearly visible. (b) Normalized PL spectra of Si NWs after thermal oxidation for 10, 15, 30, 40, and 120 min. (b, inset) Plot of the PL peak energy vs average Si nanowire diameter measured by DF-TEM [47].*

PL study of the size-dependent optical properties of the Si NWs. They have grown $TiSi_2$-catalyzed Si NWs by depositing Ti on an Sb-doped, n-type Si(100) wafer. The samples were then annealed at 900 °C in H_2 for 5 min to form $TiSi_2$ catalyst islands. To grow Si NWs, the samples were exposed to a mixture of SiH_4, HCl, and H_2 at 680 °C for 30 min, by VLS process. Following NWs growth, the samples were etched in 2% HF for 1 min to remove the native oxide from the NWs. The samples were then thermally oxidized at 950 °C in dry O_2 for times ranging from 10 to 120 min. The dark field HR-TEM micrographs in fig. 1.33.a depicts a NW after thermal oxidation for 30 min.The contrast between the c-Si core and the amorphous oxide around it is clearly visible. As for other experiments performed by other groups [19], a self-limited shrinking of the core of Si NWs has been observed, and in their case a self-limited crystalline Si NW core diameter of about 3.3 nm has been found. Figure 1.33.b shows normalized PL spectra of Si NWs after thermal oxidation for 10, 15, 30, 40, and 120 min.

After 10 min of oxidation, a broad luminescence band is observed, peaking at 1.55 eV (800 nm) (fig. 1.33.b). For longer oxidation times, the luminescence band maintains a constant full width half maximum (FWHM) and shifts to the blue. For short oxidation times, the peak energy shifts rapidly with increasing oxidation time, and for longer oxidation times the peak energy saturates at around
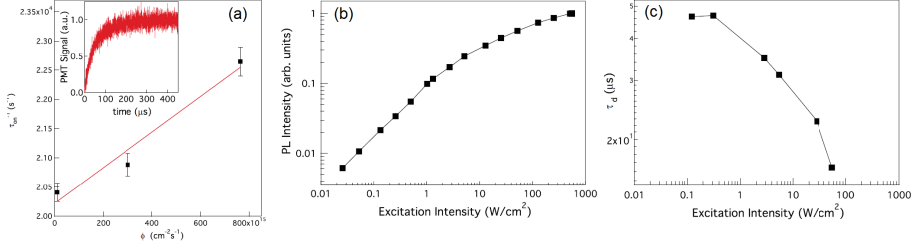
Figure 1.34: *(a) Room temperature excitation rate, τ_{on}^{-1} as a function of excitation photon flux ϕ for low pumping regimes. The slope of the fit represents the excitation cross section of $TiSi_2$ catalyzed VLS grown Si NWs. (b) PL intensity vs the excitation intensity I_{ex}. (c) Decay lifetime as a function of I_{ex} [46].*

1.66 eV, consistent with a self-limited NW diameter. The inset shows a plot of the PL peak energy vs average Si nanowire diameter measured by DF-TEM, demonstrating the blue shift of peak luminescence wavelength with decreasing diameter. Another indirect proof of Si NWs quantum confinement emission is represented by an excitation cross section similar to the one measured in Si nanocrystals embedded in silica matrix, since these ones show photoluminescence due to quantum confinement. The excitation cross section can be found by considering the state-filling equations in the low-pump-power regime, where Auger recombination (AR) can be ignored. The procedure adopted by Guichard et al. is similar to the one used for Si nanocrystals [96]. The pump-power-dependent-PL risetime, τ_{on}^{-1} is given as a function of the excitation photon flux, ϕ: $\tau_{on}^{-1}(\phi) = \sigma\phi + \tau_{d,0}^{-1}$. Figure 1.34.a is a plot of room temperature excitation rate, τ_{on}^{-1} as a function of excitation photon flux ϕ for low pumping regimes, at which the PL intensity goes linearly with the pumping photon flux because non-radiative phenomena are suppressed. By fitting these data, they obtained an excitation cross section of $\sigma = 3 \times 10^{-15} cm^2$, just an order of magnitude higher than the one measured for Si nanocrystals. It's likely that the increase in σ is due to increased optical excitation field strength inside the wire as compared to a spherical geometry. However, the long radiative lifetime in these systems means that short lifetime nonradiative processes can dominate at high pump powers. In fact,

at higher pump fluxes a high amount of carriers is injected and the Auger recombination process (AR) starts to be competitive with radiative recombination of excitons. This phenomenon is visible in fig. 1.34.b and fig. 1.34.c. They show both the PL intensity and the decay lifetime as functions of excitation intensity, I_{ex}. These two quantities exhibit two distinct regimes. At low excitation conditions, the PL intensity scales linearly with I_{ex}, giving rise to a slope of about 1 in the log-log plot. Above 1 W/cm^2, the PL power law becomes sublinear. The decay lifetime is constant at low-pump intensity, but decreases at intensities above a similar threshold. The size and dimensionality of a semiconductor is known to greatly affect the character and rate of the Auger process. In most bulk semiconductor systems at room temperature, including Si, AR occurs via a process involving three free carriers, and the PL decay rate (the reciprocal lifetime) is proportional to the square of the carrier concentration, n^2. In contrast, one-dimensional 1D structures can exhibit increased electron-hole overlap and dielectric constant mismatch between the host wire and its surroundings. This can result in an exciton binding energy that exceeds the thermal energy, $k_B T$. In this case, the majority of the excited carriers are in the form of excitons and AR occurs in the form of exciton-exciton or so-called bi-molecular annihilation. Since this process involves two bound electron-hole pairs or particles, this bi-molecular AR rate scales linearly with N [46].

A tuning of the visible PL of Si NWs towards higher energies has been observed by Walavalkar et al. on EBL-made Si NWs (see paragraph 1.1.2 for details about their preparation). These NWs have been oxidized to shrink the crystalline core, they are 1 μm tall and exhibit a diameter of the crystalline core tunable in the range between 2 and 8 nm, hence they show a quantum confinement of excitons inside the crystalline core higher than the ones fabricated by Guichard (which could reach a minimum diameter value of 3.5 nm).

Photoluminescence was observed between 600-800 nm (1.5-1.9 eV), as shown in fig. 1.35.a. The data show a strong blue shift in peak emission wavelength corresponding to a decrease of the silicon core diameter. The peak wavelength versus core diameter is plotted
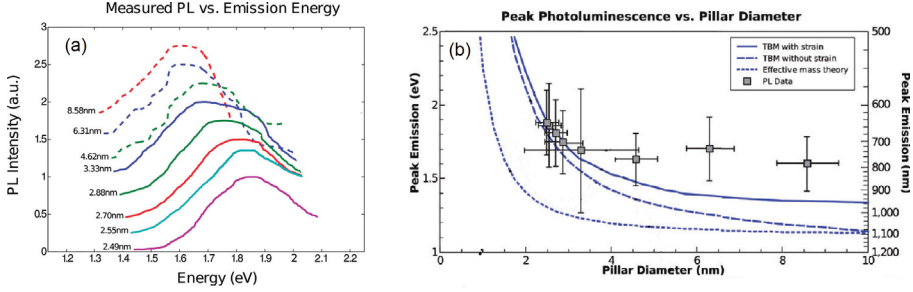
Figure 1.35: *(a) PL spectra at different radii of EBL made Si NWs. (b) Peak wavelength vs core diameter[19].*

in fig. 1.35.b. Walavalkar et al. [19] measured decay times in the range of hundred of nanoseconds (two orders of magnitude less than the ones measured by Guichard et al. in $TiSi_2$ catalyzed VLS grown Si NWs) and found that they are decreasing with narrowing of the core diameter [19]. Probably in smallest Si NWs a possible increase of the overlap between the hole and electron wavefunctions is responsible of increasing the recombination rate [47].

To further look into the origin of electron-hole recombination, Walavalkar et al made computational calculations on the bands of [100] Si NWs. These theoretical calculations have found the strain in nanowires, due to the SiO_2 shell, to be important in increasing the splitting between the Γ conduction band valley and the bulk indirect X direction valley. For pillars with diameters less than 10 nm experiencing tensile strain in the radial and circumferential direction, the splitting between these two minima is several times the room temperature thermal energy kT, as seen in the solid lines of fig. 1.36. This large splitting allows the excited electrons to sit in the Γ valley, allowing for a faster, direct optical transition. For unstrained or compressively strained pillars (dotted line in fig. 1.36) the splitting between the two valleys is closer to the thermal energy forcing carriers to sit both in the Γ as well as the X valley, requiring a longer phonon-assisted recombination.

However, similar photoluminescence spectra have also been observed in thicker Si NWs made with a completely different approach. In fact, V. Sivakov et al. *[81]* observed a strong room temperature PL emission from Si NWs obtained by MACetch process of heavily
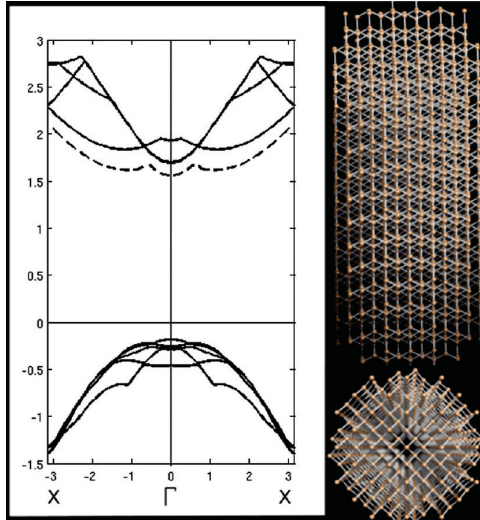
Figure 1.36: *Band-structure (in eV) of a TBM simulation of a strained and unstrained 2.5 nm diameter silicon nanowire. The dotted line shows the relative conduction band edge for the unstrained wire while the two insets show the axial and transverse structure of the nanowire [19].*
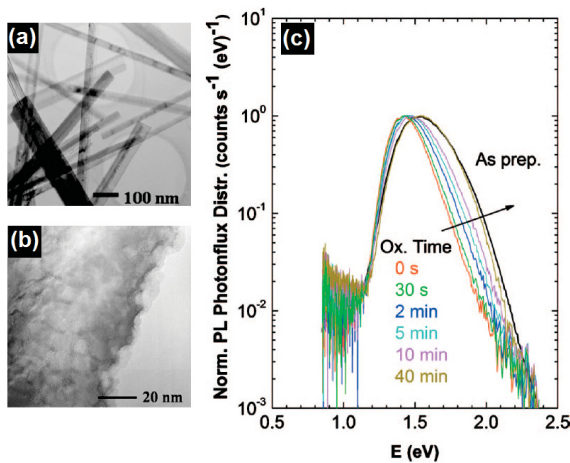
Figure 1.37: *(a) Low-mag. and (b) high-mag. BF TEM images of MACetch Si NWs obtained using a solution containing AgNO$_3$ salt and HF. A rough surface is clearly visible. (c) Normalized PL intensity as a function of the oxidation time. [81].*

(As: $10^{20} cm^{-3}$) doped [100]-oriented Si wafer, using a deep bath in a solution containing $AgNO_3$ salt and HF acid. The Si NWs they obtained have diameter varying from 30 to 200 nm , with an average diameter of approximately 70 nm, as depicted in the bright field (BF) TEM image of fig. 1.37.a. All Si NWs are single crystalline and are coated by a thin native silicon oxide layer and, in contrast to the smooth surfaces of typical VLS grown Si NWs the surfaces of etched Si NWs are much rougher as shown in the BF TEM in fig. 1.37.b. The average surface roughness of etched Si NWs was typically 2.5 - 3.5 nm measured from peak to valley. The formation of rough surfaces during the Si NW etching may be related to the silver nanoparticle enhanced local Si oxidation and subsequent oxide etching and further to migration of silver nanoparticles along the Si NWs sidewalls during the etching process. Figure 1.37.c shows normalized PL spectra of the wet chemically etched heavily doped c-Si before and after treatment with 2.5% HF for 3 min and during reoxidation under air atmosphere. The blue-shift in PL spectra during reoxidation in fig. 1.37.c can be associated with the growth of native oxide layers on the silicon nanowires surfaces that also was specified in the TEM micrographs as shown in fig. 1.37.b, where a 2–3 nm thick native oxide layer is clearly visible in as-prepared Si NWs surface. Sivakov and al. argued that the quantum confinement interpretation appears to be the most probable interpretation of the room temperature visible PL for their samples, and proposed that for their Si NWs the PL is related to nanoscale periodically rough sidewalls.

Conclusions

Different strategies for Si NWs realization, adopted worldwide by different research groups, have been shown in this chapter. In particular, VLS growth is the most common bottom-up technique, based on metallic catalysts and on physical or chemical vapor deposition of molecules containing silicon. This technique is limited by the thermodynamics of the Si-metal alloy and by the kinetics of diffusion of silicon from the vapor phase into each NW. Gold is the most common metal catalyst adopted for VLS growth, for

several reasons: it is inert, it forms a liquid alloy with Si at low eutectic temperatures, compatible with VLSI processing. By the way, it has been shown that gold diffuses into the NW and on the sidewalls of it during the growth itself. Gold puts midgap electronic energy levels into the band diagram of silicon. Therefore, it increases the probability of non radiative recombinations of carriers, becoming a lifetime killer for slow radiative processes typical in nanosized silicon. This issue affects both optical and electrical properties of these interesting new materials. To solve this problem different strategies have been adopted, i.e. changing the catalyst or changing the method of preparation of NWs. In fact different groups prepared NWs by using lithography and reactive ion etching processes. This is a powerful technique, fully compatible with CMOS processing, but with the main issue of being very expensive and extremely time consuming. It is impossible to make wafer scale NWs by electron beam lithography, since the writing time of this kind of lithography for a whole wafer is too slow and comparable to human life. Si NWs can be useful for several applications of tomorrow: due to their high surface to volume ratio they can be promptly used as sensors, or because of their dimensionality can be used as all-around-gate field effect transistors, or thanks to their vertical alignment (and their strong scattering of the light among them) they can be used for radial solar cells. Unfortunately, it is nevertheless true that only NWs with features of a few nanometers are suitable for photonic applications, since the exciton radius in Si is about 5 nm. Then, both the VLS made NWs (whose minimum radius is limited by the Gibbs-Thompson effect to tens of nanometers) and the electron beam lithography (whose minimum radius is limited both by lithography and by sidewalls stability during the RIE process) need further oxidation processes to shrink the radius of the NWs. It is necessary to achieve crystalline cores of a few nanometers. Then, we described a new top-down approach followed in these last years to make Si NWs. This top down approach, i.e. metal assisted etching, is a chemical approach and is based on chemical oxidation of silicon through a metal catalyst and a subsequent removal of oxidized silicon through an HF bath. This method is simple, wafer scale, cheep and easy to apply. Making NWs by this method needs basically a silicon wafer and a bath of a

couple of minutes into a solution containing an oxidant, a metallic salt and some HF acid. It is unbelievably simple. By the way, lots of metallic dendrites form during the reaction have to be removed in some way from the region all over the MACetch Si NWs, by using etchants which can damage the surface of the NWs themselves. This technique offers the possibility to control the doping as preferred, since the doping of the initial silicon layer can be controlled via conventional implantation techniques before the etching. We have also shown how the radius of the nanowires obtained by metal assisted etching can be tuned up to minimal sizes of 10 nm via difficult lithography processes involving alumina masks and reactive ion etching. In the next chapter we will show that, through a maskless and cheap metal-assisted technique, it is possible to go easily beyond the 10 nm size limit.

Chapter 2

Synthesis and structure of group IV semiconductor NWs

Abstract

In this chapter will be shown that Metal-assisted chemical etching (MacEtch) is a powerful technique to obtain high density and low-cost Si NWs with high and controllable aspect ratio. NWs obtained by this technique have exactly the same structure and doping properties of the substrate and, depending on the adopted substrate, vertical or tilted NWs can be obtained. Then, it will be shown that by using for the first time ultra thin films of gold or silver as catalysts for the etch, their main size becomes less than 10 nm, allowing quantum confinement effects. A Si core - SiO_2 shell structure is obtained for and it is possible to tune the core of the NWs scaling it down to 5 nm. The size of the Si NWs scales down as the thickness of the metallic mesh (used as a catalyst for the etching process) becomes thicker. Both energy filtered TEM analyses and Raman analyses strictly confirm these data. Hence Si NWs made by MacEtch are suitable for photonic applications. Also, A more complex system has been realized, indeed by etching a multi quantum well made by stacks of 1 nm thick Ge and 54 nm thick Si it is possible to realize Si/Ge MQW NWs. In this way a

structure made of Si NWs and Ge disks can be obtained, in which carriers are confined in 2D and 3D respectively.

2.1   Synthesis of ultrathin Si NWs by metal assisted etching

The first part of this PhD thesis is dedicated to a novel approach for the realization of Si NWs suitable for photonics. Therefore, it's important and strategic that the developed method gives NWs with diameters comparable with quantum confinement effects. Metal-assisted wet etching processes are a known alternative method for Si NWs synthesis [68, 72] and have been identified as the most promising method to achieve these results. The metal catalyzes Si oxidation by H_2O_2 and then SiO_2, selectively formed where metal and Si are in contact, is etched by HF. In metal-assisted wet etching processes the metal catalyst is usually present in the etching solution as a salt (typically $AgNO_3$) [97]. Note also that NWs with a mean radius lower than 30 nm have been never obtained by etching processes assisted by metal salts [98] while NWs with dimensions of 10 nm have been obtained only using particular masks of anodized aluminum oxide [76]. Even in the case in which MACetch Si NWs emit light, the origin of their emission is somehow controversial. Moreover, the use of metal salts (e.g. $AgNO_3$) leads to the formation of dendrites, whose subsequent removal could damage the NWs [97, 98]. In this chapter we present a maskless, cheap, fast and compatible with Si-technology process for the direct synthesis of small Si NWs exhibiting room temperature light emission. The process is a modified metal-assisted wet etching, exploiting the replacement of the salt with an ultra thin metal thin film. A sketch of the adopted method is depicted in fig. 2.1. To this purpose, Si NWs have been obtained starting from p-type (B concentration of 10^{16} cm^{-3}) single crystal, (111)- and (100)-oriented Si wafers. The wafers were cut into 1 cm × 1 cm pieces, and then UV oxidized and dipped in 5% HF to obtain clean and oxide-free Si surfaces. Afterwards, a thin Au layer, having a thickness of 2 or 3 nm (corresponding
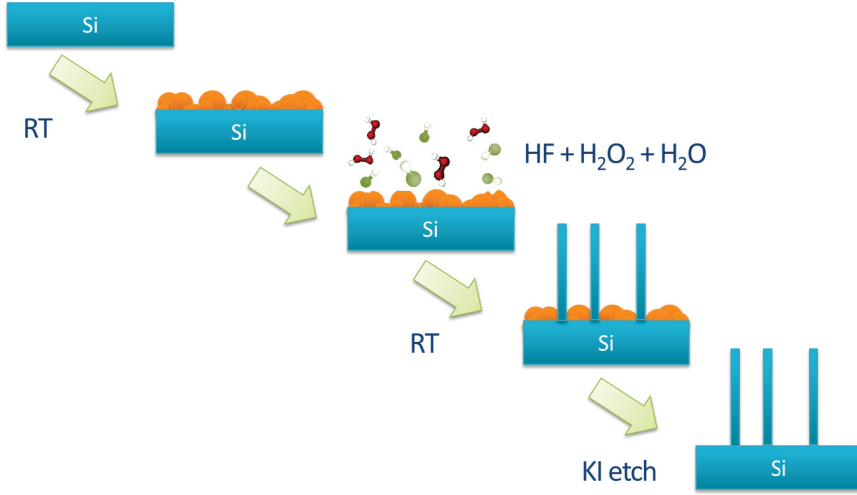
Figure 2.1: *Etching scheme of metal assisted chemical etching of Si NWs by using ultrathin layers of gold and silver as catalysts [60].*

to 1×10^{16} and 1.6×10^{16} Au $atoms/cm^2$, respectively), was deposited on the Si samples at room temperature by electron beam evaporation by using high purity (99.9%) gold pellets as a source. Alternatively, Ag layers 10 nm thick were deposited with the same procedure. The amount of deposited Au and Ag was verified by Rutherford Backscattering Spectrometry (RBS), as shown in fig. 2.2.a. This technique allows an accurate control of stoichiometry of thin films. We will see that an accurate control of the thickness of gold and silver is necessary for successfully control the radius of Si NWs. Finally, samples were etched at room temperature in an aqueous solution of HF (5 M) and H_2O_2 (0.44 M) to form Si NWs. During the etching, as highlighted in the previous chapter, holes are injected through the metal into the silicon, they oxidize silicon which finally is removed by HF and diffuses into the liquid phase. As a result, gold and silver meshes sink into the crystalline silicon, leaving Si NWs formed during the etching. These metals can be possibly removed via a bath in a solution containing potassium iodide KI and iodine I_2. The removal of gold has been demonstrated via RBS measurements, shown in fig. 2.2.b. These RBS measurements, despite RBS is a method typically used to study planar
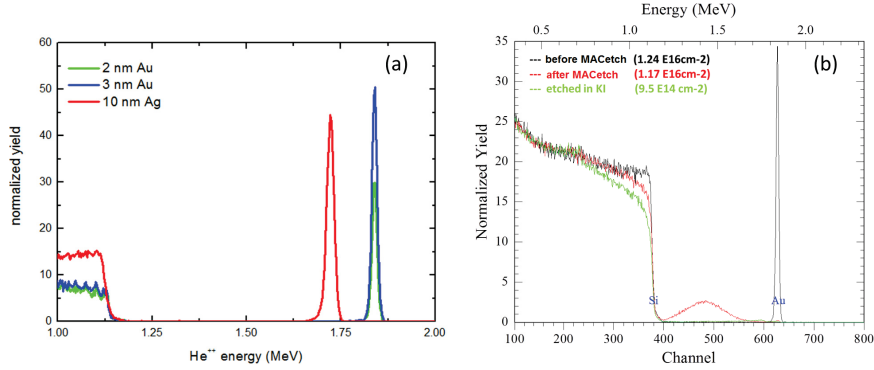
Figure 2.2: *(a) RBS spectra of ultrathin layers of gold and silver on Si substrates. (b) RBS spectra of a 2 nm thick gold layer before and after the MACetch and after the removal in a solution containing a mixture of KI and I_2.*

structures, give clear information about the sinking of gold into the NWs structure. All of the gold previously deposited on the surface drops into the silicon, leaving only a short tale of gold droplet from the edge of the etching into the NWs. Gold can be successfully removed leaving less than the 3% of its initial amount. This strategy presents two main relevant advantages: no metallic dendrites due to the etching process are present and, more importantly, a better control over the Si NWs structural properties is obtained. We have indeed been able to define a precise process window where Si NWs having a diameter compatible with the occurrence of quantum confinement phenomena can be obtained. This condition has been achieved by identifying a very narrow thickness range of the Au or Ag thin films for which the layer itself is not continuous, but it is characterized by a peculiar morphology, which leaves uncovered a relevant fraction of the Si surface. Within this thickness range, the morphology of the metal layer and the etching solution determine the formation of NWs having an extremely small diameter. In the inset to fig. 2.3 a plan view SEM image of a Si surface after 3 nm Au deposition is shown. Dark regions are uncovered Si, while yellowish regions represent Au. It is clear that several nanometric uncovered Si areas, almost circular and totally embedded within Au regions are present, these are indeed the precursor sites where
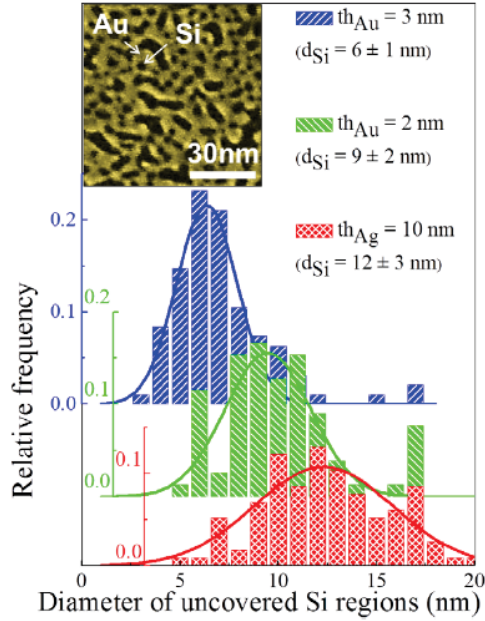
Figure 2.3: *The inset shows a plan view SEM image of a Si surface after 3 nm Au deposition. Dark areas are uncovered Si regions while yellowish areas are Au. A statistical analysis after 3 nm or 2 nm Au deposition and 10 nm Ag deposition of the diameter distribution of the circular uncovered Si regions after analyzing several SEM images is reported in figure [60].*

NWs will form upon etching. Similar structures are also observed after Ag deposition though in this case Ag, as a result of a smaller wettability, tends to ball up and therefore interconnected structures leaving nanometer-size uncovered Si regions are obtained for much thicker metal layers. Figure 2.3 presents a statistical analysis of the precursor sites on the basis of several SEM images taken after 10 nm Ag and 2 or 3 nm Au deposition. In all cases a nanometer size distribution of uncovered Si regions is obtained measuring the diameter of the circle circumscribed to each precursor site, with smaller sites achieved for Au with respect to Ag and by increasing the amount of deposited Au. Figure 2.4.a reports a cross section SEM image of Si NWs obtained after the wet etching of the 2 nm Au covered (100)-oriented Si substrate. This cross section image displays a dense and uniform distribution of NWs, having the same
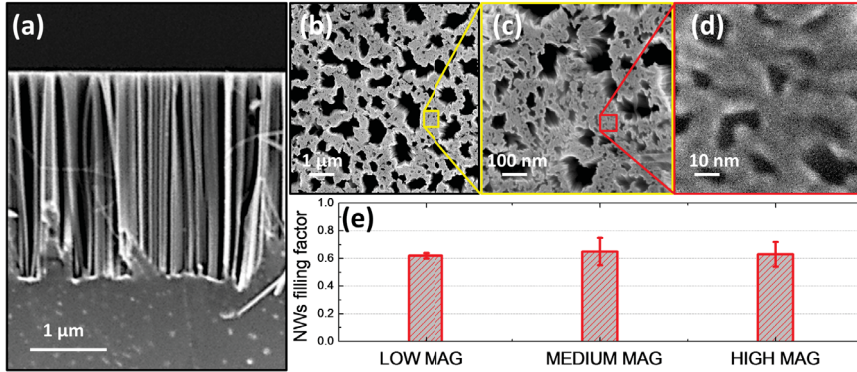
Figure 2.4: *(a) Cross section SEM image of Si NWs obtained by metal assisted chemical etching technique. (b,c,d) Top view SEM image of MACetch Si NWs at three different magnitudes: 25k×, 250 k× and 2500 k× respectively from left to right. These images look the same despite of the different magnification, hence this structure is a fractal. (e) Histogram of the percentage of area covered by Si NWs (NWs filling factor) at these three magnifications. The constant filling factor is a proof of the fractality of this system* [99].

length (about 2.6 μm, as determined by the etching conditions) and very small diameters. Figures 2.4.b,c,d show different top view SEM images of MACetch Si NWs at three different magnitudes: 25 $k\times$, 250 $k\times$ and 2500 $k\times$ respectively increasing the magnitude each time by an order of magnitude from left to right. It's clearly visible that, despite these microscopy images are made at different magnifications, they look similar one to another. The same structure is repeated at different length-scales. This aspect is a signature of a fractal structure, since a sort of "scale invariance" is visible [99]. Fractalness and randomness are sometimes connected, as in this case. In fact, the metallic mesh is random and also there is a sort of redistribution of metallic catalysts during the etching process [61]. Particularly remarkable are the extremely high NW density $(1 \times 10^{11}~cm^{-2})$ as deduced by the analysis of plan view SEM images, in which about the 60% of the total surface is covered by nanowires. The density value is similar to the density of the precursor sites shown in the inset of fig. 2.3, well above the typical values found in Si NWs grown by techniques based on the VLS
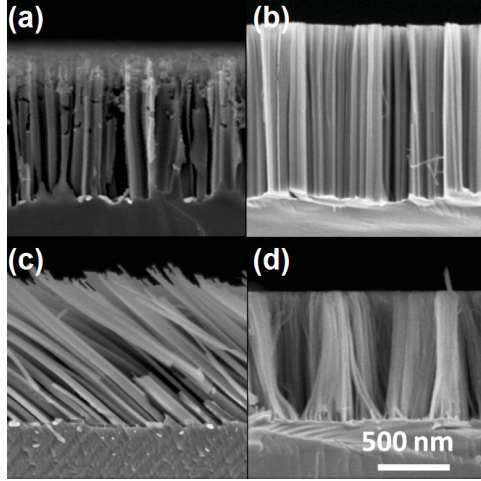
Figure 2.5: *Cross section SEM images of MACetch Si NWs obtained by etching a (100)-oriented Si substrate covered by 10 nm of Ag (a), a (100)-oriented Si substrate covered by 2 nm of Au (b), a (111)-oriented Si substrate covered by 10 nm of Ag (c) and a (111)-oriented Si substrate covered by 2 nm of Au.*

mechanism [16, 26, 25]. As reported in literature, depending on the nature of the catalyst adopted and depending on the substrate, it is possible to obtain NWs with different structural properties. As an example, fig. 2.5.a and fig. 2.5.b show NWs obtained by etching a (100)-oriented Si substrate covered by 10 nm of Ag and 2 nm of Au respectively. At the same time, fig. 2.5.c and fig. 2.5.d show NWs obtained by etching a (111)-oriented Si substrate covered by 10 nm of Ag and 2 nm of Au respectively. Obviously, the etching rate changes depending on the orientation of the substrate, doping and on the amount and kind of the metallic mesh. In fact, once defined the etching rate $R_{etching}$ as the number of atoms of Si etched by each atom of metal per second:

$$R_{etching} = \frac{velocity_{etching}}{thickness_{met}} \frac{\rho_{Si}}{\rho_{met}} \qquad (2.1)$$

It has been observed that the etch rate of silver is 1.4 s^{-1} while the etch rate of gold is 2.8 s^{-1}. Au is two times more efficient than Ag. This difference can be attributed to the different electronegativity

65

and oxidation number of Au and Ag. Moreover, Au always etches normal to the surface, since it has a higher etching rate than Ag. Indeed, Ag can etch according to the crystallographic orientation, since it has a slower etch rate. Moreover, the NWs made using Ag catalysts seem to be thicker than the Au-catalyzed counterparts. Since the preferred direction of etching is the [100], and since the Au-catalyzed MACetch Si NWs are thin, with a very high aspect ratio, in (111) substrates the formation of bundles of NWs can occur. The formation of bundles can be attributed to surface tension forces exerted on the nanowires during the drying of the sample, which is a common phenomenon for drying of long nanowire arrays from the solvent and can be avoided with super-critical CO_2 drying [61, 100].

2.2   Structural Features of NWs

Both Si NWs and MQW Si/Ge NWs have been prepared by metal assisted etching technique. Different characterizations have been made on these systems, i.e. SEM and TEM characterizations in order to study both the length and the structural and surface properties of the NWs, Raman analyses to know the main diameter of the NWs, and Energy Dispersive X-ray spectroscopy which allows to obtain the mean amount of oxygen in the NWs media and hence estimate the amount of silicon oxide which wraps the silicon core. RBS measurements have also been performed for a fine control of the gold and silver thickness, which is a key parameter of the etching. A similar analysis have been performed on MQW Si/Ge NWs. The knowledge of the structural properties of both of these systems allows to control them during the synthesis and hence their optical and electrical properties.

2.2.1   Structural Properties of Si NWs

Tuning the length of Si NWs is very easy. Typically, at room temperature, the etching rate of (100)-oriented Si covered by 2 nm of gold in a solution of 0.44 M H_2O_2 and 5 M HF is about 400 nm/minute. Silicon NWs of different lengths are shown in fig. 2.6.

Figure 2.6: *Cross section SEM images of Si NWs prepared by etching a (100)-oriented Si substrate covered by 2 nm of gold at different etching times. The length of the NWs are 1, 2, 3, 4, 5 μm respectively from left to right.*

These NWs have lengths from 1 to 5 μm, which can be tuned linearly by varying the etching time approximately from two to ten minutes. The diameter of the NWs is the same above all the length of the NWs, since the etching proceeds vertically. Then, it is possible to obtain NWs with very high and controllable aspect ratios. Raman measurements have been used to estimate the different NWs size obtained by varying the thickness of the metal layer assisting the etching process. In particular, fig. 2.7 reports the Raman spectra of Si NWs synthesized by using Ag (10 nm thick) or Au (2 and 3 nm thick) metal layers; they are characterized by asymmetrically broadened peaks, red shifted with respect to the symmetric and sharper peak typical of bulk crystalline Si (shown in the same figure for comparison purposes), which is found at 520 cm^{-1}; the position and the shape are in agreement with literature data concerning quantum confined crystalline Si nanostructures. The Raman peaks have been fitted by using a phenomenological model developed by Richter et al. [101] to deduce the nanocrystal size from the Raman spectrum, subsequently improved by Campbell and Fauchet [102] for strongly confined phonons and more recently applied by Piscanec et al. to Si NWs [103]. The fit procedure gives NW diameter values of 9± 2 nm for the 10 nm Ag film, 7 ± 2 nm for the 2 nm thick Au film and 5 ± 1 nm for the 3 nm thick Au film. We under-
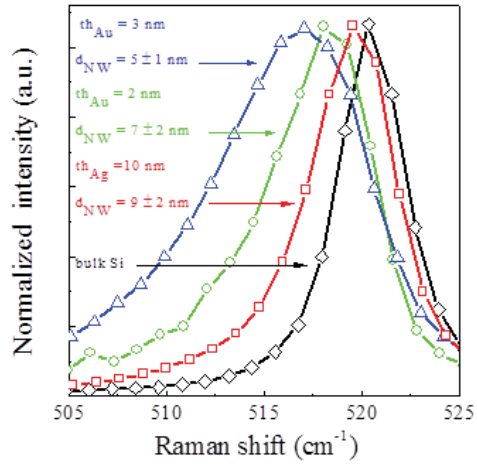
Figure 2.7: *Raman spectra of Si NWs obtained by using Au layers having a thickness of 3 nm (blue line-triangles) and 2 nm (green line-circles) and Ag layer having 10 nm (red line-squares). For comparison, the Raman spectrum of bulk crystalline Si (black line-rhombs) is also shown. A fit to the Raman data gives NW diameter values of 5 ± 1 nm for the 3 nm thick Au film, 7 ± 2 nm for the 2 nm thick Au film and 9 ± 2 nm for the 10 nm Ag film [60].*
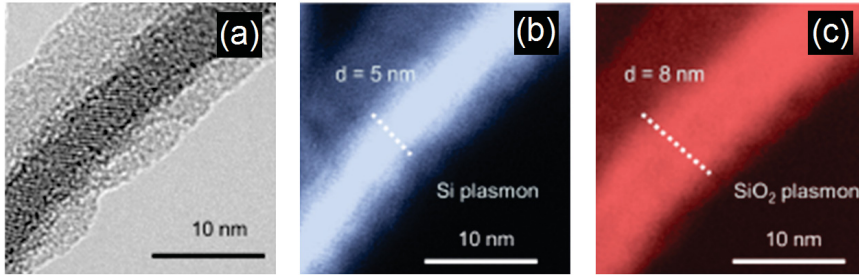
Figure 2.8: *(a) High resolution bright field TEM image performed on a single NW. (b) EFTEM image from the same NW obtained by selecting electrons which have lost an energy of 16 eV, corresponding to the Si plasmon loss. (c) EFTEM image obtained by selecting electrons which have lost an energy of 24 eV, corresponding to the SiO_2 plasmon loss.*

line here that the very large aspect ratio of these NWs can be very hardly obtained by techniques based on the VLS mechanism. It is also remarkable that the measured NW sizes are in good agreement with the sizes of the precursor sites shown in fig. 2.3. This is an evidence that this synthesis represents a maskless method taking advantage of the thickness-dependent roughness of the metal thin film and that the deposited pattern is directly reproduced after etching. It is noteworthy that, as a direct consequence of the peculiar characteristics of the synthesis process, based on the anisotropic etching of commercial Si substrates, NWs are monocrystalline and defect free, as verified by TEM measurements. Figure 2.8.a reports a high resolution TEM image of a typical Si NW obtained by using a 2 nm thick Au film. Two features are highly remarkable:

(i) a core-shell structure is clearly visible. Noticeably, Si lattice planes are visible only in the inner part of the NW, while the shell seems to be amorphous;

(ii) The diameter of the crystalline core is about 5 nm, in agreement with the mean size of 7 ± 2 nm estimated by Raman measurements.

Further structural details can be obtained by the analysis of the energy filtered (EFTEM) image shown in fig. 2.8.b and fig. 2.8.c. The EFTEM image shown in fig. 2.8.b has been obtained by selecting electrons which have lost an energy of 16 eV, corresponding to the Si plasmon loss. The size of the very bright Si region fully
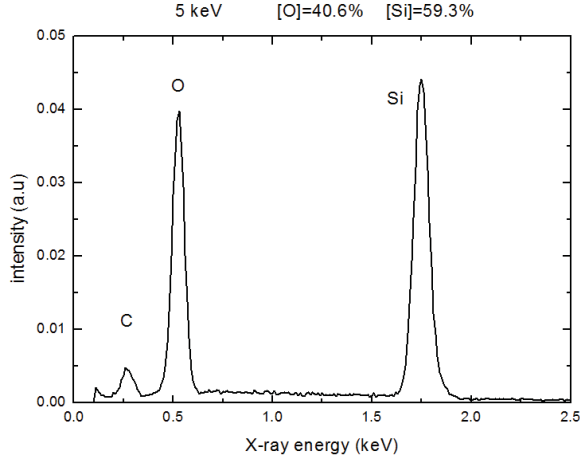
Figure 2.9: *Energy Dispersive X-ray spectroscopy spectra of Si NWs. A considerable oxidation of Si NWs is observed.*

corresponds to the crystalline region visible in fig. 2.8.a, unambiguously demonstrating the presence of a crystalline Si core of about 5 nm. On the other hand, the shell appears much less bright than the core, suggesting a different chemical composition. A proof of the shell composition has been obtained by collecting a EFTEM image obtained by selecting electrons which have lost an energy of 24 eV, corresponding to the SiO_2 plasmon loss, shown in fig. 2.8.c. Such an image indeed suggests that the shell is essentially composed by SiO_2 with a diameter of 8 nm, formed due to the air exposure of the NW. Different information is given by the EDX analysis made on a large area of Si NWs. This analysis is shown in fig. 2.9. It has been performed by irradiating a large area (several micron squares) of Si NWs with electrons with an energy of 5 keV, whose mean free path in bulk Si is 300 nm. Considering that the percentage of the filled area of Si NWs is about 0.6, about half of the volume is occupied by air, then the mean free path of electrons in Si NWs should double and become roughly 600 nm. Hence it is possible to collect information on higher part of the NWs, since this analysis has been performed on NWs with a length of 2.6 μm. It has been measured that the atomic percentage of Si is about 60% while the atomic percent of oxygen is 40%. Some carbon contamination is observable, and comes from the environment since Si

NWs have a large exposed area and carbon structures easily stick on them. These are atomic percentages and have to be compared with the results from the TEM analysis, which gives a volumetric ratio $V_{Si}/V_{SiO_2} = \frac{\pi(2.5)^3}{\pi(4^5-2.5^3)} = 0.64$. Considering that part of the Si is bonded with oxygen atoms to form silicon dioxide, the atomic ratio measured by EDX is $X_{Si}/X_{SiO_2} \approx 2$ and since silicon dioxide has a lower density than silicon, EDX gives the value $V_{Si}/V_{SiO_2} = 1.38$. This value is about two times higher than the one measured by TEM on a single NW. Since there is a broad distribution of diameters of the NWs and since native oxide on the surface of the NWs is expected to be independent of the radius, it is possible that the value given by EDX analysis has been influenced by thicker NWs, in which the percentage of Si is higher.

2.2.2 Structural properties of Si/Ge MQW NWs

A similar approach has been adopted for the realization of Si/Ge MQW NWs. The substrate adopted has been prepared by Molecular Beam Epitaxy (MBE) in the following way: first, a buffer layer of 54 nm has been deposited on the cleaned and reconstructed surface of a (100)-oriented Si wafer (p-type, 10^{16} cm^{-3}). Then, layers of 1 nm thick Ge and 54 nm thick Si are alternatively evaporated at 0.1 Å/s and 3 Å/s respectively, for 62 times. This structure has a thickness of about 3500 nm, and has been grown at a temperature of 450°C. With these growth parameters the grown structure should be heteroepitaxial, which is a necessary condition to have a constant and well defined etching direction when the gold droplets sink across the Si/Ge/Si interfaces. The MACetch Si NWs preparation is similar to the process adopted for Si NWs, and is sketched in fig.2.10. First, the MBE grown substrate is cleaned and the silicon dioxide which forms on it is removed via HF bath, then it is put into an evaporator chamber where a 2 nm thick gold layer is evaporated. The cleaning process before the gold evaporation is a crucial step of the etching process. In fact without this process gold cannot inject holes into silicon and neither oxidation nor etching can occur. After the deposition of a 2 nm thick gold layer, the sample is immersed in the etching solution which has a molarity of H_2O_2 of 0.44 M and a
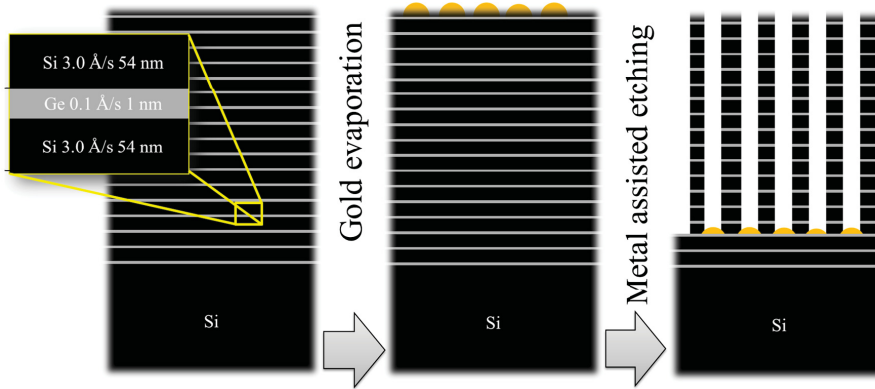
Figure 2.10: *Scheme of the fabrication of a multiquantumwell (MQW) of alternating 1 nm-thick Ge layers and 54 nm-thick Si layers. This substrate has been then chemically etched by using ultrathin layers of gold as catalyst in order to obtain Si/ MQW NWs.*

molarity of HF equal to 5 M. Hence, the obtained structure of each Si/Ge MQW NW consists in 55 nm long whiskers alternated by 1 nm thick Ge disks. It will be shown in the following chapter that light can arise from these novel kind of structures. In fact, since the electron-hole excitonic pair in monocrystalline germanium has a mean radius of of 25 nm, a structure made by 1 nm thick disks of Ge allows at least a strong 1D confinement of carriers giving rise to a superposition of electrons and holes wavefunctions and therefore it changes their electronic and optical properties. Figure 2.11.a-b-c-d show Si/Ge MQW NWs grown by this maskless approach at different etching times. Their length goes from 1 to 3 μm, and the length goes linearly with the etching time. Most of the area of the sample have been successfully etched, except few areas in which NWs formation doesn't occur. The etch rate of this kind of structure is similar to the etch rate for MBE grown Si and is equal to 150 nm/min. This etch rate is lower than the etch rate of CZ Si, and this could be attributed to a lower oxygen contamination or to different doping. It is noteworthy to say that, to the best of my knowledge, Ge NWs have not been ever made by metal assisted etching. The etch solution applied for Si/Ge MQW Si NWs works only for thin Ge layers embedded in thick Si layers. In fact, this

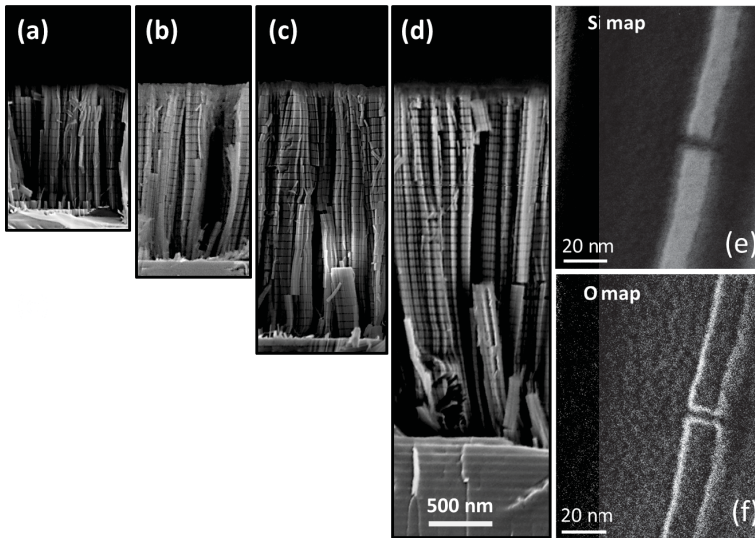Figure 2.11: *(a-b-c-d) Cross section SEM images of MQW Si/Ge NWs of 1, 1.3, 2, 3 μm respectively from left to right. (e) EFTEM image from a single Si/Ge NW obtained by selecting electrons which have lost an energy of 16 eV, corresponding to the Si plasmon loss. (f) EFTEM image from a single Si/Ge NW obtained by selecting electrons which have lost an energy of 24 eV, corresponding to the SiO_2 plasmon loss.*
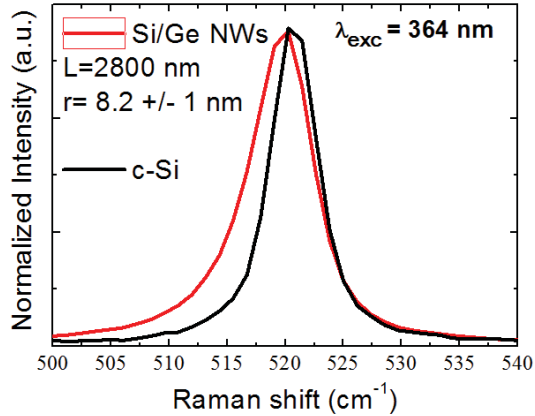
Figure 2.12: *Raman spectra of Si/Ge MQW NWs obtained by using 2 nm thick Au layers (red line). The Raman spectrum of bulk crystalline Si (black line) is shown for comparison. A fit to the Raman spectrum gives a Si/Ge MQW NW diameter value of 8.2 ± 1 nm.*

etching solution is water based, and it is well known that germanium typically is oxidized in water and quickly dissolved.

Figures 2.11.e-f show TEM images of a freestanding Si/Ge NW obtained by filtering the electron energy loss at the Si and O plasmonic resonances respectively. The 54 nm Si/ 1 nm Ge/ 54 nm Si structure can be observed. The diameter of the Si NW is about 10 nm (see fig. 2.11.e), as well as the diameter of the Ge dot, due to the etching process. Then, it is probable that the diameter of the Ge dot is less than the diameter of the Si NW, because of a partial dissolution of Ge in the water based etching solution. Moreover, the energy filtered TEM image in fig. 2.11.f shows the presence of a SiO_2 shell all around the Si NW and at the interface between the Si NW and the Ge dot. Hence, the thickness of the Ge could be less than 1 nm, enhancing quantum confinement effects of the carriers localized inside it. The diameter of the Si/Ge MQW NWs has been confirmed by an accurate Raman analysis on the samples, similarly to the one adopted for Si NWs. The Raman spectra of Si/Ge MQW NWs synthesized by using 2 nm of Au are shown in fig. 2.12.

The Raman spectrum of Si/Ge MQW NWs (red line) is charac-

terized by an asymmetrically broadened peak, red shifted with respect to the symmetric and sharper peak typical of bulk crystalline Si (black line), which is found at 520 cm^{-1}. The position and the shape is in agreement with literature data on quantum confined crystalline Si nanostructures. The Raman spectrum of Si/Ge MQW NWs has been fitted by the same model used for Si NWs [101, 102, 103], and the fit procedure gives a value of the diameter equal to 8.2 ± 1 nm, in agreement with TEM measurements. At the same time, no Raman emission coming from Ge has been detected, because of its low concentration in the Si/Ge MQW NWs sample.

Conclusions

In this chapter we have shown that Metal-assisted chemical etching, together with the advantage of using ultrathin films of gold and silver, is a powerful technique to obtain NWs with features compatible with quantum confinement effects. A study of the different mesh structure of 2 nm thick and 3 nm thick gold, and of 10 nm thick silver has been conducted. It has been demonstrated that the accurate control of the metal thickness in this few nm range is strategic for control of the radius of the NWs. The mean size of the holes in the metallic mesh will determine the mean size of the radius of the NWs. Indeed, it has been possible to achieve diameter sizes as 9 nm, 7 nm and 5 nm. The crystallinity of the Si core and the presence of a SiO_2 shell has been demonstrated by TEM analyses, by using high magnification analyses and by filtering the electron energy loss at the Si and O plasmonic resonances. Finally, a more complex system has been realized, etching a multi quantum well made by stacks of 1 nm thick Ge and 54 nm thick Si. Si/Ge MQW NWs can be fabricated with the same etching process used for Si NWs. The complex alternating structure of Si/Ge/Si quantum wells for both electron and holes is repeated along each NW several times. The obtained structure is therefore made of Si NWs alternated to Ge disks. These NWs have a diameter of less than 10 nm, as measured by the shift in the Raman spectra, and confirmed by TEM analyses. It will be shown in the next chapter that both the small diameter of Si NWs, and the 3D confined structure of Ge

disks will have a strong impact on the luminescence properties of both Si NWs and Si/Ge MQW NWs, due to quantum confinement of carriers.

Chapter 3

Optical properties of group IV semiconductor NWs

Abstract

The development of functional materials for light emission and/or amplification is a research field in constant expansion. In particular, semiconductor nanowires (NWs) represent a promising system that have attracted a considerable interest within the scientific community as an innovative material for applications in light sources sensing and nanoscale photovoltaic devices. In this chapter the optical properties of both Si NWs and Si/Ge multi quantum well (MQW) NWs will be studied. Concerning both Si NWs and Si/Ge MQW NWs, an efficient red room temperature luminescence, visible at the naked eye, is observed when NWs are optically excited, exhibiting a blue-shift with decreasing NW size in agreement with quantum confinement effects. A prototype device based on Si NWs has been fabricated showing a strong and stable electroluminescence at low voltages. The detailed analysis of the steady-state and time-resolved PL properties of Si NWs as a function of aging, temperature and pump power allows to suggest that the emission is due to the radiative recombination of quantum confined excitons. Moreover, Si/Ge MQW NWs exhibit also a IR photoluminescence

at low temperature, centered at 1300 nm. A detailed time resolved study allows to demonstrate that this emission is due to radiative recombination of excitons confined in the large amount of Ge disks present in each NW. At the same time, Si NWs are known to exhibit a strong Raman activity, depending on the morphology and the array arrangement. Here we report on the unique optical properties exhibited by a forest of densely arranged MACetch SiNWs with a 2D fractal geometry. The texture of this new material is responsible for a very high light trapping, Anderson localization and recurrent multiple coherent scattering events that lead towards the experimental evidences of a strong stimulated enhanced backscattering cone of the Raman signal of Si NWs, paving the way towards Raman lasing phenomena. The relevance and the perspectives of the reported results open the route toward novel photonics applications of group IV semiconductor NWs.

3.1 Quantum confinement in Si based nanostructures

Silicon is by far the most suitable material for microelectronics. Indeed, it is an abundant element and it has very good electrical, thermal and mechanical stability. Moreover, its oxide (SiO_2) is a very good insulator, which can well passivate surfaces and acts as an effective diffusion barrier. All of these properties made silicon the leading material in microelectronic applications. Anyway, silicon can do well even in photonics. Indeed its high refractive index (n = 3.5) makes it a good medium through which light can be guided and transmitted. Indeed, several low loss waveguides based on silicon have been developed, using different approaches. Moreover, silicon based detectors have been realized, able to convert a light signal into an electrical signal [104]. What silicon is still lacking, is an efficient light emitter or even a laser. For a long time, silicon has been considered unsuitable for optical application, due to the indirect nature of its electronic bandgap. Indeed, once an electron-hole pair is created inside bulk silicon, the radiative recombination pro-
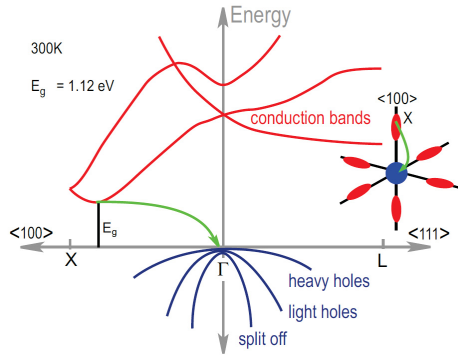
Figure 3.1: *Silicon electronic bands. Green arrow shows the indirect transition from the bottom of the conduction band to the top of the valence band.*

ducing a 1.1 eV photon necessitates of a phonon in order to conserve crystal momentum. Silicon electronic bands are shown in fig. 3.1. Hence the emission of a photon is a three-particles process (electron, hole and phonon) and is characterized by very small rates, bringing to lifetimes of the order of ∼1 ms. This lifetime is too long if compared to the recombination times of the order of μs or even ns characterizing some non-radiative transitions, such as the Shockley-Hall-Read (SHR) recombination by deep levels introduced in the gap of silicon by defects and metallic impurities [105, 106], or Auger recombination with the promotion of a free carrier (electron or hole) in higher lying levels within the conduction or valence band respectively. All of these processes, being orders of magnitude more probable than radiative recombination, make photon emission from silicon a very weak process, characterized by quantum efficiencies of the order of $10^{-7} - 10^{-6}$, four orders of magnitude smaller than for direct bandgap semiconductors. In order to solve this problem, many routes have been followed. Among these, silicon based nanostructures and defect engineering of silicon through insertion of efficient light emitters in the crystal have shown great potentialities. Once a semiconductor structure is reduced to nanometric sizes (1-10 nm), the electron and the hole become spatially confined, and cannot be described anymore by planar wavefunctions, but as a superposition of them their wavefunctions becoming wave-

packets. Moreover, due to the boundary conditions, only certain wavefunctions with precise wavelengths can be supported by the material. Therefore the energy of the confined particles becomes quantized. In addition, since the position of the particles can be defined with more determination with respect to the bulk, as a result of the Heisenberg's uncertainty principle, the momentum of the particles suffers a greater indetermination. This results in an increase in the minimum energy level available to the particles. Indeed, in nanostructured silicon, both the electron and the hole are characterized by higher energies, thus producing an increase of the energy gap with respect to bulk silicon. From a theoretical point of view, the actual energy gap of a Si nanowire depends on the method used, and on many corrective factors, such as the electrostatic energy interaction between electron and hole forming the exciton ($\sim 1/L$), the exchange interaction ($\sim 1/L^3$) among them, the spin-orbit interaction. Another effect of quantum confinement is the increase in the probability associated with an optical transition. Indeed, due to the reduced size, the translational symmetry of the system is no more satisfied and, as a consequence, the crystal momentum is no more a good quantum number. This allows for vertical, direct band to band, no-phonon transition to become more probable [107]. The total radiative probability per unit time can be expressed as the product of the oscillator strength times the density of states involved in the transition. It has been shown that the oscillator strength exponentially increases as the number of silicon atoms in the nanocrystal decreases [108], thus leading to an increase of the total radiative recombination probability. Moreover, going from three-dimensional to zero-dimensional (quantum dots) systems, the density of states tends to resemble the Dirac's delta function, producing again an increase in the probability of a photon to be emitted in a exciton recombination process.

The first experimental results more than a decade ago demonstrating room-temperature luminescence of silicon nanocrystals (Si-NCs) in silicon implanted SiO_2 [109] or in porous silicon [93, 110] attracted a strong interest among the scientific community. For clarifying the origin of the observed luminescence signal as well as for the described potential applications, tight control over the size of the nanocrystals is essential. Synthesis of Si-NCs can be realized by
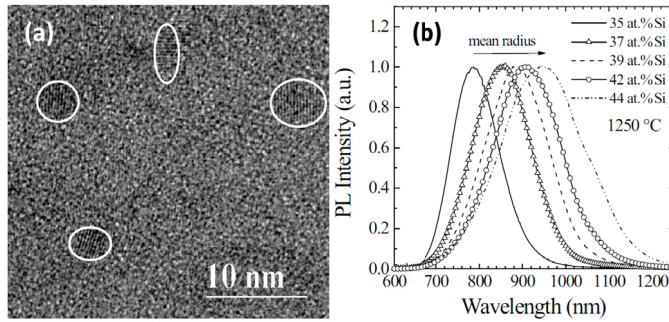
Figure 3.2: *(a) High resolution TEM of a SiO_x sample after high temperature annealing. Si NCs are clearly shown. (b) Normalized PL spectra of SiO_x thin films with different silicon concentrations annealed at 1250 °C for 1 hour. Spectra are measured at room temperature.*

ion implantation of silicon into an SiO_2 matrix [111], by deposition of sub-stoichiometric oxide films using chemical vapor deposition (CVD) [112] or by sputtering processes [113], in all cases followed by thermally induced precipitation and Ostwald ripening of silicon clusters. All these methods result in a relatively broad size distribution of the synthesized Si-NCs. Size control in these systems is normally realized by shrinking the entire size distribution by varying the silicon content within the SiO_2 matrix or by subsequent oxidation of the nanocrystals [114]. The origin of the room temperature photoluminescence (PL) signal from Si-NCs is still under discussion, and some essential features of this PL signal are still not understood in detail. Several mechanisms have been suggested to explain the appearance of this luminescence signal, such as defects within the SiO_2 [115], or at the nanocrystal surface [116], the formation of siloxene [82], or quantum confinement effects of the excitons caused by their spatial confinement within the Si NCs [107, 110]. As an example, fig. 3.2.a shows a high resolution TEM image performed on a SiO_x sample containing an excess of Si, i.e. 42 at. % Si annealed at 1250 °C for 1 hour [117]. The formation of crystalline Si precipitates having nanometric dimensions is clearly evident. The Si nanocrystals formation is thought of in terms of a first nucleation of small Si clusters inside the matrix, followed by an Ostwald ripening process which determines the growth of

81

larger nanocrystals at the expenses of smaller ones. According to this model, at a fixed annealing time and temperature, the mean nanocrystal radius depends only on the total amount of Si in excess in the SiO_x matrix. All of the produced Si nanocrystals emit light at room temperature in the range 700 -1100 nm. As an example in 3.2.b the normalized PL spectra of Si nanocrystals obtained by annealing at 1250 °C SiO_x samples having different Si contents are reported [117]. The luminescence signal clearly shows a marked blue shift with decreasing Si content as a result of the smaller size of the Si nanocrystals. Indeed, the average nanocrystals radius (as observed by TEM) increases from 1.1 to 2.1 nm by increasing the Si content from 37 at.% to 44 at.% Si [117].

Another confined silicon system is porous silicon (PSi). Porous silicon was discovered by Uhlir in 1956 when performing electro-chemical etching of silicon. At the time, the findings were not taken further and were only mentioned in Bell Lab's technical notes [118]. In 1990, Canham showed that certain PSi materials can have large photoluminescence (PL) efficiency at room temperature in the visible: a surprising result, since the PL efficiency of bulk silicon (Si) is very low, due to its indirect energy band gap and short non-radiative lifetime [93]. The reason of this was the partial dissolution of silicon, which causes the formation of small silicon nanocrystals in the PSi material; the reduction of the effective refractive index of PSi with respect to silicon, and hence an increased light extraction efficiency from PSi; and the spatial confinement of the excited carriers in small silicon regions where non-radiative recombination centers are mostly absent. In general, PSi is a interconnected network of air holes (pores) in Si. PSi is classified according to the pore diameter, which can vary from a few nanometers to a few microns depending on the formation parameters (see fig. 3.3). PSi is mostly fabricated by electrochemical anodization (often referred to as electrochemical etching) of bulk Si wafers in diluted aqueous or ethanoic hydrofluoric acid (HF). Ethanol is often added to facilitate evacuation of H bubbles, which develop during the process. To form PSi, the current at the Si side of the Si/electrolyte interface must be carried by holes, injected from the bulk towards the interface. In order to achieve significant hole current in n-type Si, external illumination of the sample is required, depending on the doping
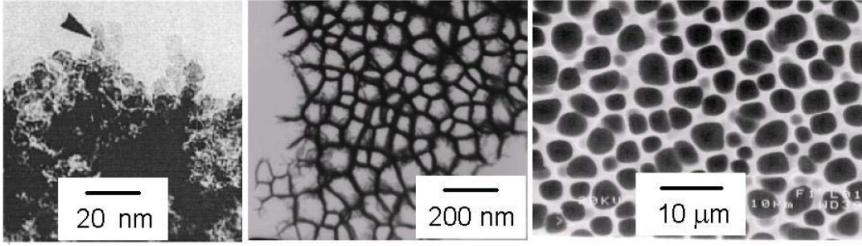
Figure 3.3: *Examples of PSi structures: microporous (left), mesoporous (center) and macroporous (right).*
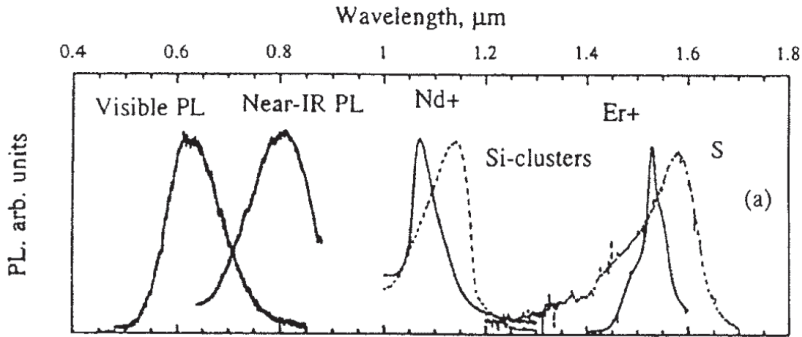
Figure 3.4: *Room temperature photoluminescence spectra for various PSi structures which have been oxidized or implanted with some selected impurities.*

level. A hypothesized chemical reaction which could describe the anodization is:

$$Si + 6HF \rightarrow H_2SiF_6 + H_2 + 2H^+ + 2e^-$$
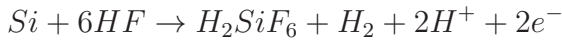
The last term (a negative charge at the interface, to be neutralized by the current flow) would explain the need of hole injection from the substrate towards the Si/electrolyte interface. Similarly to most semiconductor junctions, at the Si/electrolyte interface a depletion zone is formed, and the width of this depletion zone depends on the doping. Microporous PSi structures have been reported to luminesce efficiently in the near infrared (IR) (0.8 eV), in the whole visible range and in the near ultraviolet (UV) (see fig. 3.4).

Such a broad range of emission energies arises from a number of
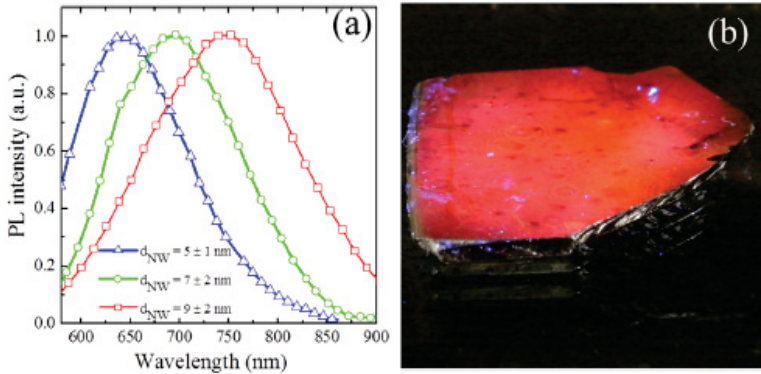
Figure 3.5: *(a) PL spectra obtained by exciting Si NW samples having different sizes with the 488 line of an Ar^+ laser at a pump power of 10 mW. (b) Photograph of a Si NW sample having an area of about 1 cm^2 excited by the 364 nm line of a fully defocused Ar^+ laser beam showing a bright red PL emission clearly visible by the naked eye.*

clearly distinct luminescent bands. In addition, PSi has been used as an active host for rare earth impurities, e.g. Nd or Er, or dye solutions. Direct energy transfer between PS and the impurity or dye is demonstrated.

3.2 A size-dependent photoluminescence in Si NWs

Si NWs synthesized by metal-assisted etching using thin layers of gold or silver are efficient light emitters at room temperature. Indeed, some reports about photoluminescence (PL) emission from Si NWs already exist in the literature but they are clearly not related to quantum confinement phenomena since NWs are too large and they exploit the presence of light emitting N-containing complexes [119] or the phonon-assisted low temperature recombination of photogenerated carriers [120], while only very few studies on room temperature PL from NWs whose size is reduced by poorly controllable oxidation processes have been reported [46, 19, 121]. The situation is very different in the present case. In fact, fig. 3.5.a reports typi-

cal PL spectra obtained by exciting with the 488 nm line of an Ar laser at a pump power of 10 mW Si NW samples having different sizes. The spectra consist of a broad band (full width at half maximum of about 150 nm) with the wavelength corresponding to the maximum of the PL emission exhibiting a shift as a function of the NW mean size. In particular, the PL peak is centered at about 750 nm for NWs having a mean diameter of 9 nm while it is clearly blueshifted at about 690 nm for NWs having a mean diameter of 7 nm and further shifted at 640 nm for a size of 5 nm. This behavior strongly suggests that quantum confinement effects are responsible for the observed light emission. Indeed emission is very bright and visible with the naked eye. Figure 3.5.b displays a photograph of the PL emission coming from a Si NW sample excited by the 364 nm line of a fully defocused Ar laser beam. The external quantum efficiency of the system has been measured to be higher than 0.5%, by taking into account the spatial emission profile of the Si NWs and under the conservative assumption that the exciting laser beam is totally absorbed by the material. Further details of the external quantum efficiency will be shown in the paragraph 3.2.3. This value is comparable with efficiencies reported for porous Si [95] and Si nanocrystals [122].

3.2.1 Excitation and de-excitation properties

Relevant information about the optical properties of Si NWs can be obtained by measuring the risetime of the PL signal as a function of the pump power, at room temperature. PL intensity I is generally given by:

$$I \propto \frac{N^*}{\tau_R} \tag{3.1}$$

being N^* the concentration of excited centers and τ_R the radiative lifetime. The rate equation for NWs will be:

$$\frac{dN^*}{dt} = \sigma\phi(N - N*) - \frac{N^*}{\tau} \tag{3.2}$$

being σ the excitation cross section, ϕ the photon flux, N the total

concentration of optically active NWs and τ the decay time, taking into account both radiative and non-radiative processes. If a pumping laser pulse is turned on at $t = 0$, the PL intensity, according to the previous equations, will increase with the following law:

$$I(t) = I_0(1 - e^{-t/\tau_{on}}) \tag{3.3}$$

with I_0 being the steady state PL intensity and τ_{on} the characteristic risetime. Indeed these measurements allow to calculate the excitation cross section of the system, in a fashion previously shown for Si NCs [123]. In fact, the risetime is given by:

$$\frac{1}{\tau_{on}} = \sigma\tau + \frac{1}{\tau} \tag{3.4}$$

σ being the excitation cross section, ϕ the pumping photon flux and τ the lifetime. Figure 3.6.a shows the PL risetime curves for different pump power. Each curve has been fitted with the following curve, slightly different from eq.3.3:

$$I(t) = I_0(1 - e^{-(t/\tau_{on})^\beta}) \tag{3.5}$$

where the parameter β is the same for all the curves, and takes into account the energy transfer from thinner NWs to thicker ones during the de-excitation process, which is intrinsically involved in this measure. By plotting the reciprocal of the risetime values at a wavelength of 690 nm as a function of the photon flux (see fig. 3.6.b) and by a linear fit of the data (see eq. 3.4) we obtain a value for the excitation cross section of about $5 \times 10^{-17} \ cm^2$. Note that very similar values have been previously reported for Si NCs [123, 124]; this fact constitutes a further evidence of the occurrence of quantum confinement effects in Si NWs. The PL properties of the system have been also analyzed as a function of the pump power in the 0.5–50 mW range. In this higher pump power range, the PL intensity increases almost linearly by increasing the pump power, while no noticeable variation of the lifetime with increasing power is detected. This behavior suggests that non-radiative processes, as the Auger recombination process, do not play a relevant role in the luminescence properties of the system. PL lifetime measurements
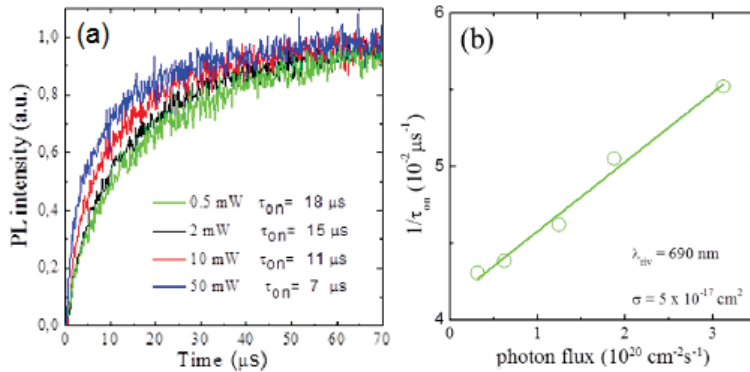
Figure 3.6: *(a) Normalized PL intensity vs the risetime at different excitation photon fluxes. (b) Reciprocal of the risetime as a function of the excitation photon flux. The slope of the curve gives an excitation cross section of $5 \times 10^{-17} cm^2$. The excitation wavelength was 488 nm and the detection wavelength was 690 nm.*

were performed by monitoring the decay of the PL signal after pumping to steady state and switching off the laser beam (overall time resolution 200 ns). The lifetime of the PL signal, measured at different wavelengths after the switching off of the excitation source, is reported in fig. 3.7. The lifetime has the shape of a stretched exponential $(I_{PL} = I_0 exp(-t/\tau)^\beta)$ and increases with increasing wavelength with values in the range between 15 and 40 μs. These values are two orders of magnitude above those reported for pillars produced by e-beam lithography plus oxidation [19] demonstrating that the quality and efficiency of the present NWs is superior by orders of magnitude.

3.2.2 Temperature dependence of the PL emission

Further information about the origin of the PL from Si NWs, as well as useful information about their perspectives for practical applications, can be obtained by following the temperature dependence of the PL signal. These measurements are reported in fig. 3.8.a, where the PL intensity (I_{PL}) at 690 nm of Si NWs is plotted as a
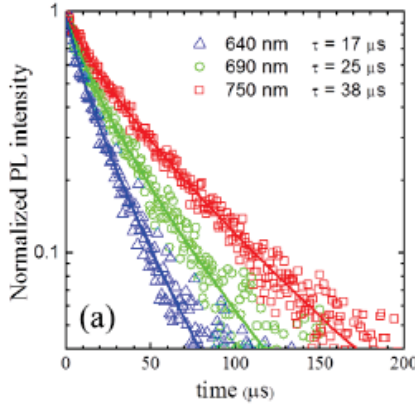
Figure 3.7: *PL lifetime of the Si NWs at different emitting wavelengths. The excitation wavelength was 488 nm and the detection wavelength was 690 nm.*

function of the temperature in the range 11-300 K. The data show that I_{PL} monotonically increases with the temperature up to about 270 K, where the maximum intensity is found. Above this temperature a slight decrease of I_{PL} is observed. The overall dependence on temperature is relatively weak, since the intensity change between 11 and 270 K accounts for about one order of magnitude. The PL lifetime as a function of the temperature, measured at a fixed wavelength of 690 nm is reported in fig. 3.8.b. The figure shows that the PL lifetime decreases by increasing the temperature; in particular, the decay time decreases from 200 μs at 11 K to 20 μs at room temperature, with a variation of about one order of magnitude. This behavior closely resembles that of quantum confined Si systems, such as Si NC [125] and porous Si [126], and it is a further confirmation of the occurrence of quantum confinement effects in Si NWs. It has been previously demonstrated [127] that, by solving the appropriate rate equation, the PL intensity I_{PL} can be expressed as:

$$I_{PL} \propto \sigma\phi\frac{\tau}{\tau_R}N \qquad (3.6)$$

where σ is the excitation cross section, ϕ the pumping beam photon flux, N the total population of emitting centers, τ the luminescence
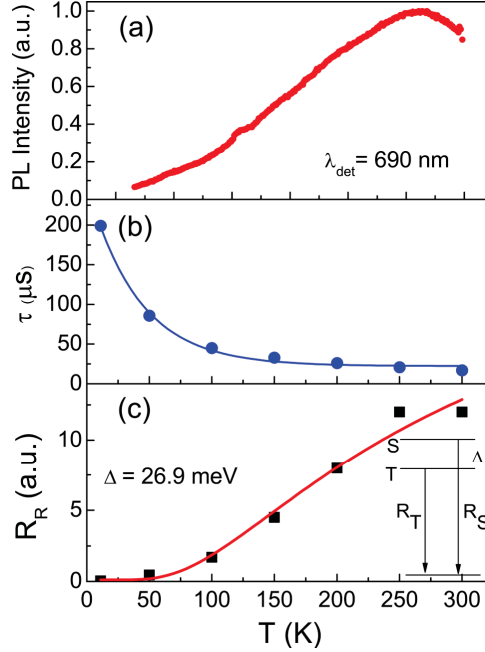
Figure 3.8: *PL properties of 150 days-aged Si NWs as a function of the temperature in the range 11-300 K. (a) Normalized intensity of the PL signal at 690 nm. (b) Lifetime of the PL signal, measured at a fixed wavelength of 690 nm. The blue line is a guide to the eyes. (c) Radiative rate ($R_R = 1/\tau_R$), extracted by the ratio between the PL intensity and the decay time at a fixed photon flux. The red line is a fit to the data, according to the model proposed in Refs. , with $\Delta = 26.9 \pm 4.3$ meV. In the inset the singlet and triplet energy levels split by the electronhole exchange energy Δ are schematically shown.*

decay time, including both radiative and non-radiative processes and τ_R the radiative lifetime. In the low pump power regime, I_{PL} increases linearly with pump power and it is proportional to the ratio τ/τ_R. Since N and σ are temperature independent, the only temperature dependences are due to τ and τ_R. In presence of non-radiative processes τ does not coincide with τ_R and I_{PL} depends on temperature. The temperature dependence of the radiative rate $(R_R = 1/\tau_R)$ can be extracted by the ratio between the PL intensity and the decay time at fixed photon flux, as shown in fig. 3.8.c, where the radiative rate in arbitrary units at each temperature is calculated by dividing the PL intensity by the decay time. R_R increases by about a factor of 200 on going from 11 to 300 K, and this increase is partially counterbalanced by a simultaneous increase in the efficiency of the non-radiative processes as suggested by fig. 3.8.b, showing a marked PL lifetime shortening when the temperature is increased. Since it is well known that non-radiative processes are characterized by very fast decay times, we can conclude that these processes have an increased role in the de-excitation dynamics of Si NWs when the temperature is increased. The behavior of the radiative rate can be explained with a model proposed by Calcott et al. [126] for porous Si and applied also to Si NC [125, 127]. According to this model the exchange electron-hole interaction splits the excitonic levels by an energy Δ. The lowest level in this splitting is a triplet state and the upper level is a singlet state. The triplet state (threefold degenerate) has a radiative decay rate R_T much smaller than the radiative decay rate R_S of the singlet. Once excited the excitonic population will be distributed according to thermal equilibrium law. Hence at a temperature T the radiative decay rate will be:

$$R_R = \frac{3R_T + R_S exp\left(-\frac{\Delta}{kT}\right)}{3 + exp\left(-\frac{\Delta}{kT}\right)} \tag{3.7}$$

Equation 3.7 suggests that, by increasing temperature, the relative population of the singlet state will increase and, being the radiative rate of the singlet state much higher than that of the triplet state, also the total radiative rate will consequently increase. We have used this formula to fit the data in fig. 3.8.c. Indeed the con-

tinuous line is a fit to the data with $\Delta = 26.9 \pm 4.3$ meV. This value is in good agreement with those previously found for porous Si [126] and Si NC [125, 127], confirming the occurrence of quantum confinement effects also in Si NWs. Note also that similar values of the level splitting have been recently theoretically calculated for Si NWs [128], though no experimental data existed. Calculations of the splitting of the excitonic levels at detection wavelengths different than 690 nm have been done and the results, showing an increased splitting for lower wavelengths (corresponding to smaller NWs), are in agreement with literature [125, 126].

3.2.3 External quantum efficiency

In order to estimate the photoluminescence (PL) efficiency of our Si NWs, we first proceed to the determination of their spatial emission profile in the far-field. Figure 3.9.a reports the integrated PL intensity as a function of the emission angle ϑ, as measured by optically pumping ($\lambda_{exc} = 405$ nm) the Si NWs at a fixed excitation angle with respect to the sample surface. The angular dependence of the PL intensity can be very well fitted by a cosine function (red line in the fig. 3.9.a), which demonstrates that our Si NWs sample behaves as a perfect Lambertian source. This allows to estimate the total PL emission of the Si NWs by measuring the light emitted within a given solid angle around normal direction, and then weighting it to the total emission power of a Lambertian source. The PL power efficiency is then given by the ratio between the total PL emission power and the absorbed excitation power. According to the emission properties of a Lambertian source, we have for the total emission intensity I_{tot}:

$$I_{tot} = 2I_{max} \int_0^{\pi/2} \int_0^{2\pi} cos(\theta)sin(\theta)d\theta d\phi =$$

$$= 4\pi I_{max} \int_0^{\pi/2} cos(\theta)sin(\theta)d\theta = 2\pi I_{max} \qquad (3.8)$$

On the other hand, for the same source, the light emission intensity collected within a solid angle of angular aperture 2α around the
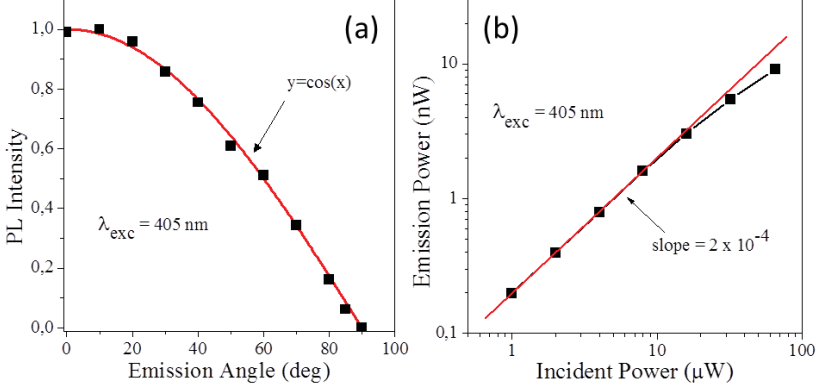
Figure 3.9: *(a) Normalized angular dependence of the spectrally inte-grated photoluminescence from Si-NWs (square dots), as compared to the Lambertian cosine law (red line). (b) Power efficiency curve of the light emission from Si-NWs. Red line is a linear fit in the low pump-power regime.*

normal direction will be:

$$I_{2\alpha} = I_{max} \int_0^\alpha \int_0^{2\pi} cos(\theta)sin(\theta)d\theta d\phi =$$

$$= 2\pi I_{max} \int_0^\alpha cos(\theta)sin(\theta)d\theta = \pi I_{max} \left[1 - cos^2(\alpha)\right] \qquad (3.9)$$

Thus, if $P_{2\alpha}^{exp}$ is the PL power measured within a solid angle of angular aperture 2α around the normal direction and P_{exc} is the absorbed excitation power, the PL external power efficiency will be given by:

$$\eta_P = \frac{P_{2\alpha}^{exp}}{P_{exc}} \frac{I_{tot}}{I_{2\alpha}} = \frac{P_{2\alpha}^{exp}}{P_{exc}} \frac{2}{\left[1 - cos^2(\alpha)\right]} \qquad (3.10)$$

Fig. 3.9.b shows the measured power efficiency curve of our Si NWs as obtained by optically exciting the sample with a $\lambda = 405$ nm laser beam and collecting the PL emission with an objective lens of numerical aperture NA = 0.4 = sinα. Under the conservative

92

assumption that the 405 nm exciting laser beam is totally absorbed by the Si NWs, we obtain from the experimental data:

$$\eta_P = \frac{P_{2\alpha}^{exp}}{P_{exc}} \frac{I_{tot}}{I_{2\alpha}} = 2 \times 10^{-4} \frac{2}{1 - cos^2(sin^{-1}0.4)} \qquad (3.11)$$

The external quantum efficiency is then obtained by normalizing to the photon fluxes of the excitation and emission beams:

$$\eta_Q = \eta_P \frac{3.0\,eV}{1.77\,eV} = 5 \times 10^{-3} \qquad (3.12)$$

A lower limit estimate of the external quantum efficiency is hence 0.5%.

3.3 Surface passivation in Si NWs

The PL intensity exhibits a marked aging effect. This behavior is illustrated in fig. 3.10, where the intensity of the PL signal at 690 nm at room temperature of freshly prepared Si NWs is plotted as a function of the air exposure time. The PL signal is seen to monotonically increase as a function of the air exposure time; the experiment has been conducted up to 245 days, and within this time lapse, an increase of the PL intensity accounting for a factor of 250 has been found. No noticeable variation of the peak position and shape has been observed during the whole experiment. Two different interpretations of the observed aging phenomenon are possible: since it is known that Si surfaces, especially if freshly etched, can interact with atmospheric reactive gases such as O_2 or H_2O [129], the increase of the PL signal as a function of air exposure time can be due to the formation of new luminescent surface states. Under this hypothesis, the PL from Si NWs should be due to surface emitting centers (such as siloxene and its derivates [82, 130]) whose number increases due to the progress of the surface reactions with gaseous species. In contrast, since it is well known that Si nanostructures exhibiting quantum confinement effects need an efficient surface passivation in order to suppress the non radiative de-excitation channels which could limit the efficiency of the light emission process, the effect
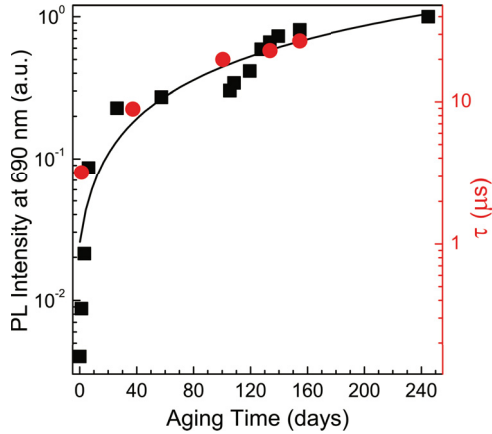
Figure 3.10: *Normalized intensity of the PL signal at 690 nm of freshly prepared Si NWs as a function of the air exposure time at room temperature (black squares). The line is a linear fit to the data. The lifetime of the PL signal, obtained by following the decrease of the PL signal at 690 nm after the laser switch-off, as a function of the aging is also presented (red circles, righthand scale). During the experiment the sample is exposed to the laser beam only for the brief time needed for PL data acquisition. The inset reports a typical PL spectrum obtained from a 150-days-aged sample. The PL data are obtained by exciting the sample with the 488 nm line of an Ar+ laser at a pump power of 10 mW.*

of aging could be ascribed to an improvement of the surface passivation of the quantum confined Si NWs, through heterogeneous (gas-solid) reactions involving O_2 or H_2O, leading to the formation of Si-H, Si-O or Si-OH bonds. To discriminate between the two above described effects, we have studied the lifetime of the PL signal as a function of the aging by following the decrease of the PL signal at 690 nm after the laser switch-off. The lifetime data are reported in fig. 3.10 as red points and indicate the occurrence of an increase of the lifetime as a function of the aging; in particular, a lifetime value of about 30 μs has been observed in 245-days-aged samples. The common trend as a function of the aging exhibited by PL intensity and lifetime strongly suggests that aging produces an efficient surface passivation of the quantum confined NWs, and, in turn, a reduction of the number of sites acting as centers for non-radiative recombination. The occurrence of quantum confinement effects has been confirmed by the observation that the PL signal can be shifted by synthesizing NWs having a different mean size. We remark finally that the absence of saturation of the PL intensity in the explored time range (the behavior is roughly linear within the whole time lapse) puts clearly into evidence the huge surface area of this material. The effect of passivation on the PL properties of Si NWs has been also studied by following the behavior of the PL intensity at 690 nm during a prolonged exposure to the laser source used for PL experiments (488 nm, 10 mW). The results are reported in fig. 3.11; in particular, the red points illustrate the behavior of the PL intensity at 690 nm of 150 days-aged Si NWs when the laser is left on the sample kept in air. The PL intensity increases by approximately a factor of 1.5 in a time lapse of 2000 s; the increase of the signal is sub-linear but, remarkably, no steady state is reached even in longer experiments. The effect of the laser resembles that of an accelerated aging; indeed the laser-induced decomposition of gaseous molecules such as O_2 or H_2O increase the rate of the heterogeneous surface reactions leading to the NW passivation. Since also laser-induced desorption phenomena simultaneously occur, the observed increase of the PL signal is the result of the competition between the two effects. This explains the sublinear increase of the PL intensity shown in fig. 3.11, to be compared with the linear increase of fig. 3.10, where no phenomena competing with passivation
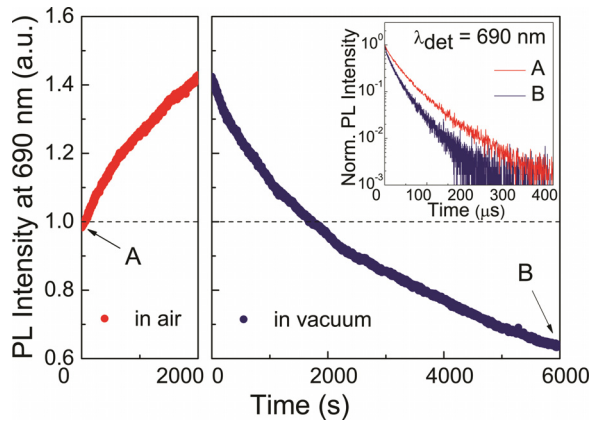
Figure 3.11: *Normalized intensity of the PL signal at 690 nm of 150 days-aged Si NWs as a function of the exposure time to an Ar^+ laser beam (488 nm, 10 mW). Data refer to laser irradiation with the sample kept in air (red points) or in vacuum (blue points). The dashed line represents the starting PL intensity. In the inset, the comparison between the PL decay curves of 150-daysaged NWs, at the beginning of the irradiation experiment (indicated with A) and after irradiation in vacuum for 6000 s (indicated with B), is reported.*

Figure 3.12: *(a) Normalized PL intensity of a 40-days aged sample of Si NWs before (red curve) and after (blue curve) a treatment in water vapor for 5 min. (b) Decay lifetimes of this 40-days aged sample of Si NWs before (red curve) and after (blue curve) treatment in water vapor for 5 min. Both the PL intensity and the lifetime increase of the same factor.*

are operating. On the other hand, if, after the 2000 s laser exposure, the sample is transferred in vacuum at a pressure of about 10^{-5} Torr, and we continue the laser exposure, the PL signal at 6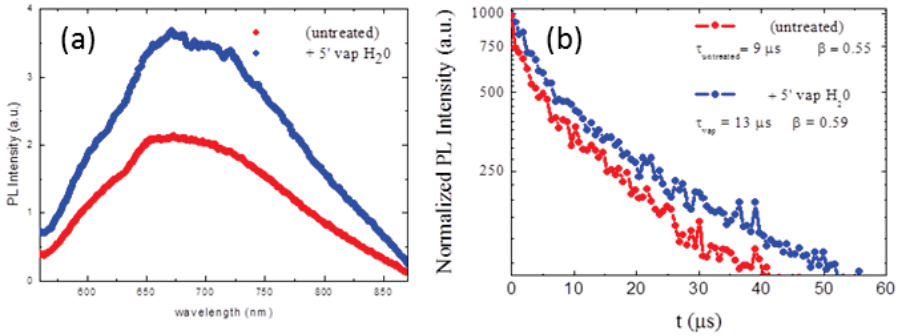90 nm is seen to progressively decrease (blue points in fig. 3.11), and an intensity lower than the initial one (represented by the dashed line) is reached in a few thousands of seconds. This effect is due to the fact that, in vacuum, no further formation of surface oxidized species can occur and desorption becomes the only operating phenomenon. As a final result, the PL intensity decreases because, in absence of a good surface passivation, non-radiative processes limit the PL efficiency of the system. It is remarkable that the PL intensity observed at the end of the experiment is weaker than the starting one, since this demonstrates that laser irradiation in vacuum is able not only to destroy the effect of the laser irradiation in air, but also to partially remove the NW passivation due to the 150 days of aging of the sample. We underline that the experiments illustrated in fig. 3.11 have been conducted by recording the whole PL spectrum. No relevant variations of the shape (including both the FWHM and the position of the maximum) of the PL peaks were found during the whole experiment, so that the conclusions derived from the figure do not change if we replace the PL intensity
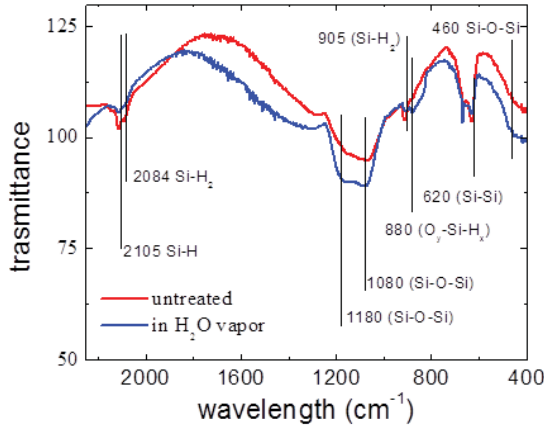
Figure 3.13: *Transmittance FTIR spectra of a 40-days aged sample of Si NWs before (red curve) and after (blue curve) a treatment in water vapor for 5 min.*

at a single wavelength with the integrated PL intensity. The inset of fig. 3.11 reports the comparison between the PL decay curves at 690 nm of 150-days-aged NWs, at the beginning of the irradiation experiment (indicated by A) and after irradiation in vacuum for 6000 s (indicated by B). The above discussed enhanced efficiency of non-radiative processes in samples irradiated in vacuum is clearly evidenced by the lifetime shortening from 27 to 16 μs. Figure 3.12.a shows the normalized PL intensity of a 40-days aged sample of Si NWs before (red curve) and after (blue curve) a treatment in water vapor for 5 min. A permanent increase of the PL intensity by a factor $I_{vap}/I_{untreated} = 1.7$ is observable. Moreover, also the PL lifetime increases by the same factor $(\tau_{vap}/\tau_{untreated} = 1.5)$, as shown in fig. 3.12.b. This effect could be due to an accelerate passivation of the dangling bonds in the surface of Si NWs with Si-O-Si bonds, similar to a wet oxidation, as shown in the transmittance Fourier Transform Infrared Spectroscopy (FTIR) spectra of fig. 3.13, from where absorption is clearly enhanced after wet oxidation. Passivation with other species, e.g. $Si-H$ or $Si-H_2$ or O_y-Si-H_x bonds is less probable.
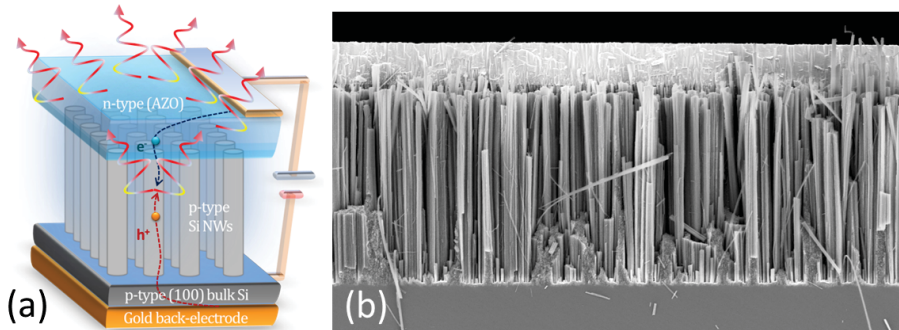
Figure 3.14: *(a) Cross section SEM image of an axial p-n junction formed by an Aluminum Zinc Oxide (which is natively a n-type material) layer grown on p-type Si NWs made by metal assisted etching. (b) A sketch of the directly biased Si NWs light emitting device.*

3.4 A Si NWs light emitting device at room temperature

The capability of Si NWs to emit photons if electrically excited, and therefore to constitute the active region in Si-based light emitting devices operating at room temperature, has been tested by fabricating prototype devices. The device structure is sketched in figure 3.14.a: p-type Si NWs have been formed by etching a Si substrate containing a B concentration of $1.5 \times 10^{20} cm^{-3}$, corresponding to a resistivity of $8 \times 10^{-4} cm^{-3}$. The electrical contacts have been realized by depositing a 900 nm thick Au layer on the back of the Si substrate and a 1300 nm thick layer of a transparent conductive oxide (AZO) on the Si NWs. AZO is a conductor n-type material, and therefore it forms a p–n junction with the underlying p-type NWs. The junction is shown in fig. 3.14.b. The AZO layer allows current injection in the device without absorbing the emitted photons, being characterized by a transmittance of about 85% in the spectral range 480–1300 nm. Devices have a rectangular shape, with dimensions of the order of a few millimeter. Figure 3.15.a shows the IV curve of the device. The pn-junction characteristic is clearly visible, both in direct and reverse bias. The EL spectra of a device forward biased at voltages between 2 and 6 V are
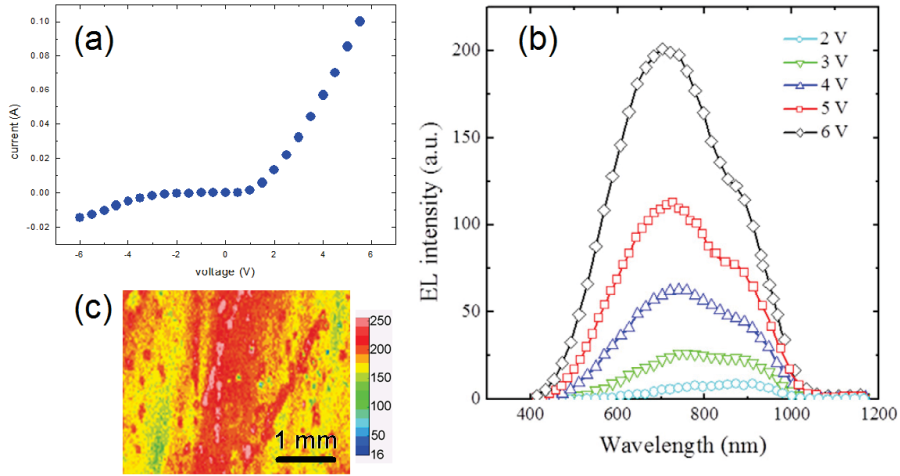
Figure 3.15: *(a) I/V curve (dark) of the Si NW light emitting device. (b) Electroluminescence spectra at different direct bias voltages. (c) Top-view emission microscopy (EMMI) of a 10 mm² area of the device.*

shown in figure 3.15.b. They consist of a broad band, centered at about 700 nm. The shape and the position of the EL spectra are similar to those of the PL spectra shown in figure 3.5.a; this similarity constitutes strong, although indirect, evidence of the fact that both mechanisms of excitation involve the same emitting centers, i.e. quantum confined Si NWs. Note that the intensity fluctuations visible in the EL spectra are due to interference phenomena induced by the presence of the AZO overlayer, while the intensity increases roughly linearly by increasing the current with operating voltages in the range 2-6 V. Moreover, the EL intensity is quite constant even in a large area of the device, as shown in the Emission Microscopy (EMMI) in fig. 3.15.c. Even if this device is a prototype, these results can be considered extremely promising together , if compared to other silicon based light emitting devices. In fact, light emitting devices made on silicon NWs allow a lower resistance than light emitting devices made in silicon nanocrystals embedded in silicon dioxide, and definitely lower operating voltages.

3.5 Coherent enhanced Raman backscattering from Si NWs fractal arrays

The design of new textures of nanowire materials and the optimization of dimensions and spatial arrangement play a key role on the improvement of the optical properties, such as light trapping and multiple scattering, towards important phenomena as coherent backscattering [131, 132], Anderson localization of light [133, 134] and random lasing [135, 136, 137, 138]. Si NWs are known to exhibit also a strong Raman activity, depending on the morphology and the array arrangement [139, 140, 141, 142, 143]. The demonstration of coherence effects and high directionality in the Raman emission from Si NWs towards the perspective of a Raman gain in the visible wavelength range, where the material is absorbing, is yet a challenge and it could lead to the possibility of realizing an ultralow threshold continuous-wave nanowire Raman laser. The texture of the NWs medium is responsible for a very high light trapping, Anderson localization and recurrent multiple scattering events that lead towards the first experimental evidence of a coherent enhanced backscattering cone of the Raman signal of Si NWs. The 2D fractal geometry of the Si NWs has been shown in fig. 2.4 of chapter 2. This texture is obtained after the deposition process of the thin gold layer quite below the percolation limit (54% of estimated surface coverage) and then imposed on Si NWs as a negative mask during the wet etching procedure. The 2D fractal geometry and the lack of translational invariance can lead to wave spatial localization inside the system [144, 145]. This sort of localization, in which a wave cannot propagate through a disordered medium because of strong scattering, was predicted by Anderson and it is a general phenomenon of waves, which applies equally to the propagation of sound and light [134].

To uncover the light-scattering properties of our Si NWs forest we first study the optical reflectance in the visible to the near-infrared spectral range. The diffused and total reflectance spectra were accurately measured in the range 200 - 1800 nm by means of a double-beam spectrophotometer (Varian, CARY 6000i) equipped with an integrating sphere. In the diffused reflectance geometry, the spec-
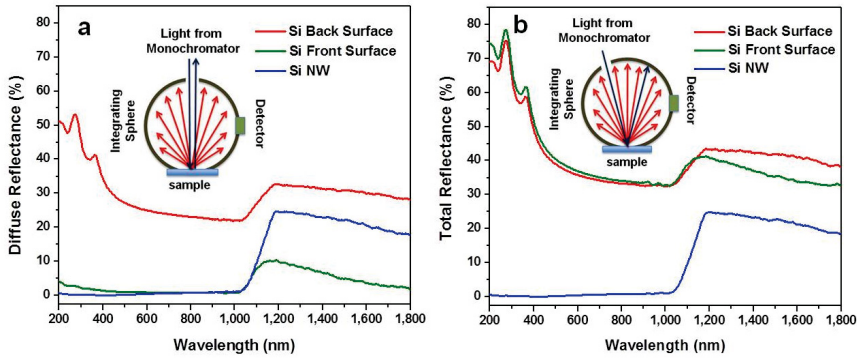
Figure 3.16: *Experimental evidence of light trapping property of fractal array arranged Si NWs. a,b. Diffuse (a) and total (b) reflectance of Si NWs sample (blue lines) and of a bulk c-Si front and back surfaces (green and red lines respectively).*

ular component of the light reflected at the sample surface is excluded from the integrating sphere (see the scheme in fig. 3.16.a), allowing the measurement of the diffused light only. In the total reflectance geometry, both the specular and diffused components are sent to the detector in the integrating sphere (see the scheme in fig. 3.16.b). Figure 3.16.a shows the diffuse reflectance, obtained by excluding the specular component, in three different cases: a SiNW forest, an optically flat Si sample and an optically rough Si sample, the back surface of a silicon wafer with a roughness in the tens of microns scale. In this latter case, the diffuse reflectance assumes the values expected from the Fresnel coefficients at the Si-air interface, indicating a simple diffusing behavior over all the investigated spectral range. Notice the marked step in the spectrum at 1.1 μm wavelength, corresponding to the suppression of the back-surface reflection in the sample due to optical absorption above the Si electronic bandgap. On the other hand, a clear evidence of two different diffusion regimes is observed in the Si-NW sample. In fact, while in the non-absorbing region the diffuse reflectance displays a behavior similar to that measured in the rough Si sample, for wavelengths above the Si bandgap we observe a sharp drop to near-zero reflection (lower than 1%). Such a behavior gives a clear evidence of a strong light-trapping and absorption mecha-

nism through multiple-scattering diffusion from the Si NWs forest. This is further supported by the total reflectance spectra of the same set of samples, obtained by measuring both the diffused and specular components, as shown in fig. 3.16.b. Here, in the strongly absorbing visible region, the total reflectance of the rough Si sample assumes high values and is very similar to that one of the flat Si sample (for which the total reflectance coincides with the specular reflectance), thus confirming the single-scattering nature of the diffusion occurring in the rough Si sample. However, in the Si NWs sample the short wavelength total reflectance keeps always to very low values as for the diffuse reflectance, demonstrating a strong absorption due to multiple scattering. A similar black body experimental evidence has been recently demonstrated for a forest of single-walled carbon nanotubes [146]. A key role in this behavior is played by the texture of the sample that supports a very high light trapping efficiency and that is enhanced at normal incidence to the top of the NWs. Indeed, due to the low reflection, almost all the light propagates through the forest and interacts with the nanowires walls, then, at each interaction, it is absorbed, transmitted and reflected inside the sample more times as in a trap until the complete absorption occurs.

Micro-Raman spectra have been acquired in a back-scattering configuration by using a Horiba-Jobin Yvon spectrometer. This set up allows for a multi-wavelength excitation making use of a He-Ne, two argon ion lasers, one used to produce the UV line at 364 nm and the other one for the visible wavelengths, and a diode laser at 785 nm. The excitation powers were maintained very low (ranging between hundred and tens microwatts, depending on the laser wavelength) and the laser beams were focused by using a 100X objective (NA = 0.9) in the visible and near IR excitation spectral range and a fluorinated 60X (NA = 0.9) in the UV excitation. Angle-resolved Raman spectra have been acquired by means of a home-made goniometer coupled to a liquid nitrogen cooled Si-CCD (Spec 400 BR, Princeton Instruments), with an angular resolution of about 2° set by the collection optics. A variable-angle excitation has been obtained by means of a 488 nm CW solid state laser focused to a 100 μm diameter spot onto the sample surface. In figure 3.17.a the optical emission spectrum obtained by exciting the investigated sample
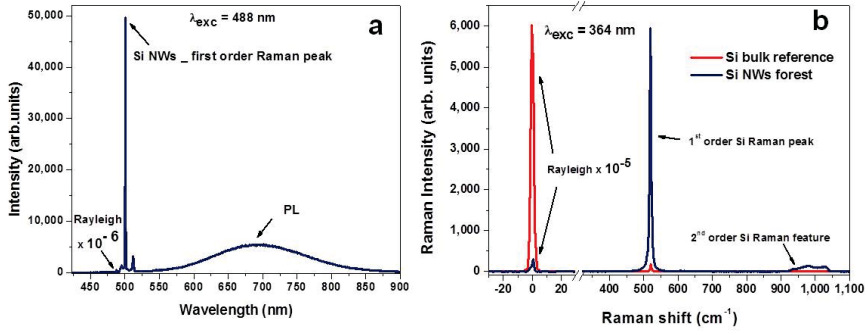
Figure 3.17: *Raman enhancement evidences of Si NWs fractal array sample due to multiple scattering. (a) PL and Raman emission spectrum obtained by exciting Si NWs sample with the 488 line of a solid state laser at a pump power of 20 mW. The Rayleigh line was attenuated 10^{-6} times by using an edge filter. (b) Comparison between Raman spectra of Si NWs (blue line) and bulk c-Si (red line) obtained by exciting the samples with a 364 nm of an Ar^+ laser for 5s at a pump power of 0.4 mW; the Rayleigh line was here attenuated 10^{-5} times.*

with the 488 nm line of a solid state laser at a power of 20 mW is shown. The PL band, peaked at 690 nm, is clearly visible, however the most dominant feature is represented by an exceptionally strong first order Si Raman peak at 500.7 nm (about 520 cm^{-1} of Raman shift). In figure 3.17.b the Si NWs forest Raman spectrum (blue line) under an excitation wavelength of 364 nm and a power of 0.4 mW focused to a spot of about 1 μm diameter is shown. Its intensity as compared to that of the single-crystalline Si (c-Si) used to obtain the NWs sample (red line), appears strongly amplified (about 37 times); this occurrence makes the SiNWs Raman signal detectable also at very low incident laser power (until 100 nW). Note that only a 21% of Si surface coverage is estimated by SEM images after the wet-etching process in the NWs sample when the wires process is complete, if the fractal like texture is considered (see fig. 2.4b,c,d in chapter 2), while the crystalline core of Si NWs that gives a significant Raman contribution covers only about 13% of the probed total area, due to their surface oxidation. The actual Raman enhancement, if we normalize for the silicon volumes, is hence by a factor of 285. On the other hand, in fig. 3.17.b a
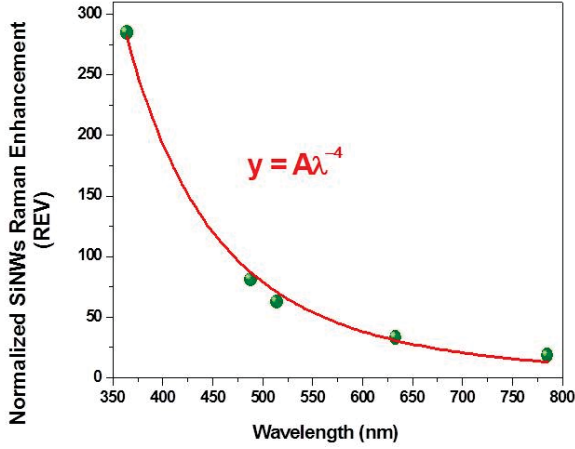
Figure 3.18: *Raman enhancement evidence of Si NWs fractal array sample due to multiple scattering. Plot of the Si first order Raman enhancement per unit volume (REV) as a function of the incident wavelength for Si NWs compared to the signal of the bulk silicon used as reference. The red line is the best fit curve that exhibits a λ^{-4} dependence.*

reverse phenomenon can be noticed in the Rayleigh peak, which is drastically reduced as compared to that of c-Si. We register a considerable Si NWs Raman enhancement compared to the c-Si signal by exciting in the entire visible spectral range. In figure 3.18 it is shown the trend of the Raman enhancement value per unit volume (REV) as a function of the incident wavelength. The REV is obtained by evaluating the ratio between the Si NWs and the c-Si Raman intensities and then normalizing to the scattering volumes, as:

$$REV = \frac{I_{NW}V_{c-Si}}{V_{NW}I_{c-Si}} \qquad (3.13)$$

In the last few years, a significant Raman enhancement for individual Si-nanowires has been demonstrated and explained in terms of structural resonances in the local field [139, 140] lightened at some characteristic laser wavelengths. However, as clearly deducible from the best fit of the data shown in fig. 3.18, the REV exhibits a λ^{-4} dependence that is far from the resonant Raman effects reported in literature [139, 140, 141, 142, 143]; we attribute this trend as a
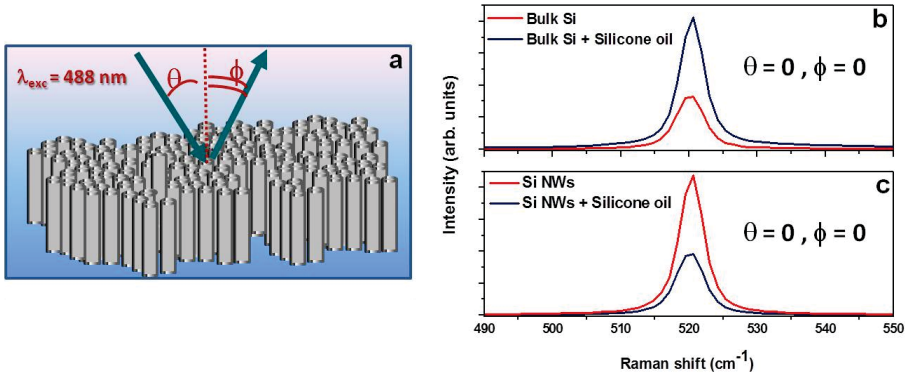
Figure 3.19: *Further experimental evidences of Raman enhancement from Si NWs array due to multiple scattering. (a) Sketch of the experimental conditions used for angle resolved Raman measurements, where θ is the angle formed by the laser beam propagation direction and the normal axis to the NWs sample surface (incidence angle) and ϕ is the detection angle of the Raman signal coming from the sample. (b,c) Raman spectra taken at $\theta = 0, \phi = 0$ showing the comparison between first order Si peaks in absence (red lines) and in presence (blue line) of Silicone oil for bulk c-Si used as reference (b) and Si NWs (c).*

function of λ to an explicit fingerprint of the multiple scattering nature of the observed phenomenon. Then, as assumed by Kastler theory [147], as a result of multiple scattering events, a redistribution of the scattered photons in the field of allowed Rayleigh and Raman frequencies occurs, as a consequence the Rayleigh photons will decrease exponentially following a geometrical progression and pumping the Raman photons population. To corroborate the role of multiple light scattering on the Raman signal intensity in our system, we added a drop of silicone oil to the sample, aiming to change the refractive index mismatch at the NWs interfaces $Si/SiO_2/air$. In fig. 3.19 we compare the Raman spectra of Si NWs and the c-Si reference before and after the silicone oil addition (refractive index 1.6). The spectra are taken in a backscattering experimental configuration (see sketch in fig. 3.19.a for θ=0 and ϕ=0). Due to its optical transparency and high refractive index, the silicone oil acts as an antireflection layer at the Si-air interface, thus increasing the transmitted light that is responsible for the Raman excitation. As a

result, the Raman scattering intensity for the reference bulk-Si sample is markedly increased as compared to the same sample without oil, as shown in fig. 3.19.b. On the other hand, the opposite behavior is observed when adding the silicone oil to the Si NWs sample, as reported in fig. 3.19.c. In this case, the introduction of silicone oil into the interstitials between Si NWs has the additional effect of substantially reducing the light scattering ability by lowering the refractive index contrast at the interfaces $Si/SiO_2/air$, which leads to a suppression of multiple scattering and a consequent reduction in the measured Raman signal. Such a behavior represents a further strong evidence that the observed Raman scattering enhancement form Si-NWs forest is indeed due to a multiple scattering effect.

We finally explore the angular dependence of the multiple light scattering behavior by recording the enhanced Raman signal from Si NWs as a function of both the excitation angle θ and the collection angle ϕ (see sketch in fig. 3.19.a). The results are shown in figure 3.20.a, where a strong deviation from the expected angular-dependent Raman scattering intensity of Si (111) is observed for scattering angles close to normal excitation (note that the c-Si curves, solid lines in figure, are multiplied by a factor of 80 to allow a comparison with the NWs data). The enhanced Raman backscattering (here in ERBS) cone, especially around its center, appears to be clearly cusped both at small positive and negative detection angles with respect to the incident radiation. This surprising behavior for the Raman signal closely resembles the observations for light diffusion in strongly scattering materials, where the constructive interference between forward and backward multiple-scattering optical paths gives rise to the well known phenomenon of coherent backscattering. Enhanced Raman scattering from vertical silicon nanowires ordered arrays has been recently demonstrated in literature due to the combined effect of optical resonances from single wires and the confinement of light within the arrays [141, 142], however the present work shows for the first time a cone of strongly enhanced Raman signal in the backscattering direction. On the other hand, coherent Rayleigh backscattering cones with a wide angular aperture has been recently observed in GaP NWs arrays [148], but here we show the same angular dependence for the Raman scattering never seen until now.
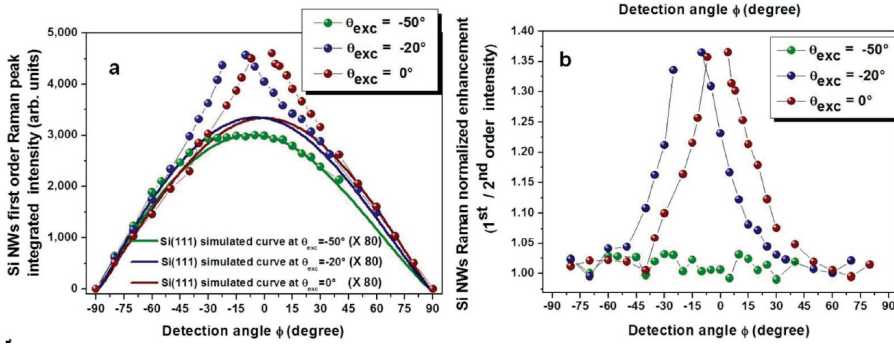
Figure 3.20: *Experimental evidences of coherent Raman backscattering in Si NWs. (a) Angular dependences of the integrated intensity of the first order Si Raman peak of the NWs sample fixing the incidence angle of the laser beam at $\vartheta=0°$ (red wine) $\vartheta=-20°$ (blue) and at $\vartheta=-50°$ (green). The continuous lines represent the calculated Raman emission curve for a Si(111) surface as a function of the detection angle for $\vartheta=0°$ (red wine), $\vartheta=-20°$ (blue line) and $\vartheta=-50°$ (green). The calculated curves are normalized to the intensity values of Si NWs sample by a multiplying factor of 80. (b) Angular dependence plot of the first to second order Si Raman peak intensity ratio in Si NWs for incident radiation angles $\vartheta=0°$ (red wine), $\vartheta=-20°$ (blue) and $\vartheta=-50°$ (green) normalized to the average value obtained for $\vartheta=-50°$.*

An important point is that the ERBS cone is detected when the laser light forms small angles with the normal to the sample surface, up to about 20°, while for increasing angles of incidence this peculiar feature is progressively smoothed out. As shown in fig. 3.20.a, at wide incidence angles ($\theta = 50°$) the Si NWs Raman signal perfectly follows the angular dependence of that one coming from a Si (111) surface in the same experimental configuration, here the solid green line represents the calculated unpolarized Raman scattering curve for a Si (111) surface as a function of the detection angle when $\theta = -50°$ multiplied by a factor 80 (see ref. [149]for simulation details). To exclude shadow effects due to the absorption of the Raman emission by the Si NWs side walls we explored the angular dependence of the Raman scattering at $\theta = 0°$ by using the 785 nm line of a diode laser as excitation wavelength, where the Si is characterized by a lower absorption coefficient while the sample yet shows an high light trapping efficiency. Also in this experimental configuration we obtained a well defined ERBS cone, while the PL emission, excited by using a 488 nm at incidence angle close to the normal and measured in the range between 550 and 900 nm, shows a perfect Lambert's cosine law (shown in the previous paragraph). Moreover, by analyzing the angular-dependent Si Raman spectra we find that for small angles around the backscattering direction, a systematic enhancement of the first order Si Raman peak as compared to the second order peak occurs. This feature disappears at wide incidence angles ($\theta = 50°$), for which the angular dependence of the second order peak is similar to that one obtained for the first order peak, and no significant change in the ratio as a function of the detection angle is observed. In fig. 3.20.b the $1^{st}/2^{nd}$ order intensity ratio is shown for all the investigated excitation angles and normalized to the constant value obtained for $\theta = -50°$ (green). Adopting this procedure the backscattering enhanced cones of the first order Si Raman peak are well visualized because of the exclusion of the diffusive background. The ERBS cones here shown strongly support the occurrence of a phase matching between the laser beam and the backscattered Raman radiation that is not straightforward due to the spatially incoherent nature of the spontaneous Raman scattering process.

In order to correctly interpret the previous experimental evidences

we make here some considerations. We demonstrated that the 2D fractal-like texture of the Si NWs sample allows for multiple scattering of light and we know that, due to the the lack of translational invariance, wave spatial localizations inside the system may occur. The condition to be achieved for the observation of localized modes is the fulfillment of the Ioffe-Regel criterion $2\frac{\pi}{\lambda}l_s \leq 1$ [150], that for optical waves is obtained when the wavelength of light λ is close to the scattering mean-free path l_s (i.e. when $2\frac{\pi}{\lambda}l_s \leq 10$), and in a fractal system like this it is certainly satisfied allowing for a recurrent multiple scattering and possibly Anderson localization of light in some points. We propose that in our system the activation of recurrent multiple scattering phenomena, leading to Anderson localization of light, is established by the incidence angle of the pump laser beam and then by the light trapping efficiency that is enhanced at normal incidence to the top of the NWs. Then we suggest that exactly along these loop-type recurrent paths, acting as ring cavities where the scattered laser field joins very high intensities, also the Raman photons that propagate with a wavevector that closely phase matches that one of the incident radiation, could experience the maximum of multiple scattering events. Moreover we expect that, along these optical paths, the Rayleigh scattering is subjected to a coherent backscattering process due to the constructive interference between forward and backward multiple-scattering. As a consequence we can deduce that, due to an analogous process, also the Raman scattered photons involved in the loop-type recurrent paths and then showing phase matching with the laser field coherently interfere, even if with an expected lower coherence degree compared to that one of the Rayleigh radiation. The proposed mechanism is not far from the well known stimulated Raman scattering process [151, 152] (SRS) where the coherent emission exhibits a narrow cone in the forward and backward directions with respect to the pump laser. The crucial differences are that the SRS is a nonlinear optical process where the Stokes intensity gains exponentially with the propagation distance through the medium, while the coherent Raman backscattering here proposed cannot join value higher than twice the diffusive Raman background contribution, in analogy with the coherent Rayleigh backscattering phenomena, and remains a linear phenomenon. We could suppose that a
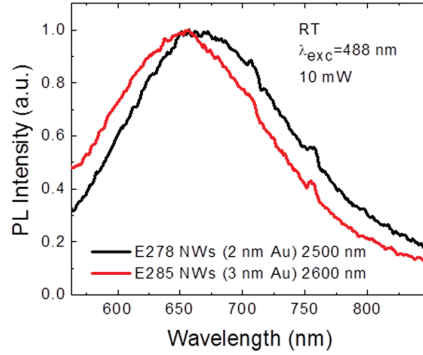
Figure 3.21: *Room temperature PL of Si/Ge MQW NWs obtained by etching a Si/Ge MQW substrate covered by 2 nm Au and 3 nm Au respectively.*

SRS threshold is activated by the incidence angle of the pump laser beam , anyway the absence of a clear experimental evidence of a gain threshold with the laser power, makes us lean to propose a coherent Raman backscattering process.

3.6 Si/Ge MQW NWs photoluminescence properties

Si/Ge MQW NWs can be obtained by metal assisted etching starting from a Si/Ge MQW as a substrate. Their fabrication has been shown in par. 2.2.2. Si/Ge MQW NWs are constituted by 54 nm long nanowiskers of Si and by dots of Ge thinner than 1 nm, as confirmed by TEM analyses. This structure is repeated several times in each NW, for all its length. In this paragraph their optical properties will be highlighted. It will be shown that both of these two materials, Si wiskers and Ge disks give rise to luminescence phenomena. On the other hand, this system is slightly more complicate than bare MACetch Si NWs, because of the addition of Ge. In fact, the room temperature luminescence coming from quantum confined Si occurs anyway, as shown in fig. 3.21. This picture shows the room temperature PL of Si/Ge MQW NWs obtained by etching a Si/Ge MQW substrate covered by 2 nm Au and 3 nm Au

respectively. As demonstrated for Si NWs, also for Si/Ge MQW NWs an increasing thickness of gold should correspond to thinner NWs. In fact, the RT PL spectra shown in fig. 3.21 show that, by increasing the gold thickness the size decreases and the wavelength decreases according to quantum confinement effects. This effect is the same effect shown in fig. 3.5.a. in section 3.2 for Si NWs. From an energy point of view, fig. 3.22 depicts a flat band scheme of the Si/Ge/Si structure which is repeated 62 times in the Si/Ge MQW substrate and hence also in the Si/Ge MQW NWs after the etching is performed. Typically, each Si/Ge/Si is a quantum well for both electrons and holes, hence in this system the occurrence of quantum confinement effects is strongly expected. Both carriers should be confined in one dimension and free in the other two in the case of the Ge layers before NWs formation, while a 3D confinement is expected once the substrate is etched, hence for the Ge dots in the NWs. Figure 3.23.a shows the bulk Ge electronic bands at low temperature. The conduction band edges of the direct and of the most probable indirect recombination are highligted in red and green respectively. The relative energy gaps are highlighted in the table of fig. 3.23.b. Figure 3.23.c shows the PL spectrum of the Si/Ge MQW NWs (in blue) compared to the Si/Ge MQW substrate (in black),

Figure 3.22: *A sketch of the flat band scheme of the Si/Ge/Si structure which is repeated 62 times in the Si/Ge MQW substrate and in the Si/Ge MQW NWs.*

at 11K. The emission is peaked at 1 eV. The analysis has been conducted in Si/Ge MQW NWs obtained etching a substrate covered by 2 nm Au. An increase of the PL signal equal to 4.5 is observable. Considering that the NWs fill only 50% of the original substrate area, this increase is by one order of magnitude. Moreover, the vertical dashed curves in green and red corespond to the indirect and direct recombination in bulk Ge. It is striking to see that these energies are well below the observed ones for both the Si/Ge MQW substrate and NWs. This shift could be due to quantum confinement effects of the carriers along the direction perpendicular to the

(a)

(b)

	Si	Ge
E_Δ	1.170	0.946
E_L	2.01	0.741
E_0	4.185*	0.889
Δ_0	0.044	0.296
Ξ_d^Δ	−6.0	−4.92
Ξ_u^Δ	8.6	9.4
Ξ_d^L	−13.0	−12.3
Ξ_u^L	16.1	16.2
C_Γ	−17.5	−12.3
a_V	−4.54	−3.1
b	−2.1	−2.86

(c)
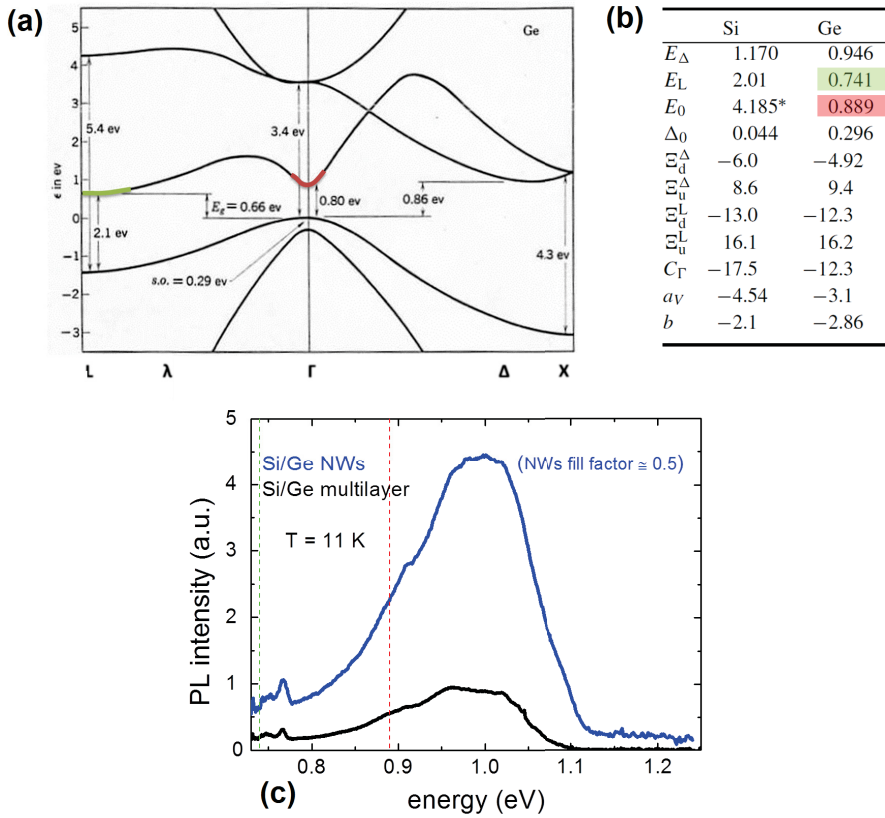
Figure 3.23: *(a) Electronic band structure of bulk Ge at 11K. (b) Table of the relative energy gaps at 11K. (c) IR PL spectra of Si/Ge MQW NWs in blue and Si/Ge. MQW substrate (in black).*

Ge layers, and it is a fingerprint of the 1D confinement in both the substrate and the Si/Ge MQW NWs. On the other side, the PL intensity increase by one order of magnitude can be due to an increase in the oscillator strength in the NWs, because of the 3D confinement of the Ge disk rather than the 1D confinement of each Ge layer in the substrate. Figure 3.24.a shows the PL intensity of Si/Ge MQW NWs measured at $\lambda = 1220$ nm (1 eV) as a function of the temperature.
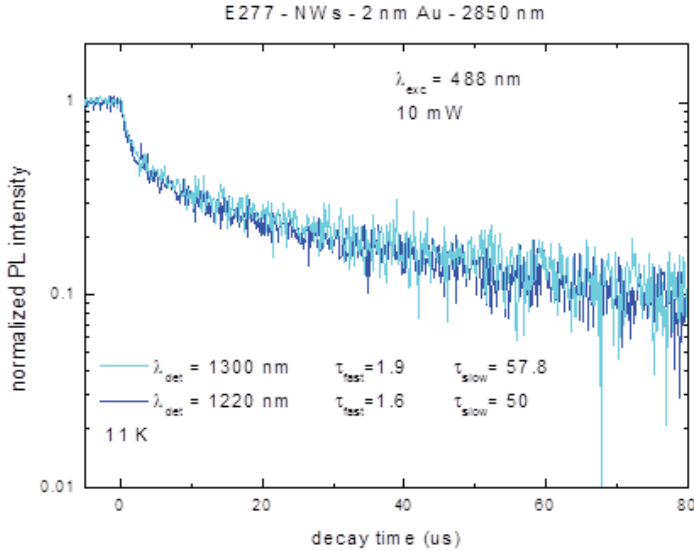
Figure 3.25: *Comparrison between IR PL lifetime decay at $\lambda_{det} = 1300$ nm and $\lambda_{det} = 1220$ nm.*

It shows that, by increasing the temperature, a quencing of the IR PL emission occurs. This is due to non radiative phenomena which arise by increasing the temperature, and which are faster than radiative ones. Moreover, a shift of the IR PL spectra is observable in figure 3.24.b. In fact, as the temperature increases, the normalized IR PL spectra shifts towards higher wavelengths (lower energies). This shift is a fingerprint of both the direct and indirect gap decrease as the temperature increases, due to the expansion of the lattice as the temperature increases. Moreover, the lifetime of the IR PL signal has been measured at two different detection wavelengths, i.e. 1220 nm and 1300 nm, and no significant change in the

Figure 3.24: *(a) IR PL intensity measured at 1220 nm as a function of the temperature (b) Normalized IR PL intensity at different temperatures, from 11K to 150K.*

lifetime has been observed. These curves are shown in figure 3.25. This means that the IR PL band comes from the same emitting center. An accurate analysis of the decay lifetime has been conducted and a double exponential decay can be observed. As it is shown in figure 3.25, there is an order of magnitude of difference between the "slow" (tens of μs) and the "fast" (μs) components of the lifetime decay. The presence of two different decay times demonstrates the clean existence of two different de-excitation channels. Figures 3.26.a and 3.26.b show the temperature dependence of the slow and the fast decay time (in red) respectively. The lifetimes have been measured at a $\lambda_{det} = 1220$ nm. The component of the PL intensity of the slow and the fast decay time is shown in black for being compared with the lifetimes. It is striking to observe that both the slow and the fast components decrease proportionally with the PL intensity as the temperature increases. This is a clear evidence that non radiative phenomena occur and quench the luminescence. Figure 3.27.a shows the sublinear behavior of the IR PL intens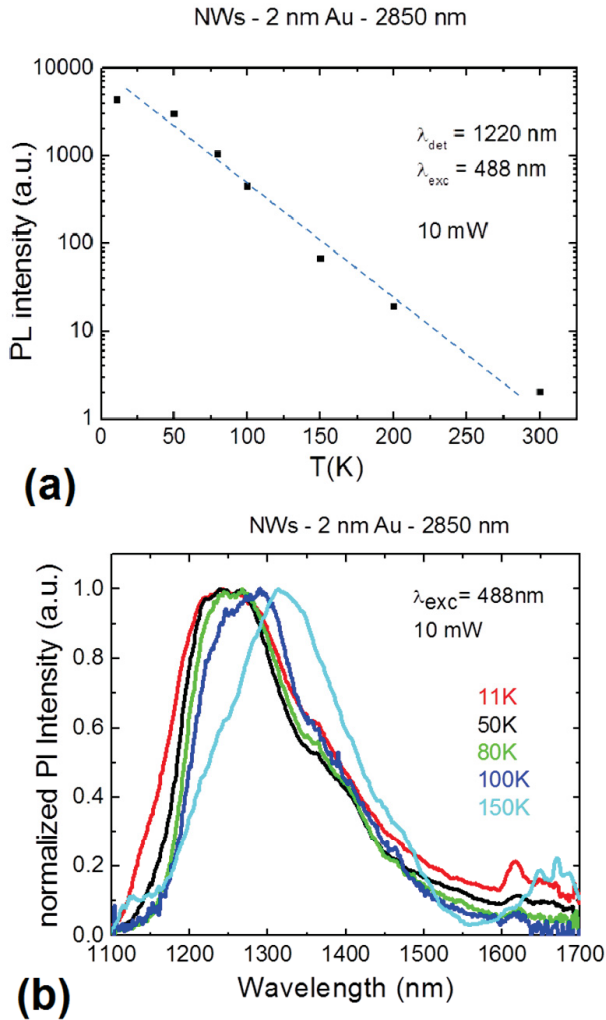ity, measured at $\lambda = 1220$ nm, as a function of the photon flux. In order to understand the reasons for this behavior the data have been be analyzed in detail. The data in fig. 3.27.a can be described by solving the rate equation which accounts for the excitation and de-excitation processes of excitons in the Si/Ge/Si emitting center:

$$\frac{dN^*}{dt} = \sigma\phi(N - N^*) - \frac{N^*}{\tau} \tag{3.14}$$

where N is the total amount of excitable emitting centers, N* is the excited emitting center population, σ is the cross section for excitation, ϕ is the photon flux impinging on the sample, and τ is the lifetime of the excited state taking into account both radiative and nonradiative processes. At steady state, solving eq. 3.14 and taking into account that the PL intensity is proportional to N^*/τ_{rad} , where τ_{rad} is the radiative lifetime of the emitting center, we obtain:

$$\frac{I}{I_{max}} = \frac{\sigma\tau\phi}{\sigma\tau\phi + 1} \tag{3.15}$$

with $I_{max} \propto N/\tau_{rad}$. From a fit to the data of fig. 3.27.a using eq. 3.15 we obtain a $\sigma\tau$ value of 5.3×10^{-22} $cm^2 s$. In order to
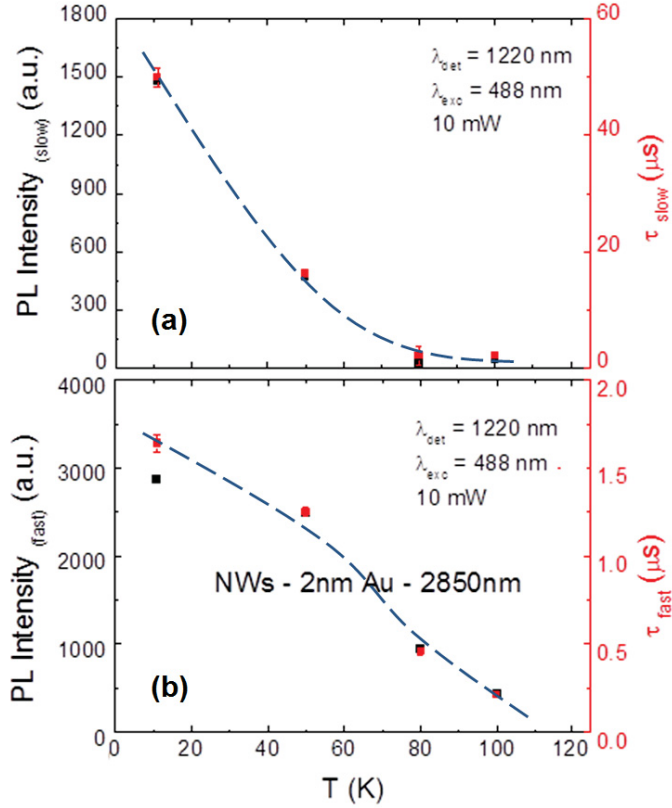
Figure 3.26: *(a) Temperature dependence of the slow lifetime compared to the slow component of the PL intensity. (b) Temperature dependence of the fast lifetime compared to the fast component of the PL intensity. All measurements have been performed at a pump power of 10 mW, excitation at 488 nm and detection wavelength of 1220 nm, on a Si/Ge MQW NWs sample of length equal to 2800 nm.*

obtain the value of the excitation cross section σ, a study of both the fast and the slow lifetime as a function of the pump power has been conducted (see fig. 3.27.b). As the photon flux increases, both the fast and the slow lifetimes decrease, due to non radiative phenomena, e.g. the Auger effect. However, it is important to understand the contribution of the fast and the slow channel to the PL intensity. This has been measured, by fitting each PL lifetime decay with a double exponential with its relative pre-factors A_{slow} and A_{fast}. The ratio $A_{slow}/(A_{fast} + A_{slow})$ vs the photon flux is shown in fig. 3.27.c. At high photon fluxes, the contribution of the slow component is negligible and we can consider a mean lifetime of 0.5 μs. Hence, the measured excitation cross section is $\sigma = 1\times 10^{-15} cm^2$. This value is compatible with the excitation cross section of excitons, excluding an origin of the IR PL due to defects.
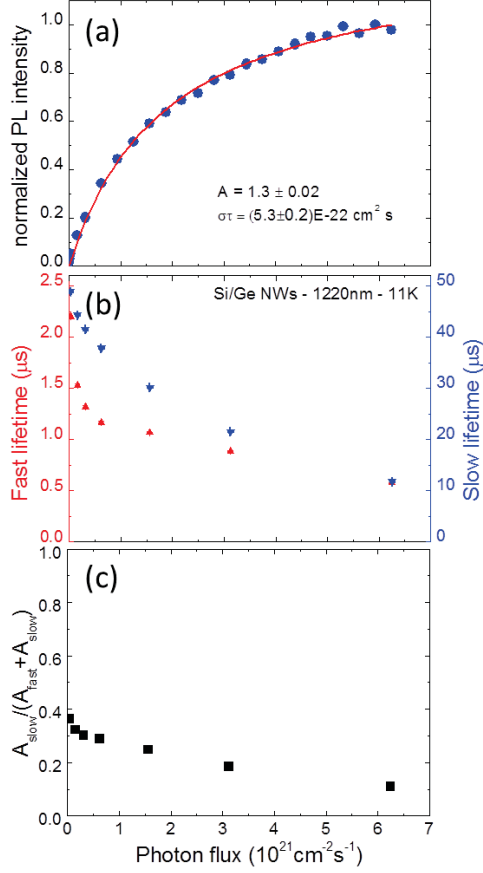
Figure 3.27: *(a) Sublinear behavior of the IR PL intensity, measured at $\lambda = 1220$ nm, as a function of the photon flux. (b) Fast lifetime and slow lifetime as a function of the photon flux. (c) Ratio $A_{slow}/A_{fast} + A_{slow}$ as a function of the photon flux. All measurement are performed at 11 K under a 488 nm excitation wavelength, and a detection wavelength of 1220 nm.*

Conclusions

In conclusion, it has been demonstrated that metal-assisted etching processes can be used to produce ultrathin Si NWs exhibiting efficient RT luminescence due to quantum confinement effects. These NWs can be electrically excited and a prototype light emitting device has been demonstrated. It is noteworthy that these NWs have highly controlled and reproducible structural properties also over very large areas, up to the wafer scale, demonstrating the potential applicability of this technique also in an industrial environment. In addition they have an electrically active dopant concentration simply determined by the doping of the etched substrate. Changes in the concentration or in the nature of the dopant, or even the formation of p–n junctions inside the NWs, can be very simply and effectively accomplished by a proper change of the characteristics of the starting substrate. The potential advantages related to the ease of doping of Si NWs synthesized by metal-assisted etching are enormous, since, on the other hand, it is well known that the doping of NWs grown by techniques based on the VLS mechanism presents important problems, both for in situ and ex situ approaches, such as incomplete dopant activation, dopant surface segregation, or even Si NW structural damage in the case of ion implantation. It is also remarkable that there is no metal inclusion inside the NWs, which is one of the main factors which makes application in optical and electrical devices of NWs grown by metal-catalyzed VLS techniques difficult. Metal particles are indeed trapped at the bottom of the etched regions. Since the whole process is performed at room temperature, diffusion inside the wires is negligible and metal atoms can be effectively removed at the end by an appropriate selective etching. Then, the analysis of the PL properties as a function of aging, temperature and pump power of Si NWs prepared by metal-assisted wet etching strongly supports the idea that photon emission is due to quantum confinement effects. Moreover, the peculiar high surface reactivity exhibited by the wires, and its influence on the PL properties of the system, makes this material potentially interesting also for sensor fabrication. Finally, it becomes important to compare performances and perspectives of Si NWs with those of Si NCs, which have been generally recognized

as the most promising Si-based materials for applications in light sources. While Si NWs show strong similarities to Si NCs from several points of view, they have in fact much stronger potentials. Si NWs have the great advantage over Si NCs of being a continuous 1D Si system. Indeed, it is well known that tunneling phenomena are the main conduction mechanism in Si NCs embedded in SiO_2. This determines high operating voltages, which could probably prevent any practical device application of Si NCs; furthermore, oxide breakdown phenomena constitute the main failure mechanism for devices based on Si NCs. In contrast, Si NWs can be fabricated in very dense arrays, are very good conductors and we have demonstrated light emitting devices operating at low voltages (2 V). On the other side, by studying and understanding the mechanisms of emission of Si NWs, it has been possible to increase the complexity of this system by inserting Ge dots inside each Si NW. In this way the photoluminescence properties of Si/Ge MQW NWs have been studied, and a luminescence due to exciton recombination in the Ge disks has been demonstrated. Finally, concerning Raman experiments on Si NWs , we demonstrated that a forest of vertically aligned densely arranged Si NWs with a 2D fractal geometry shows a high light trapping efficiency and highly directional Raman emission field due to multiple scattering phenomena. Our findings give the first strong experimental evidence for a coherent Raman backscattering phenomenon occurring in strongly scattering materials, paving the way for the optimization of Si NWs technology towards Raman gain and lasing in the visible range.

Chapter 4

Optical trapping of Si NWs

Abstract

Optical trapping [153, 154, 155] (OT) of nanostructures has acquired tremendous momentum in the past few years. Manipulating nanoparticles with OT is generally difficult because radiation forces scale approximately with particle volume [155, 156] and thermal fluctuations can easily overwhelm trapping forces at the nanoscale [155]. However semiconductor and optical nonlinear [157, 158] nanowires, carbon nanotubes, [159] polymer nanofibers, [160] graphene, [161] quantum dots, [162] and plasmonic nanoparticles [163] have now been stably trapped thanks either to their highly anisotropic geometry [164, 165, 166, 167, 157, 158, 159, 160, 161] or to their intrinsic resonant behavior [162, 163]. They have been manipulated to build nanoassemblies, [164, 165] as well as to accurately measure forces with a resolution at the level of femto-Newtons crucial for photonic force microscopy applications [157, 159, 161, 168, 169]. Nanotools [168] have been specifically designed in order to combine the outstanding force-sensing capabilities of OT with increased nanometric precision and bridge the gap between micro and nanoscale in fluidic environments [169]. Furthermore the integration of OT with Raman spectroscopy allowed for ultrasensitive chemical-physical analysis of trapped particles [161, 170, 171]. In this context, the role of size-scaling is crucial for understand-

ing the interplay between optical forces and hydrodynamic inter-
actions [172] that change dramatically with size, hence much af-
fecting both force-sensing and spatial resolution in precision appli-
cations [165, 157, 159, 168, 169]. Here we investigate how optical
trapping and Brownian motion of very thin (7±2 nm diameter)
Si NWs are dependent on size. We show how their length is the
key parameter that regulates forces, torques, and hydrodynamics.
We fully characterize the three-dimensional translational and an-
gular Brownian motion, measure root-mean-square displacements
and show the different size-scaling due to the interplay between ra-
diation forces defining the trapping potential and hydrodynamics.
Finally, we compare our findings with a full electromagnetic theory
of optical trapping of SiNWs, showing good agreement when taking
into account aberration from the coverslip-water interface.

4.1   Optical tweezers

It has been known since the XVII century that light can exert forces.
But it was only with the invention of the laser in the 1960 [173] that
it became possible to exploit these forces. In 1970 a seminal pa-
per from Ashkin [174] demonstrated that it was possible to use the
forces of radiation pressure to significantly affect the dynamics of
transparent micrometer neutral particles. In 1986, Ashkin et al. re-
ported the first observation of what is now commonly referred to as
an optical trap [153]: a tightly focused light beam capable of hold-
ing microscopic particles in three dimensions. It is well known from
quantum mechanics that light carries a momentum: for a photon
a wavelength λ the associated momentum is $p = h/\lambda$, where h is
the Plank constant. For this reason, whenever an atom emits or ab-
sorbs a photon, its momentum changes according to Newton's laws.
Similarly, an object will experience a force whenever a propagating
light beam is refracted or reflected by its surface. However, in most
situations this force is so much smaller than other forces acting on
macroscopic objects that there is no noticeable effect and, there-
fore, can be neglected. Objects, for which this radiation pressure
exerted by light starts to be significant, weigh less than $1\mu g$ and
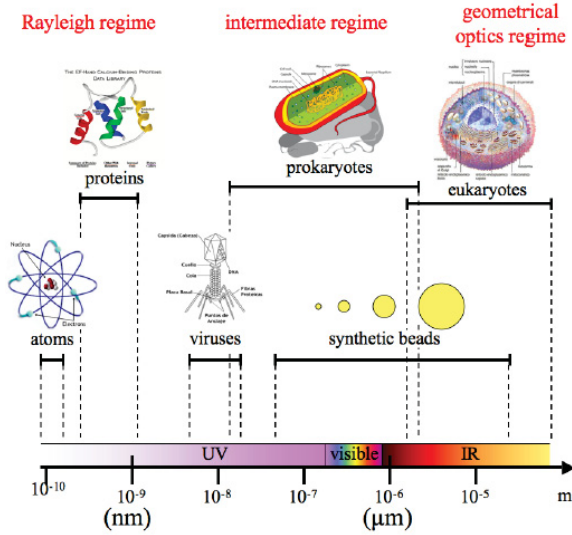
Figure 4.1: *Trapping regimes and typical objects that are trapped in optical manipulation experiments.*

their size is below 10 μm. A focused laser beam acts as an attractive potential well for a particle. The equilibrium position lies near - but not exactly at - the focus. When the object is displaced from this equilibrium position, it experiences an attractive force towards it. This restoring force is in first approximation proportional to the displacement. In other words, optical tweezers force can generally be described by Hooke's law:

$$F_x = -k_x(x - x_0) \tag{4.1}$$

where x is the position of the particle, x_0 is the focus position and k_x is the spring constant along x of the optical trap, usually referred as *trap stiffness*. In fact, optical tweezers create a tridimensional potential well that can be approximated by three independent harmonic oscillators, one for each of the x, y, and z directions. If the optics are well aligned, the x and y spring constants will be roughly the same, while the z spring constant, instead, is typically smaller by a factor of $\approx 5 \div 10$. In optical trapping experiments, light force is provided by a laser beam and objects ranging from tens of nanometers to tens of microns, such as cells, micron-sized dielectric

123

particles or nano-sized metallica beads, are manipulated. Considering the ratio between the characteristic dimension L of the object and the wavelength λ of the trapping light, three different trapping regimes can be deinfed:

1. *Rayleigh regime*, when $L \ll \lambda$;

2. an *intermediate regime*, when L is comparable to λ;

3. *geometrical optics regime*, when $L \gg \lambda$.

In fig. 4.1 an overview of the kind of objects belonging to each of these regimes is presented, assuming that the trapping wavelength is in the visible or NIR spectral region. In any of these regimes, the electromagnetic equations can be solved to evaluate the force acting on the object. However, this can be a cumbersome task. For the Rayleigh regime and geometrical optics regime approximated models have been developed, which allows one to going insight into the physics of optical trapping. However, most of the objects that are normally trapped in optical manipulation experiments fall in the *intermediate regime region*, where the Rayleigh or geometrical optics approximation cannot be used. In particular, the probes we use in this thesis lie in the intermediate regime: they typically are Si NWs with diameter of a few nanometers and length between 1 μm and 5 μm. In the following we will see more in detail the optical forces in the Rayleigh regime and in the geometrical optics regime.

4.1.1 Rayleigh regime for a bead

A macroscopic particle with dimensions much smaller than the wavelength λ of the illuminating electromagnetic field is well described by a dipole, i.e. by two bounded oppositely charged particles with masses m_1 and m_2, placed respectively at r_1 and r_2, such that $||s|| = ||r_1 - r_2|| \ll \lambda$. The equation of motion for the two particles follows the Lorentz law:

$$
\begin{cases}
m_1 \frac{d^2 r_1}{dt^2} = q \left[\mathbf{E}(\mathbf{r}_{1,t}) + \frac{dr_1}{dt} \times \mathbf{B}(\mathbf{r}_1, t) \right] - \nabla U(\mathbf{r}_1, t) \\
m_2 \frac{d^2 r_2}{dt^2} = q \left[\mathbf{E}(\mathbf{r}_{2,t}) + \frac{dr_2}{dt} \times \mathbf{B}(\mathbf{r}_2, t) \right] + \nabla U(\mathbf{r}_2, t)
\end{cases}
\tag{4.2}
$$

where the binding potential U has been included in the equation. The two particles constitute a two body problem which is most conveniently solved by introducing the center of mass coordinate

$$\mathbf{r} = \frac{m_1}{m_1 + m_2}\mathbf{r}_1 + \frac{m_2}{m_1 + m_2}\mathbf{r}_2 \tag{4.3}$$

and the dipole moment $\mathbf{p} = q\mathbf{s}$. Combining this notation with eq. 4.2, the mechanical force exerted by the electromagnetic field on the dipole is:

$$\mathbf{F}(\mathbf{r}, t) = \mathbf{p} \cdot \nabla \mathbf{E}(\mathbf{r}, t) + \frac{dp}{dt} \times \mathbf{B}(\mathbf{r}, t) + \frac{d^2\mathbf{p}}{dt^2} \times \mathbf{p} \cdot \nabla \mathbf{B}(\mathbf{r}, t) \tag{4.4}$$

where, using the dipole approximation $||s|| \ll \lambda$, the Taylor expansion of the electric and magnetic fields at the positions of the two particles can be truncated at the first order. The third term of the right hand side is usually much smaller than the other two terms and, therefore, can be neglected:

$$\mathbf{F}(\mathbf{r}, t) = \mathbf{p} \cdot \nabla \mathbf{E}(\mathbf{r}, t) + \frac{d\mathbf{p}}{dt} \times \mathbf{B}(\mathbf{r}, t) \tag{4.5}$$

It is interesting to note that the field appearing in this equation corresponds to the incoming one, i.e. the dipole is assumed not to change the fields, which is very convenient from the computational point of view. If the dipole is illuminated by an arbitrary monochromatic electromagnetic wave with angular frequency ω,

$$\begin{cases} \mathbf{E}(\mathbf{r}, t) = Re\left[\mathbf{E}(\mathbf{r})e^{-j\omega t}\right] \\ \mathbf{B}(\mathbf{r}, t) = Re\left[\mathbf{B}(\mathbf{r})e^{-j\omega t}\right] \end{cases} \tag{4.6}$$

its momentum is:

$$\mathbf{p}(t) = Re\left[\mathbf{p}e^{-j\omega t}\right] \tag{4.7}$$

This means that the fields and dipole moment can be represented by their complex amplitudes $\mathbf{E}(\mathbf{r})$, $\mathbf{B}(\mathbf{r})$ and $\mathbf{p}$. Assuming that the particle has no static dipole moment, to first order, the induced one
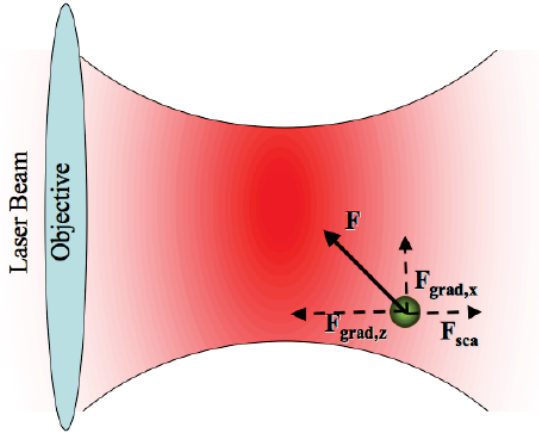
Figure 4.2: *Scattering and gradient forces in the Rayleigh regime.*

is proportional to the electric field at the position of the particle $\mathbf{r} = \mathbf{r}_0$

$$\mathbf{p} = \alpha(\omega)\mathbf{E}(r_0) \tag{4.8}$$

where α denotes the polarizability of the particle. Taking a time average, eq 4.5 becomes:

$$< \mathbf{F}(r) >= \frac{1}{2}Re\left[\mathbf{p}^* \cdot \nabla E - i\omega\mathbf{p}^* \times \mathbf{B}\right] \tag{4.9}$$

or, replacing the dipole moment by its expression in eq. 4.8 and splitting the polarizability into its real and imaginary parts, after some rearrangement:

$$< \mathbf{F}(r) >= \{\frac{Re[\alpha]}{2}\nabla\mathbf{E}^2 + \frac{\omega Im[\alpha]}{c^2\epsilon_0\epsilon_r}\mathbf{S} \tag{4.10}$$

where ϵ_0 is the permittivity of vacuum, and ϵ_r the dimensionless relative permittivity of the surrounding medium.

Therefore, as already recognized by Ashkin in 1970 [174], the mechanical force can be split into two terms, which are illustrated in fig. 4.2: the first is denoted as *gradient force* and the second one as *scattering force*. For an ideal lossless particle there is no mo-

126

mentum transfer from the radiation field to the particle and the scattering force is zero. Polarizable particles are accelerated by the gradient force towards extrema of the radiation field. Therefore, a tightly focused laser beam can trap a particle in all dimensions at its focus. However, the scattering force pushes real particles in the propagation direction and, if the focus of the trapping laser is not tight enough, the particles may be pushed out of the focus.

4.1.2   Ray optics regime for a bead

When the dimension of the object with which the light waves interact is much larger than its wavelength λ, the geometrical optics description applies. In geometrical optics a light wave is represented as a ray directed along the propagation direction, and its intensity is determined by the number of photons passing through a given area per unit time. The magnitude of the momentum of a single photon is given by $||\mathbf{p}|| = h/\lambda$, and the momentum flux of a light beam of intensity given by the Poynting vector $\mathbf{S}$ is:

$$d\left(\frac{d\mathbf{P}}{dt}\right) = \frac{n_m}{c}\mathbf{S}dS \qquad (4.11)$$

where n_m is the index of refraction of the medium surrounding the object, c is the speed of light in vacuum and dS is an element of area normal to $\mathbf{S}$. Therefore, in principle it is possible to directly calculate the force on a given area due to the light momentum flux through it. Since the force on a dielectric object, the total force on it is due to the difference between the momentum flux entering the object and the one leaving it:

$$\mathbf{F} = \frac{n_m}{c}\int_S (\mathbf{S}_{in} - \mathbf{S}_{out})dS \qquad (4.12)$$

In optical manipulation experiments the object is pushed by the reflection of light from its surface. Radiation forces due to refraction, instead, can be used to pull a transparent object, as it is qualitatively shown in fig. 4.3 *[175]*. Each ray is refracted at the object surface so that the direction of propagation changes according to Snell's law which states that
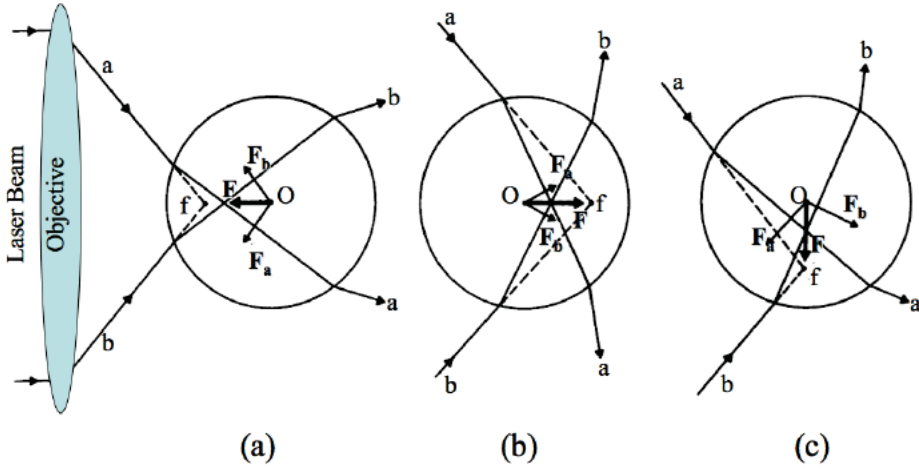
Figure 4.3: *Forces in the geometrical optics regime. Qualitative view of the trapping of different spheres. The refraction of a typical pair of rays a and b of the trapping beam gives forces F_a and F_b whose vector sum F is always restoring for axial and transverse displacements of the sphere from the trap focus f [175].*

$$n_m sin\left(\theta_1\right) = n_p sin\left(\theta_2\right) \qquad (4.13)$$

where n_m is the index of refraction of the medium surrounding the particle and n_p is the index of refraction of the bead. Here θ_1 is the angle of incidence of the ray with respect to a line perpendicular to the surface of the particle and θ_2 is the angle with respect to the same line at which the ray propagates within it. Figure 4.4.a illustrates the multiple reflections and refractions that a light ray undergoes when it impinges on a spherical object [175]. Snell's law indicates that the change in the light direction at the interface of the bead with its surroundings depends strongly on the index of refraction of each medium. The change in direction of the light due to refraction is all contained within the integral in eq. 4.12. Since the bead changes the momentum of the light, an equal and opposite change in its momentum occurs. The resultant force of the light on the bead due to refraction, also called *gradient force*, is always in the direction of the focus of the light. Therefore, in
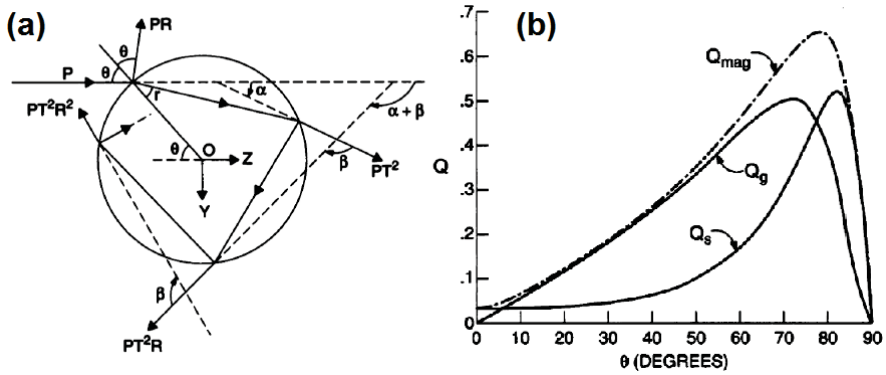
Figure 4.4: *Scattering of a ray on a sphere. Scattering of a single incident ray of power P by a dielectric sphere, showing the reflected ray PR and infinite set of refracted rays PT^2R^n [175].*

absence of other forces, the sphere is attracted to the focal point of the light. In order to trap, the attractive force due to refraction of the light at the surface of the particle must be sufficient to overcome any other forces acting to push the bead out of the trap, such as the force due to reflection at its surface (*scattering force*). The values of these forces, as a function of the incidence angle, are shown in fig. 4.4.b. Following the approach of Ashkin [153], it is possible to derive various results in the geometrical optics regime. In particular we can see which are the theoretical limits to the trapping forces. The force that can be extracted from a beam of power $F = (n_m P/c) \cdot Q$, where Q is a dimensionless factor depending on the geometry. When the optical beam is perfectly reflected in the incident direction the maximum $Q = 2$ is achieved; therefore, the maximum force that can be exerted in water by a 1 mW beam is $F_{MAX} = 8.9$ pN.

4.1.3 Nanowire hydrodynamics and correlation function analysis

For rigid rod-like structures (such as our SiNWs dispersed in water) of length L and diameter d, the viscous drag is characterized by anisotropic hydrodynamic damping (see fig. 4.5.a) [176]. Because
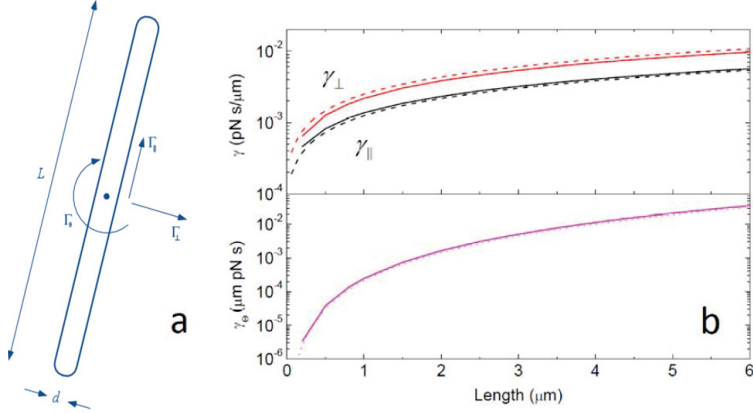
Figure 4.5: *(a) Different viscous damping forces for a cylinder. (b) Scaling with nanowire length L of the damping coefficients $\gamma_\perp$, $\gamma_\parallel$ and γ_Θ calculated for our experimental conditions with (solid lines) and without (dashed lines) end-effect corrections δ_i.*

of symmetry, the translational and rotational viscous damping coefficients are [177, 178, 159]:

$$\gamma_\perp = \frac{4\pi\eta L}{ln(p) + \delta_\perp}, \quad \gamma_\parallel = \frac{2\pi\eta L}{ln(p) + \delta_\parallel}, \quad \gamma_\theta = \frac{\pi\eta L^3}{3\left[ln(p) + \delta_\parallel\right]} \qquad (4.14)$$

where $\gamma_\perp$ and $\gamma_\parallel$ are the translational damping coefficients, transverse and parallel to the main axis respectively, γ_Θ is the rotational mobility about the center-of-mass, L is the length of the nanostructure, $p = L/d$ is the length-to-diameter ratio, η is the water dynamical viscosity, and δ_i are end corrections (calculated by Broersma in ref. as polynomial of $ln(2p^{-1})$). The behavior of these coefficients vs the length of the NW is shown in fig. 4.5.b. Si NWs align with the propagation axis and positional and angular displacements occur in the small angle limit, $\theta \ll 1$. Thus the tracking signals are the combination of positional and angular variables [159, 179, 180]: $S_x \propto X + a\Theta_x$, $S_y \propto Y + b\Theta_y$, $S_z \propto Z$. Where X, Y, and Z are the center-of-mass coordinates, a, b, c calibration constants, and $\Theta_x = \theta sin\phi$ and $\Theta_y = \theta cos\phi$ are the correlated angular projections on the x and y axis, respectively. All these coordinates are treated

as stochastic variables. Now we consider the transverse signals autocorrelation (ACF) and crosscorrelation (CCF) functions [159]:

$$C_{xx}(\tau) = < S_x(t)S_x(t+\tau) > = < X(t)X(t+\tau) > + a^2 < \Theta_x(t)\Theta_x(t+\tau) > \tag{4.15}$$

$$C_{yy}(\tau) = < S_y(t)S_y(t+\tau) > = < Y(t)Y(t+\tau) > + b^2 < \Theta_y(t)\Theta_y(t+\tau) > \tag{4.16}$$

$$C_{xy}(\tau) = ab < \Theta_x(t)\Theta_y(t+\tau) > \tag{4.17}$$

Thus ACFs contain combined information on translational and rotational variables and decay as double exponentials [159, 179, 180]. Instead CCF separates the angular variables only [159] and decays as a single exponential with different relaxation frequencies for positive or negative lag times related to Ω_i (i = x, y). In our experiments we get the measured values of angular relaxation frequencies from both ACFs and CCF. Figure 4.6 shows an exemplar comparison between values of Ω_x extracted from ACF (red) and CCF (blue) for data obtained on individual trapped Si NWs. The agreement between the two procedures is well within the error bars, hence only the data obtained from ACFs will be shown. To calculate the radiation force [156] and torque [166] on trapped Si NWs we use the full scattering theory in the framework of the transition matrix (T-matrix) approach [181]. This approach is quite general as it applies to particles of any size, symmetry and refractive index for any choice of the wavelength.[181] Our starting point is the calculation of the field configuration in the focal region of a high numerical aperture (NA) objective lens in absence of any particle, using the procedure originally formulated by Richards and Wolf [182]. The resulting field is considered as the field incident on the particles, and the radiation force and torque exerted on any particle within the region is calculated by resorting to momentum conservation for the combined system of field and particles. As a result the optical force and torque exerted on a particle are given by the integrals [166, 156]:
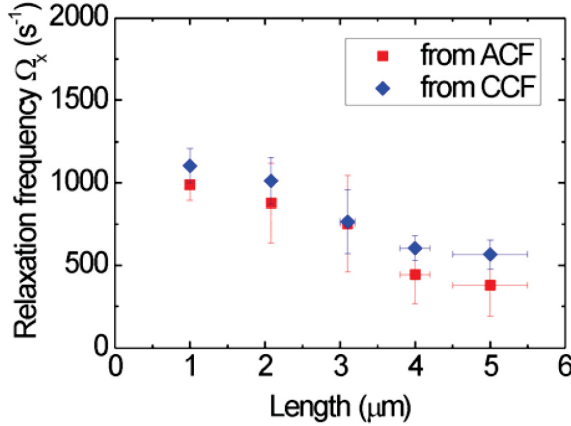
Figure 4.6: *Comparison between angular relaxation frequencies obtained from ACF and CCF analysis. The consistency is good within the error bars that represent the standard deviation obtained from several measurements in each Si NW sample.*

$$\mathbf{F}_{rad} = r^2 \int_{\Omega} \hat{\mathbf{r}} \cdot < T_M > d\Omega \qquad (4.18)$$

$$\mathbf{M}_{rad} = -r^3 \int_{\Omega} \hat{\mathbf{r}} \cdot < T_M > \times \hat{\mathbf{r}} d\Omega \qquad (4.19)$$

where the integration is over the full solid angle, r is the radius of a large (possibly infinite) sphere surrounding the particle centre, and $< T_M >$ is the time averaged Maxwell stress tensor in the form of Minkowski [183]:

$$< T_M > = \frac{1}{8\pi} Re \left[n^2 \mathbf{E} \otimes \mathbf{E}^* + \mathbf{B} \otimes \mathbf{B}^* - \frac{1}{2} (n^2 |\mathbf{E}|^2 + |\mathbf{B}|^2) I \right]$$
$$(4.20)$$

where $\otimes$ denotes dyadic product, I is the unit dyadic and n is the refractive index of the surrounding medium. Expanding the incident field in a series of vector spherical harmonics with (known) amplitudes W^p_{Ilm}, the scattered field can be expanded on the same basis with amplitudes $A^{p'}_{l'm'}$. The relation between the two amplitudes
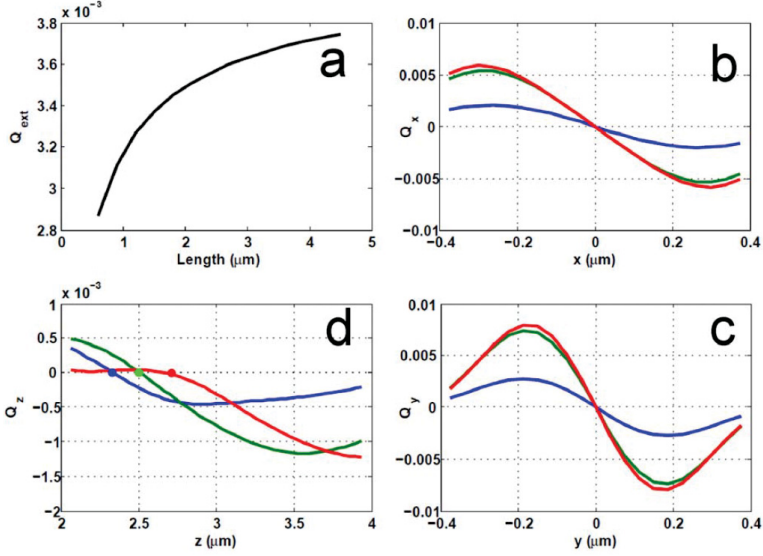
Figure 4.7: *(a) Extinction efficiency Q_{ext} for a Si NW modeled as a linear chain of spheres with $D = 30$ nm. (b-d) Optical trapping efficiency Q_x, Q_y, and Q_z for three different Si NWs modeled with an increasing number of spheres: 20 spheres, $L = 0.6$ μm (blue line); 80 spheres, $L=2.4$ μm (green line); 110 spheres, $L=3.3$ μm (red line). For the transverse optical forces (b,c) the equilibrium position of the Si NW in the trap is always found at the center of the laser spot. Instead in the axial direction (d) the equilibrium position is shifted from the nominal unaberrated focal point (set to zero) because of radiation pressure and aberration.*

is given by $A^{p'}_{l'm'} = \sum_{plm} S^{p'p}_{l'm'lm} W^{p}_{I\,lm}$, where $S^{p'p}_{l'm'lm}$ is the T-matrix of the particle. In this framework, several kinds of non-spherical particles can be modeled as aggregates of spherical scatterers with size below the radiation wavelength. Each element of the T-matrix is independent both on the direction of propagation and on the polarization of the incident field [181]. Thus they do not change when the incident field is a superposition of plane waves with different direction of propagation, i.e., for the description of a focused laser beam in the angular spectrum representation [184]. In our calculations, the Si NWs are modeled as chains of spheres, with diameter (D = 30 nm) much smaller than the wavelength. The chain length,

L, corresponds to the Si NW one. Note that the size (30 nm) and number of subunits composing the model linear chains are limited by the memory demand of the computing facilities. In fact, the calculation of the transition matrix for a N-sphere linear chain, requires the inversion of a matrix of order $2N \times l_T(l_T+2)$, where l_T is the l-value at which the multipole expansion of the electromagnetic fields is truncated [181]. To ensure the numerical stability of the results, that depends on the size of both the subunits and the length of the linear chain, we check each linear cluster configuration for the existence of an l-value l_M for which, if $l_T > l_M$, the calculated values (extinction cross-section, optical force and torque constants) do not change. For the longest linear chain of 4.5 µm we have 150 subunits and we truncate the multipole expansion at $l_M = 5$. The transition matrix then contains (10500×10500) complex elements. The calculation of optical forces and torques was performed on a HP/Itanum 2 cluster, requiring about 7 h of CPU time for every configuration. In fig. 4.7.a we show the scaling with length of the extinction efficiency for a linear clusters of N spheres with a random orientation in space, defined as [181]:

$$Q_{ext} = \frac{< C_{ext} >}{C_T} \tag{4.21}$$

where $< C_{ext} >$ is the averaged extinction cross section of the linear chain, and $C_T = N\pi r^2$ is the total geometrical cross section. We calculate for each model Si NW the radiation force $\mathbf{F}_{rad}(\mathbf{R})$ and torque $\mathbf{M}_{rad}(\mathbf{R})$, the argument $\mathbf{R}$ denoting the position of the center of mass of the linear cluster of spheres. The trapping occurs on the optical axis where all the components of force and torque vanish with a negative derivative. In the vicinity of the trapping point $R_0 = (0, 0, z_0)$ the components of $\mathbf{F}_{rad}(\mathbf{R})$ can be approximated by $F_{rad_x}(x, 0, z_0) = -k_x x$, $F_{rad_y}(0, y, z_0) = -k_y y$, $F_{rad_z}(0, 0, z) = -k_z(z - z_0)$. Where k_x, k_y, and k_z are the force constants. Thus we first determine the trapping position and equilibrium orientation of the Si NW, and then calculate the force constants around this equilibrium state. The results of typical calculations of the optical force efficiencies, $Q_\xi = R_{rad\xi}\frac{c}{nP}$, $\xi = x, y, z$ exerted on exemplar trapped Si NWs with L =0.6, 2.4, 3.3 µm and D = 0.03 µm are displayed in fig. 4.7.b,c,d. For the transverse

optical forces the equilibrium position of the SiNW in the trap is always found at the center of the laser spot. Instead in the axial direction the equilibrium position is shifted from the nominal unaberrated focal point (set to z = 0) because of radiation pressure and aberration.

4.2 Experimental setup

Si NWs were prepared by the wet-etching technique discussed in details in chapter 2. For this experiment we prepared five samples in which the Si NWs length, L, is respectively 1.00±0.05, 2.08±0.04, 3.1±0.1, 4.0±0.2, and 5.0±0.5 µm, measured from scanning electron microscopy (field-emission SEM Zeiss Supra 25) analysis of the as-grown samples. Typical cross-section SEM images of different length of Si NWs obtained by varying the etching time have been shown in fig. 2.6 of chap. 2 (pag. 67). The images display a dense and uniform distribution of NWs with very small diameters. A mean diameter of 7 ± 2 nm is obtained from Raman spectroscopy analysis. For optical trapping experiments, Si NWs are mechanically scratched from the substrate and then stably dispersed by sonication in water solution added with sodium dodecyl sulfate (SDS) (see fig. 4.8.a), as shown in fig. 4.8.b. Although Si NWs can be dispersed in water without the aid of surfactants, we found that using SDS improves the temporal stability of the dispersion toward aggregation and minimize the sticking to glass surfaces. A few tens of microliters are then placed in a sample chamber attached to a piezo-stage with 1 nm resolution. Optical trapping is achieved [159, 161] by focusing a 830 nm laser beam (from a laser diode Sanyo DL 8142-201, 150 mW nominal power) through a 100 oil immersion objective (NA = 1.3) on an inverted microscope (see fig. 4.8.c and 4.8.d for a sketch of the setup and the geometry). The laser power available at the sample is about 20 mW and was kept constant during the optical force measurements. Optically trapped Si NWs are imaged with a CCD camera (see fig. 4.9). Figure 4.9 shows a optical microscopy image of a 3 μm long Si NW optically trapped in the focal region of the NIR laser (in red), where a slow precession motion of the NW is visible. Then,
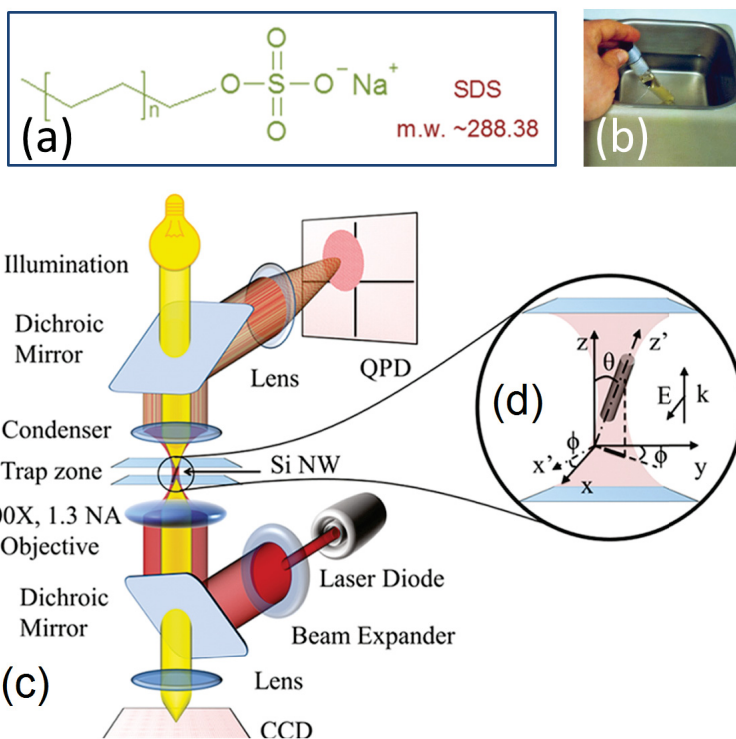
Figure 4.8: *Sketch of the optical tweezers setup: a NIR laser beam (830 nm) is focused by a 1.3 NA oil immersion microscope objective. Si NWs are trapped in a water dispersion placed in a sample chamber. The scattered light from the trapped particle is detected by a QPD through a collection optics yielding electrical signals S_x, S_y, and S_z proportional to the particle translational and angular displacements. (inset) Description of the geometry in the trap with relevant coordinates and angles for the characterization of forces and hydrodynamic mobilities of trapped nanowires.*

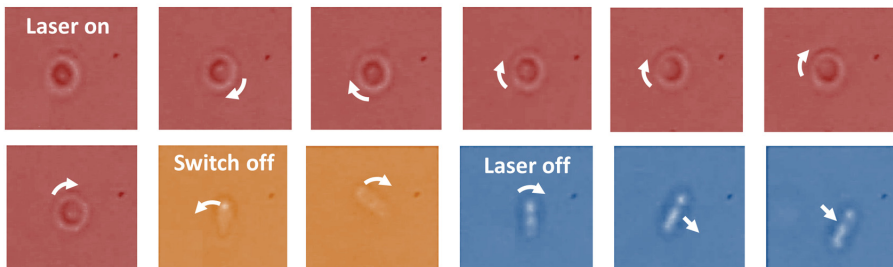Figure 4.9: *(red) Optical microscopy image of a 3 μm long SiNW optically trapped in the focal region of the NIR laser. A slow precession motion of the NW is visible. (orange) Gradually switching the laser off the NW starts to misalign from the the trap axis. (blue) As the laser is switched off, the free brownian motion of the NW starts again, and its center of mass moves far from the optical trap. Note that these diffraction-limited CCD images result from the interference between scattered and unscattered illumination light from the nanowire yielding a change from brighter to darker region when propagating along the nanowire length.*

gradually switching the laser off (in orange) the NW starts to misalign from the the trap axis. Finally, as the laser is switched off, the free brownian motion of the NW starts again, and its center of mass moves far from the optical trap (in blue). This enables inspection of the individual trapped Si NW length that is always checked to be consistent with SEM measurements for each sample. Force measurements are performed always at a distance of about 15 μm from the coverslip inside the sample chamber in order to minimize the effect of the glass surface. Positional and angular displacements of the trapped SiNWs are measured by back focal plane (BFP) interferometry [185], where the interference pattern between forward scattered and unscattered light in the microscope condenser BFP is imaged onto a four quadrant photodiode, QPD (see a sketch in fig. 4.10). This is oriented with the polarization (x-y) axis of the laser beam in order to have sensitivity over polarization effects [167, 156]. The QPD outputs from each quadrant are then combined as pairwise sums (S_x, S_y) and four-quadrant sum (S_z). These tracking signals are thus acquired at 50 kHz sampling rate for 2 s (10^5 points). While for a spherical particle the QPD traces are proportional to
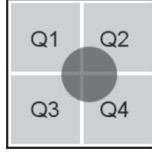
Figure 4.10: *A sketch of the four quadrant photodiode (QPD)*
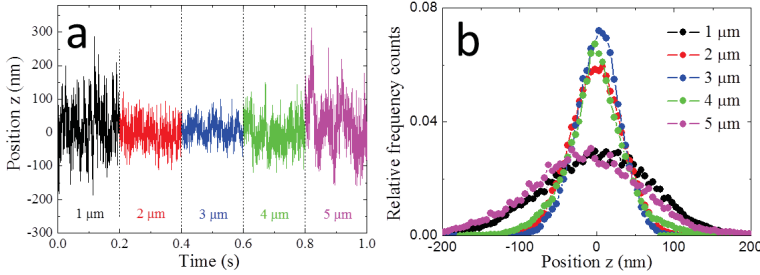
Figure 4.11: *(a) Calibrated tracking signals along the propagation (z-)axis and (b) relative frequency counts of the signals for individual trapped Si NWs of lengths L = 1 (black), 2 (red), 3 (blue), 4 (green), and 5 μm (magenta).*

its center-of-mass displacements, for trapped Si NWs they also contain information on angular displacements [179, 159, 161, 186]. In particular since radiation pressure aligns the Si NWs with the light propagation [166, 186, 187, 188] (z-)axis (see fig. 4.9, laser switched on), positional and angular displacements occur in the small polar angle limit (see geometry in fig. 4.8.d), $\vartheta \ll 1$, and the tracking signals are [159] $S_x \propto X + a\Theta_x$, $S_y \propto Y + b\Theta_y$, $S_z \propto Z$. X, Y, and Z are the center-of mass coordinates, a, b, and c are calibration constants, and $\Theta_x = \vartheta sin\phi$ and $\Theta_y = \vartheta cos\phi$ are the angular projections on the x- and y-axis, respectively (shown in fig. 4.8.d).

4.3   Tracking of trapped Si NWs

Figures 4.11.a and 4.11.b show typical (calibrated) tracking signals (S_z) and frequency counts for each recorded trace obtained by trapping individual Si NWs with different length in each sample. The analysis of these signals resulting from Brownian motion

138

in the trap is the key to get optical forces and torques in optical trapping experiments.[155, 185] In general, a colloidal particle in a fluid is subject to thermal fluctuations [189]. In the free-diffusive regime (mean-square displacement is linear with time) the motion is independent of inertia terms (mass, moment of inertia) and it is described by a Langevin equation [189] for each relevant dynamic variable (positional or angular). When a colloidal particle is confined by an external potential, for example, an optical trap, the fluid damps its motion as in the free-diffusive regime, but now the particle explores only a limited region in space [185]. Anisotropy largely affects the Brownian dynamics in the trap [167, 159, 161, 186]. Thus, in addition to translational coordinates X, Y, and Z, rotational variables, Θ_x and Θ_y, have to be considered for a correct calibration of optical forces and torques on Si NWs. Here we consider the Si NWs as a rigid rodlike structure with no bending motion activated. This is reasonable since even for such thin Si NWs the Young's modulus has been recently measured [190] to be about 100 GPa and the corresponding persistence length [191] for the thermal activation of bending is about 25 cm, that is much larger than the length of Si NWs explored in this work. Thus for rigid rodlike particles anisotropy yields different viscous damping, $\gamma_{||} = (2\pi\eta L)/(lnp + \delta_{||}))$, $\gamma_{\perp} = (4\pi\eta L)/(lnp + \delta_{\perp})$, for translations parallel and perpendicular to the SiNW main axis respectively, and $\gamma_{\Theta} = (\pi\eta L^3)/[3(lnp + \delta_{\vartheta})]$, for rotations, that are dependent on the Si NW length-to-diameter ratio, p = L/d, water dynamic viscosity, η, and end corrections δ_i (calculated [159, 177] as polynomial of $((ln2p)^{-1})$. The Brownian dynamics of a trapped SiNW is then well described by a set of uncoupled Langevin equations [159, 161]

$$\frac{d}{dt}X_i(t) = -\omega_i X_i(t) + \xi_i(t), \quad i = x, y, z \qquad (4.22)$$

$$\frac{d}{dt}\Theta_j(t) = -\Omega_j \Theta_j(t) + \xi_j(t) \quad j = x, y \qquad (4.23)$$

where $\omega_i = k_i/\gamma_i$ and $\Omega_j = k\Theta_j/\gamma_{\Theta}$ are relaxation frequencies, related to the force and torque constants and viscous damping components, while $\xi_i(t)$ are random noise sources. From eqs. 4.22 and 4.23, the autocorrelation functions (ACF) of the transverse tracking

139
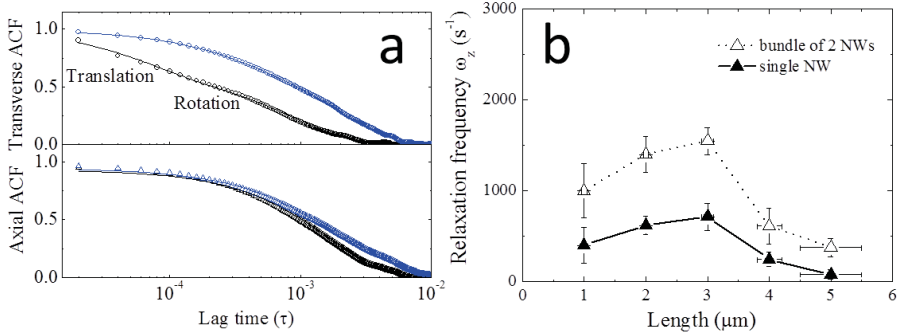
Figure 4.12: *(a) Exemplar transverse (top) and axial (bottom) auto-correlation functions (ACF) for two individual Si NWs of length L = 1 μm (black) and L = 3 μm (blue). The transverse ACF reveal both the translational and angular fluctuations of the Si NWs in the trap and are well fitted by a double exponential decay yielding the transverse force and torque constants. This is particularly evident at shorter lengths (see also). In contrast, axial ACF are well fitted with a single exponential decay with rate ω_z that yields the axial (z-)force constant. (b) Relaxation rates ω_z measured for different samples of SiNWs. For each length, we trapped about 20 different particles in each sample. Two sets of data points are distinguished corresponding to individual Si NWs and bundles of two Si NWs in the trap. The error bars on the length are extracted from the SEM images of the original samples, while the ones on the rates represents the standard deviation from the mean.*

signals $C_{ii}(\tau) = < S_i(t)S_i(t + \tau) >$ now contain combined information [186, 192] on center-of-mass and rotational fluctuations, and decay with lag time τ as a double exponential with positional and rotational relaxation frequencies ω_i, Ω_i (i = x, y). The ACF of the axial tracking signal, that is, the motion parallel to the propagation (z-)axis, is instead unaffected by the rotational motion and decays as a single exponential with relaxation frequency [159] ω_z. Figure 4.12.a shows ACF analysis for exemplary signals related to trapped SiNWs of 1 μm (black lines) and 3 μm (blue lines) length. The double exponential decay is clearly visible for the transverse signals, while it is absent for the axial ones as expected for a strongly aligned linear nanostructure (small angle approximation). For each sample, we trapped [160] different Si NWs, we then analyzed the
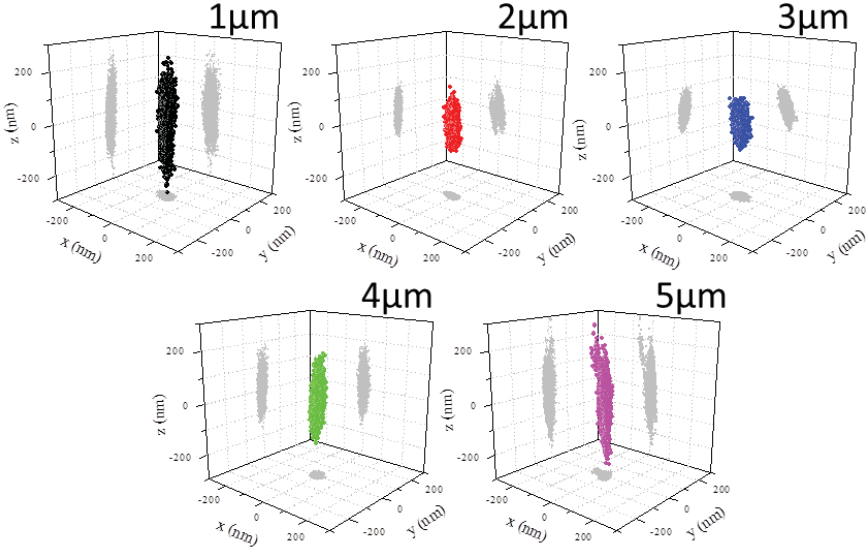
Figure 4.13: *Reconstruction of Brownian fluctuations of the trapped SiNWs for exemplar data sets from each sample. Each plot shows 10^4 points from the tracking signals in x, y, and z.*

corresponding ACF and obtained the relaxation frequencies, force, and torque constants. As an example, in fig. 4.12.b we show the measured axial relaxation frequencies ω_z measured for Si NWs of different length. Two sets of data points are distinguished corresponding to individual Si NWs and bundles of two Si NWs in the trap. The error bars on the length are extracted from the SEM images of the original samples, while the uncertainty on the relaxation rates represents the standard deviation from the mean. The functional behavior of relaxation frequencies with SiNWs length is the result of the interplay between optical trapping forces and hydrodynamics. By knowing the hydrodynamic damping for each Si NW we extrapolate the functional behavior of force and torque constants (as discussed later). Thus from these measurements, we get the full calibration of the optical confining potential. Figure 4.13 shows the reconstruction of Brownian motion of exemplar individual Si NW in the trap by sampling the calibrated tracking signals in x, y, and z. From each plot the transverse (fig. 4.14.a), axial (4.14.b), and angular (4.14.c) root mean square displacement (RMSD) are
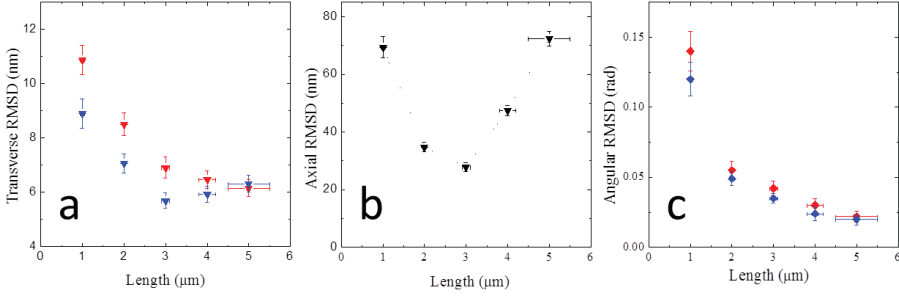
Figure 4.14: *Transverse (a) root-mean-squared-displacement (RMSD) for x- (red), y-direction (blue) and z-direction (b) as a function of length obtained from each data set shown in fig. 4.13. The observed monotonic RMSD decrease in (a) is consistent with the increase in trapping force. In contrast, in (b) the axial RMS along z has a more complex behavior accounting for the contrasting action of trapping and radiation pressure shift yielding a weaker trap for longer Si NW and hence larger positional fluctuations. (c) Angular RMSD as a function of length for fluctuations in the xz- (red) and yz-plane (blue). A larger length for the trapped Si NW results in a stronger optical torque and hence smaller angular fluctuations.*

obtained from the ACF zero point value, related to mean-squared-displacements $< X_i^2 >= k_B T/\gamma_i \omega_i$ and $< \Theta_j^2 >= k_B T/\gamma_\Theta \Omega_j$. The observed RMSD decrease in 4.14.a is consistent with an increase in trapping force. In contrast in 4.14.b the axial RMSD has a more complex behavior accounting for the contrasting action of increased trapping and larger radiation pressure shift yielding a weaker trap for longer Si NW and hence larger positional fluctuations. In 4.14.c angular RMSD decreases at larger lengths as a consequence of a stronger optical torque. Optical trapping forces generate from the conservation of momentum in the scattering process of light by a particle [166, 156, 186, 187, 188]. In a light scattering process by a thin Si NW we have two size scaling parameters defined by its transverse size and length as $x_d = \pi n d/\lambda \ll 1$ ($x_d \approx 0.05$, constant for each Si NW sample) and $x_L = \pi n L/\lambda > 1$ (varies in the range 5-25 for our SiNW samples), where n is the refractive index of the surrounding medium. The latter size parameter, x_L, regulates the interaction between Si NWs and radiation fields in the far-field. We

then plot in fig. 4.15 the measured optical force and torque constants and trap parameters as a function of the size parameter x_L. In particular, in fig. 4.15.a-d we show the scaling of the measured force and torque constants for individual Si NWs (solid symbols) and bundles of 2 Si NWs (open symbols). Force constants, k_x (fig. 4.15.a) and k_y (fig. 4.15.b), measured in the transverse plane are in the range 30-100 pN/μm for the longest Si NWs and are more than 1 order of magnitude larger than the ones measured along the propagation (z-)axis, k_z (fig. 4.15.c). Transverse optical forces show a flattening for longer Si NWs. This is expected [188] when the length is much larger than the Rayleigh range of the focal spot, since the interaction region is approximately the same for all Si NWs and the trapping force should not change dramatically with length. However, the scattering force increases for longer Si NWs pushing and shifting the trapped particles along the propagation axis in regions of the beam where light intensity and the axial trapping are weaker. This justifies the more complex behavior of k_z shown in fig. 4.15.c: the axial trapping force increases with size parameter x_L up to a maximum and then decreases for longer Si NWs. In contrast, measured torque constants (fig. 4.15.d) k_{Θ_x} and k_{Θ_y} show a monotonic increase with size parameter, that is, the longer the Si NWs length the stronger the optical torque on the nanowire. A linear polarized tightly focused laser beam has an anisotropic intensity profile in the focal plane as well as an intrinsic nonunitary aspect ratio of the spot because of light propagation [166, 156]. This yields asymmetries in the confining potential transverse plane and aspect ratio when trapping submicrometer or nonspherical particles [166, 167, 157, 158, 159, 160, 161]. This is quantified by two parameters: the trap polarization anisotropy, $k_P = 1 - k_x/k_y$, and trap aspect ratio, $(k_x + k_y)/2k_z$, that summarize the effects on optical forces from light polarization, propagation, and particle shape. Figures 4.15.e and 4.15.f show the scaling behavior of the polarization anisotropy and trap aspect ratio with the Si NW size parameter. In particular the polarization anisotropy, related to the nanometric transverse size [166, 159] of the Si NWs, appears to be constant, $k_P \approx 0.25$, over the range of length explored. Instead the trap aspect ratio shows a more complex scaling behavior that is related to the large anisotropy of the Si NWs combined with the
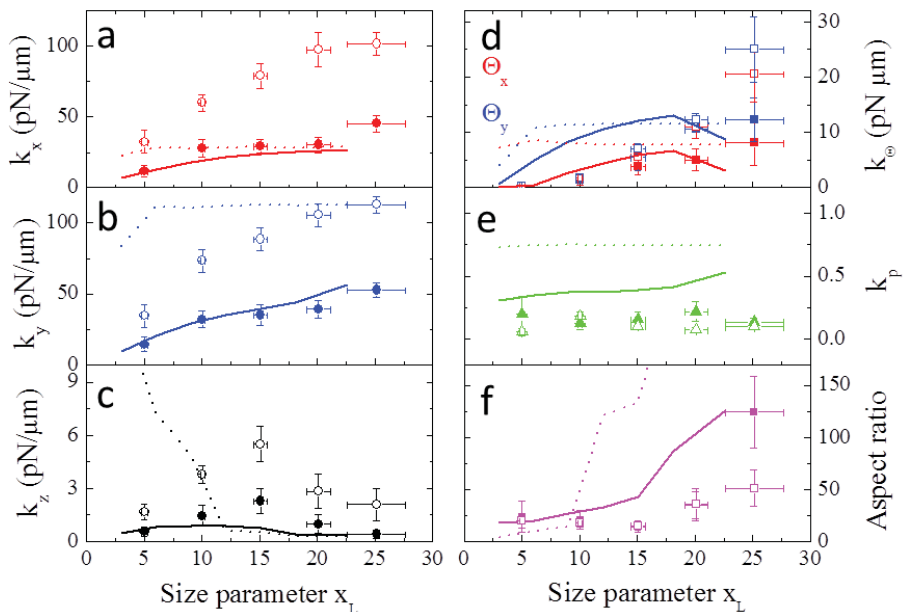
Figure 4.15: *Scaling of the measured force and torque constants and trap parameters as a function of the size parameter $x_L = n\pi L/\lambda$ for individual Si NWs (solid symbols) and bundles (open symbols). Force constants, k_x (a) and k_y (b), measured in the transverse plane are more than ten times larger than the ones measured along the propagation (z-)axis, k_z (c). (d) Torque constants k_{Θ_x} (red symbols) and k_{Θ_y} (blue symbols). (e) Polarization anisotropy, $k_P = 1 - (k_x/k_y)$, and (f) aspect ratio, $(k_x + k_y)/2k_z$, of the optical trap. The lines are the calculated values of optical force and torque constants and trap parameters for linear particles modeled as chains of small spheres trapped in an ideal diffraction limited laser spot with no aberration (dotted lines) and in a radiation field aberrated (solid lines) by the glasswater interface of the sample chamber. The theoretical lines have been scaled by only one free parameter in the plots (a-d), while no adjustment was made for the plots (e,f).*

shift of the trapping position by the scattering force. We now compare our experimental findings with optical trapping calculations based on electromagnetic scattering theory in the T-matrix formalism [166, 156]. The Si NWs are modeled as linear chains of length L composed of identical spheres of diameter $D \ll \lambda < L$ with the refractive index of bulk silicon, $n_{Si} = 3.7$ at 830 nm. Since the light scattering properties in the far-field are regulated by L, we expect our model to be able to account for a general scaling behavior of optical forces and torques despite the other structural differences at the nanoscale. In fig. 4.15, the lines are the calculated values of optical force and torque constants and trap parameters for model chains of small (D = 30 nm) spheres trapped in an ideal diffraction limited laser spot with no aberration (dotted lines) and in a radiation field that include the aberration (solid line) by the glasswater interface [156] of the sample chamber that blurs the laser spot at the distance where experiments are performed (about 15 μm). The theoretical lines have been scaled by only one free parameter in the plots (a-d) that accounts for the structural differences between the model linear chains [166] and the cylindrically shaped nanowires [188] used in the experiments, while no adjustment was made for the plots of fig. 4.15.e,f), whose parameters are obtained through ratios of measured force constants. The theoretical predictions for transverse force (fig. 4.15.a,b) and torque (fig. 4.15.d) constants in the ideal non aberrated case (dotted lines) show a sharp crossover at size parameter $x_L \approx 5$ from a monotonic increase with length to constant values. However, when aberration is taken into account (solid lines) the theoretical curves agree much better with measured values despite the simplified linear chain model structure used in the calculations. Similarly for the polarization anisotropy (fig. 4.15.e) and trap aspect ratio (fig. 4.15.f) including aberration effects in the calculations gives a better quantitative agreement with experimental findings with no free parameter. This shows how the Si NWs anisotropy plays a special role in defining the optical trapping potential yielding highly elongated traps with aspect ratios that range from 10 to 100.

Conclusions

In conclusion, Si NWs with transverse size of 7± 2 nm and controlled length in the micrometer range have been optically trapped. Such large aspect ratio ensures stable optical trapping of individual Si NWs over thermal fluctuations with transverse optical force constants of the order of 50 and 1-2 pN/μm for the axial ones, as well as granting spatial resolution of the order of tens of nanometers in photonic force microscopy applications. We have shown how length regulates optical forces, optical torques, and their Brownian dynamics in the trap. Correlation function analysis has been used to obtain the force and torque constants, root-mean-square translational and angular displacements, as well as relevant trap parameters. We compared them with calculations on model linear nanoparticles based on electromagnetic scattering theory showing that aberration plays a key role in experiments. Optical trapping of Si NWs with transverse size of a few nanometers opens perspectives for their use as nanoprobes with increased spatial and force resolution in photonic force microscopy applications [157, 168, 169, 185], as well as in protocols for laser cooling their center-of-mass and angular motion at the quantum regime in optical traps or cavities in vacuum.

Bibliography

[1] J. D. Meindl et al. - Limits on silicon nanoelectronics for terascale integration - Science (2001) vol. 293 p. 2044

[2] J. R . Heath et al - A defect-tolerant computer architecture: Opportunities for nanotechnology - Science (1998) vol. 280 p. 1716

[3] A. Javey et al. - Layer-by-layer assembly of nanowires for three-dimensional, multifunctional electronics - Nano Letters (2007) vol. 7 p. 773

[4] O. Hayden et al. - Nanoscale avalanche photodiodes for highly sensitive and spatially resolved photon detection - Nature Materials (2006) vol. 5 p. 352

[5] K. Fischer et al. - Biomimetic nanowire coatings for next generation adhesive drug delivery systems - Nano Letters (2009) vol. 9 p. 716

[6] Z. Li et al. - Sequence-specific label-free DNA sensors based on silicon nanowires - Nano Letters (2004) vol. 4 p 245

[7] M. D. Kelzenberg et al. - Photovoltaic measurements in single-nanowire silicon solar cells - Nano Letters (2008) vol 8 p. 710

[8] D. K. Kim et al. - Spinel $LiMn_2O_4$ nanorods as lithium ion battery cathodes - Nano Letters (2008) vol. 8 p. 3948

[9] R. G. Hobbs et al. - Semiconductor nanowire fabrication by bottom-up and top-down paradigms - Chemistry of Materials (2012) vol. 24 p. 1975

[10] M. Law et al. - Semiconductor nanowires and nanotubes- Annual reviews in materials research (2004) vol 34 p. 83

[11] L. Cademartiri et al. - Ultrathin nanowires: a materials chemistry perspective - Advanced Materials - (2009) vol. 21 p. 1013

[12] H. J. Fan - Semiconductor nanowires: from self-organization to patterned growth - Small (2006) vol. 2 p. 700

[13] R. Wagner et al. - Vapour-liquid-solid mechanism of single crystal growth - Applied Physics Letters (1964) vol. 4, p. 89

[14] J. D. Holmes et al. - Control of thickness and orientation of solution-grown silicon nanowires - Science (2000) vol. 287 p. 1471

[15] E. Dailey et al. - "Seedless" vapor-liquid-solid growth of Si and Ge nanowires: the origin of bimodal diameter distributions - Journal of Applied Physics (2009) vol. 105 p. 064317

[16] T. Shimizu et al. - Synthesis of vertical high-density epitaxial Si(100) Nanowire Arrays on a Si(100) substrate using an anodic aluminum oxide template - Advanced Materials (2007) vol. 19 p. 917

[17] K. Tomioka et al. - Control of InAs nanowire growth directions on Si - Nano Letters (2008) vol. 8 p. 3475

[18] R. Calarco et al. - Size-dependent photoconductivity in MBE-grown GaN nanowires - Nano Letters (2005) vol. 5 p. 981

[19] S. Walavalkar et al. - Tunable visible and near-IR emission from sub-10 nm etched single-crystal Si nanopillars - Nano Letters (2010) vol. 10 p. 4423

[20] S. Barth et al.- Defect transfer from nanoparticles to nanowires - Nano Letters (2011) vol. 11 p. 1550

[21] H. Y. Tuan et al. - Germanium nanowire synthesis: an example of solid-phase seeded growth with nickel nanocrystals - Chemistry of Materials (2005) vol. 17 p. 5705

[22] C. Chèze et al. - Collector phase transitions during vapor−solid−solid nucleation of GaN Nanowires - Nano Letters (2010) vol 10 p. 3426

[23] R. Q. Zhang et al. - Oxide-assisted growth of semiconducting nanowires - Advanced Materials (2003) vol. 15 p. 635

[24] B. A. Wacaser - Preferential Interface Nucleation: An Expansion of the VLS Growth Mechanism for Nanowires - Advanced Materials (2009) vol. 21 p. 153

[25] L. Schubert et al. - Silicon nanowhiskers grown on (111)Si substrates by molecular beam epitaxy - Applied Physics Letters (2004) vol. 84 p. 4968

[26] A. Irrera et al. - Control of growth mechanisms and orientation in epitaxial Si nanowires grown by electron beam evaporation - Nanotechnology (2009) vol. 20 p. 135601

[27] S. Kukushkin et al. - New phase formation on solid surfaces and thin film condensation - Progress in Surface Science (1996) vol 51, p. 1

[28] V. Dubrovskii et al. - Growth kinetics and crystal structure of semiconductor nanowires - Physical Review B (2008) vol. 78 p. 235301

[29] V. Sivakov et al.- Silicon nanowire growth by electron beam evaporation: kinetic and energetic contributions to the growth morphology - Journal of Crystal Growth (2007) vol. 300 p. 288

[30] N. D. Zakharov et al. - Growth phenomena of Si and Si/Ge nanowires on Si (111) by molecular beam epitaxy - Journal of Crystal Growth (2006) vol. 290 p. 6

[31] P. Artoni et al. - Kinetics of Si and Ge nanowires growth through electron beam evaporation - Nanoscale Research Letters (2011) vol. 6 p. 162

[32] Y. Wu et al. - Controlled growth and structures of molecular-scale silicon nanowires - Nano Letters (2004) vol. 4 p. 433

[33] T. Y. Tan et al. - On the thermodynamic size limit of nanowires grown by the vapor-liquid-solid process - Applied Physics A (2004) vol. 78 p. 519

[34] W. Lu et al. - One-dimensional hole gas in germanium/silicon nanowire heterostructures - Proceedings in National Academic Science U.S.A. (2005) vol. 102 p. 10046.

[35] B. M. Kayes et al. - Growth of vertically aligned Si wire arrays over large areas ($> 1cm^2$) with Au and Cu catalysts- Applied Physics Letters (2007) vol. 91 p. 103110.

[36] E. I. Givargizov - Fundamental aspects of VLS growth, Journal of Crystal Growth (1975) vol. 31 p. 20

[37] R. Duffy et al. - The curious case of thin-body Ge crystallization - Applied Physics Letters (2011) vol. 99 p. 131910

[38] E. F. Pecora et al. - Ion beam-induced bending of silicon nanowires - Physica E (2012) vol. 44 p. 1074

[39] C. Yang et al. - Encoding electronic properties by synthesis of axial modulation-doped silicon nanowires - Science (2005) vol. 310 p. 1304

[40] E. Koren et al. - Measurement of active dopant distribution and diffusion in individual silicon nanowires - Nano Letters (2010) vol. 10 p. 1163

[41] K. Bradley et al. - Influence of mobile ions on nanotube based FET devices - Nano Letters (2003) vol. 3 p 639

[42] M. Den Hertog et al. - Control of gold surface diffusion on si nanowires - Nano Letters (2008) vol. 8 p. 1544

[43] J. V. Wittemann et al. - Silicon nanowires: a review on aspects of their growth and their electrical properties - Advanced Materials (2009) vol. 21 p. 2681

[44] A. T. Heitsch et al. - - Journal of the American Chemical Society (2008) vol. 130 p. 5436

[45] Y. Wang et al. - Epitaxial growth of silicon nanowires using an aluminium catalyst - Nature Nanotechnology (2006) vol. 1 p. 186

[46] A. R. Guichard et al. - Temperature-dependent Auger recombination dynamics in luminescent silicon nanowires - Pysical Review B (2008) vol. 78 p. 235422

[47] A. R. Guichard et al. - Tunable light emission from quantum-confined excitons in $TiSi_2$ - catalyzed silicon nanowires - Nano Letters (2006) vol. 6 p. 2140

[48] P. Hashemi et al. - Gate-all-around silicon nanowire MOSFETs: top-down fabrication and transport enhancement techniques - Massachusetts Institute of Technology: Cambridge, MA (2010) p. 117

[49] I. Sychugov et al. - Sub-10 nm crystalline silicon nanostructures by electron beam induced deposition lithography - Nanotechnology (2010) vol. 21 p. 285307

[50] A. J. Bourdillon et al. - Near field x-ray lithography simulations for printing fine bridges - Journal of Physics D: Applied Physics (2003) vol. 36 p. 2471

[51] A. A. Talin et al. - Large area, dense silicon nanowire array chemical sensors - Applied Physics Letters (2006) vol. 89 p. 153102

[52] J. K. W. Yang et al. - Understanding of hydrogen silsesquioxane electron resist for sub-5-nm-half-pitch lithography - Journal of Vacuum Science and Technology B (2009) vol. 27 p. 2622

[53] M. Henry et al.- Alumina etch masks for fabrication of high-aspect-ratio silicon micropillars and nanopillars - Nanotechnology (2009) vol. 20 p. 4

[54] H. I. Liu et al. - Self limiting oxidation for fabricating sub 5 nm silicon nanowires - Applied Physics Letters (1993) vol. 64 p. 1383

[55] Wu, C. S.; Makiuchi, Y.; Chen, C. In Lithography; Wang, M., Ed.; Intech: Vukovar, 2010; pp 241−266.

[56] H. Chen et al. - Wafer-scale synthesis of single-crystal zigzag silicon nanowire arrays with controlled turning angle - Nano Letters (2010) vol. 10 p. 864

[57] S. G. Cloutier et al. - Enhancement of radiative recombination in silicon via phonon localization and selection rule breaking - Advanced Materials (2006) vol. 18 p. 841

[58] J. de Boor et al. - Sub-100 nm silicon nanowires by laser interference lithography and metal-assisted etching.- Nanotechnology (2010) vol. 21 p. 095302

[59] W. K. Choi et al. - Synthesis of silicon nanowires and nanofin arrays using interference lithography and catalytic etching- Nano Letters (2008) vol. 8 p. 3799

[60] A. Irrera et al. - Quantum confinement and electroluminescence in ultrathin silicon nanowires fabricated by a maskless etching technique - Nanotechnology (2012) vol. 23 p. 075204

[61] Z. Huang et al. - Metal-assisted chemical etching of silicon: a review - Advanced Materials (2011) vol. 23 p. 285

[62] D. D. Malinovska et al. - Preparation of thin porous silicon layers by stain etching - Thin Solid Films (1997) vol. 297 p. 9

[63] X. Li et al. - Metal-assisted chemical etching in HF/HO produces porous silicon - Applied Physics Letters (2000) vol. 77 p. 2572

[64] Y. Harada et al. - Catalytic amplification of the soft lithographic patterning of Si. Nonelectrochemical orthogonal fabrication of photoluminescent porous Si pixel arrays - Journal of the American Chemical society (2001) vol. 123 p. 8709

[65] K. Tsujino et al. - Helical nanoholes bored in silicon by wet chemical etching using platinum nanoparticles as catalyst - Electrochemical and Solid State Letters (2005) vol. 8 p. C193

[66] V. Lehmann - Electrochemistry of silicon: instrumentation, science, materials, and applications - (2002) Wiley-VCH

[67] Chattopadhyay et al. - In-plane control of morphology and tunable photoluminescence in porous silicon produced by metal-assisted electroless chemical etching - Journal of Applied Physics (2002) vol. 91 p. 6134

[68] K. Q. Peng et al. - Fabrication of single crystalline silicon nanowires by scratching a silicon surface with catalytic metal particles - Advanced Functional Materials (2006) vol.16 p. 387

[69] K. Q. Peng et al. - Metal-particle-induced, highly localized site-specific etching of Si and formation of single-crystalline Si nanowires in aqueous fluoride solution - Chemistry European Journal (2006) vol. 12 p. 7942

[70] K. Q. Peng et al. - Simultaneous gold deposition and formation of silicon nanowire arrays - Journal of Electroanalitic Chemostry (2003) vol. 558 p. 35

[71] Y. Xiu et al. - Hierarchical silicon etched structures for controlled hydrophobicity/superhydrophobicity - Nano Letters (2007) vol. 7 p. 3388

[72] Z. P. Huang et al. - Fabrication of silicon nanowire arrays with controlled diameter, length, and density - Advanced Materials (2007) vol. 19 p. 744

[73] Z. P. Huang et al. - Ordered arrays of vertically aligned [110] silicon nanowires by suppressing the crystallographically preferred [100] etching directions - Nano Letters (2009) vol. 9 p. 2519

[74] S. W. Chang et al. - Metal-catalyzed etching of vertically aligned polysilicon and amorphous silicon nanowire arrays by etching direction confinement - Advanced Materials (2009) vol. 19 p. 2495

[75] N. Geyer et al. - Sub-20 nm Si/Ge superlattice nanowires by metal-assisted etching - Nano Letters (2009) vol. 9 p. 3106

[76] Z. P. Huang et al. - Extended arrays of vertically aligned sub-10 nm diameter [100] Si nanowires by metal-assisted chemical etching - Nano Letters (2008) vol. 8 p. 3046

[77] H. Masuda et al. - Ordered metal nanohole arrays made by a two-step replication of honeycomb structures of anodic alumina - Science (1995) vol. 268 p. 1466

[78] D. E. Carlson et al. - Amorphous silicon solar cell - Applied Physics Letters (1976) vol. 28 p. 671

[79] J. Meier et al. - Complete microcrystalline p|i|n solar cell - crystalline or amorphous cell behavior? - Applied Physics Letters (1994) vol. 65 p. 860

[80] M. Shao et al. - Nitrogen-doped silicon nanowires: synthesis and their blue cathodoluminescence and photoluminescence - Applied Physics Letters (2009) vol. 95 p. 143110

[81] V. Sivakov et al. - Roughness of silicon nanowire sidewalls and room temperature photoluminescence - Physical Review B (2010) vol. 82 p. 125446

[82] H. D. Fuchs et al. - Porous silicon and siloxene: Vibrational and structural properties - Physical Review B (1993) vol. 48 p. 8172

[83] B. M. Kayes et al. - Comparison of the device physics principles of planar and radial p-n junction nanorod solar cells - Journal of Applied Physics (2005) vol. 97 p. 114302

[84] E. C. Garnett et al. - Silicon Nanowire Radial p-n Junction Solar Cells - Journal of the American Chemical Society (2008) vol. 130 p. 9224

[85] E. D. Kosten et al. - Ray optical light trapping in silicon microwires: exceeding the n^2 intensity limit - Optics Express (2011) vol. 19 p. 3316

[86] M. D. Kelzenberg et al. - Enhanced absorption and carrier collection in Si wire arrays for photovoltaic applications - Nature Materials (2010) vol. 9 p. 239

[87] D. M. Callahan et al. - Solar cell light trapping beyond the ray optic limit - Nano Letters (2012) vol. 12 p. 214

[88] Z. Li et al. - Sequence-specific label-free DNA sensors based on silicon nanowires - Nano Letters (2004) vol. 4 p. 245

[89] Y. Engel et al. - Supersensitive detection of explosives by silicon nanowire arrays - Angewandte Chemie International Edition (2010) vol. 49 p. 6830

[90] J. Goldberger et al. - Silicon vertically integrated nanowire field effect transistors - Nano Letters (2006) vol. 6 p. 973

[91] C. Huber et al. - Nanowire array composites - Science (1994) vol. 263, p. 800

[92] E. Yablonovitch et al.- Auger recombination in silicon at low carrier densities - Applied Physics Letters (1986) vol. 49 p. 587

[93] L. T. Canham et al. - - Applied Physics Letters (1990) vol. 57 p. 1046

[94] S. Ossicini, L. Pavesi, F. Priolo - Light emitting silicon for microphotonics - Springer (2004)

[95] A. G. Cullis et al. - The structural and luminescence properties of porous silicon - Journal of Applied Physics (1997) vol. 82 p. 909

[96] L. Pavesi et al. - Optical gain in silicon nanocrystals - Nature (2000) vol. 408 p. 440

[97] L. Lin et al. - Synthesis and photoluminescence properties of porous silicon nanowire arrays - Nanoscale Research Letters (2010) vol. 5 p. 1822

[98] K. Q. Peng et al. - Dendrite-assisted growth of silicon nanowires in electroless metal deposition - Advanced Functional Materials (2003) vol. 13 p. 127

[99]   B. Fazio et al. - Enhanced coherent raman backscattering from Si-nanowire fractal arrays - submitted (2012)

[100] K. Tzu et al. - Removing structural disorder from oriented TiO_2 nanotube arrays: reducing the dimensionality of transport and recombination in dye-sensitized solar cells - Nano Letters (2007) vol. 7 p. 3739

[101] H. Richter et al. - The one phonon Raman spectrum in micro-crystalline silicon - Solid State Communications (1981) vol. 39 p. 625

[102] I. H. Campbell et al. - The effects of microcrystal size and shape on the one phonon Raman spectra of crystalline semi-conductors - Solid State Communications (1986) vol. 58 p. 739

[103] S. Piscanec et al. - Raman spectroscopy of silicon nanowires - Physical Review B (2003) vol 68 p. 241312

[104] H. Zimmermann - Integrated Silicon Optoelectronics - New York, Springer (2000)

[105] R. N. Hall - Electron-hole recombination in germanium - Physical Review (1952) vol. 87 p. 387

[106] W. Shockley et al. - Statistics of the recombinations of holes and electrons - Journal of Physical Review (1952) vol. 87 p. 835

[107] D. Kovalev et al. - Breakdown of the k-conservation rule in Si nanocrystals - Physical Review Letters (1998) vol. 81 p. 2803

[108] B. Delley et al. - Quantum confinement in Si nanocrystals - Physical Review B (1993) vol. 47 p. 1397

[109] S. Furukawa et al. - Three-dimensional quantum well effects in ultrafine silicon particles - Japanese Journal of Applied Physics (1988) vol. 27 p. L2207

[110] V. Lehmann et al. - Porous silicon formation: a quantum wire effect - Applied Physics Letters (1991) vol. 58 p. 856

[111] S. Guha et al. - Visible light emission from Si nanocrystals grown by ion implantation and subsequent annealing - Applied Physics Letters (1997) vol. 70 p. 1207

[112] A. J. Kenyon et al. - Luminescence efficiency measurements of silicon nanoclusters - Applied Physics Letters (1998) vol. 73 p. 523

[113] S. Fukurawa et al. - Quantum size effects on the optical band gap of microcrystalline Si:H - Physical Review B: Condensed Matter Material Physics (1988) vol. 38 p. 5726

[114] M. L. Brongersma et al. - Tuning the emission wavelength of Si nanocrystals in SiO_2 by oxidation - Applied Physics Letters (1998) vol. 72 p. 2577

[115] H. Nishikawa et al. - Visible photoluminescence from Si clusters in γ irradiated amorphous SiO_2- Journal of Applied Physics (1996) vol. 80 p. 3513

[116] Y. Kanemitsu et al. - Photoluminescence from Si/SiO_2 single quantum wells by selective excitation - Physical Review B: Condensed Matter Material Physics (1997) v. 56 p. 15561

[117] A. Irrera PhD thesis - Light emitting devices based on Si nanostructures (2004) - University of Catania

[118] L. Canham - A glowing future for silicon: chips and circuits could work much faster if they used light to communicate with each other. Fragile layers of porous silicon could be just the thing to let them do it - New Scientist (1993) vol. 1868

[119] M. Shao et al. - Nitrogen-doped silicon nanowires: synthesis and their blue cathodoluminescence and photoluminescence- Applied Physics Letters (2009) vol. 95 p. 143110

[120] O. Demichel et al. - Recombination Dynamics of Spatially Confined Electron-Hole System in Luminescent Gold Catalyzed Silicon Nanowires - Nano Letters (2009) vol. 9 p. 2575

[121] J. Valenta et al. - - Coexistence of 1D and Quasi-0D Photoluminescence from Single Silicon Nanowires - Nano Letters (2011) vol. 11 p. 3003

[122] L. Dal Negro et al. - Light emission efficiency and dynamics in silicon-rich silicon nitride films - Applied Physics Letters (2006) vol. 88 p. 233109

[123] F. Priolo et al. - Role of the energy transfer in the optical properties of undoped and Er-doped interacting Si nanocrystals - Journal of Applied Physics (2001) vol. 89 p. 264

[124] D. Kovalev et al. - Optical absorption cross sections of Si nanocrystals - Physical Review B (2000) vol. 61 p. 4485

[125] M. L. Brongersma et al. - Size-dependent electron-hole exchange interaction in Si nanocrystals - Applied Physics Letters (2000) vol. 76 p. 351

[126] P. D. J. Calcott et al. - Identification of radiative transitions in highly porous silicon - Journal of Physics: Condensed Matter (1993) vol. 5 p. L91

[127] V. Vinciguerra et al. - Quantum confinement and recombination dynamics in silicon nanocrystals embedded in Si/SiO2 superlattices - Journal of Applied Physics (2000) vol. 87 p. 8165

[128] M. Palummo et al. - Giant excitonic exchange splitting in Si nanowires: first principles calculations - Physical Review B (2010) vol. 81 p. 121303

[129] A. C. Dillon et al. - FTIR studies of water and ammonia decomposition on silicon surfaces - Journal Electron Spectroscopy and Related Phenomena (1990) vol. 54-55 p 1085

[130] M. S. Brandt et al. - The origin of visible luminescence from 'porous silicon': a new interpretation - Solid State Communications (1992) vol. 81 p. 307

158

[131] M. P. Van Albada - Observation of weak localization of light in a random medium - Physical Review Letters (1985) vol. 55 p. 2692

[132] P. E. Wolf et al. - Weak localization and coherent backscattering of photons in disordered media - Physical Review Letters (1985) vol. 55 p. 2696

[133] S. John - Localization and absorption of waves in a weakly dissipative disordered medium - Physical Review B (1985) vol. 31 p. 304

[134] D. S. Wiersma et al. - Localization of light in a disordered medium - Nature (1997) vol. 390 p. 671

[135] D. S. Wiersma - A random laser? - Nature (1995) vol. 373 p. 203

[136] D. S. Wiersma - Laser physics: the smallest random laser - Nature (2000) vol. 406 p. 132

[137] D. S. Wiersma - The physics and applications of random lasers - Nature Physics (2008) vol. 4 p. 359

[138] H. Cao et al. - Random laser action in semiconductor powder - Physical Review Letters (1999) vol. 82 p. 2278

[139] L. Cao et al. - Enhanced Raman scattering from individual semiconductor nanocones and nanowires - Physical Review Letters (2006) vol. 96 p. 1574021

[140] V. Poborchii - High near-ultraviolet Raman efficiency of silicon nanowires with small cross sections - Physical Review B (2011) vol. 83 p. 1534121

[141] L. Cao et al - Excitation of local field enhancement on silicon nanowires - Nano Letters (2008) vol. 8 p. 601

[142] J. A. Huang et al. - Enhanced Raman scattering from vertical silicon nanowires array - Applied Physics Letters (2011) vol. 98 p. 183108

159

[143] M. Walia et al. - Raman Enhancement from Arrays of etched silicon nanowires - Proceedings of the Advanced Photonics Congress OSA (2012) IW2C.7

[144] M. V. Shalaev et al. - Scattering and localization of light on fractals - Physica A (1992) vol. 191 p. 352-357

[145] P. De Vries et al. - Wave localization in disordered and fractal systems - Computer Physics Communications (1993) vol. 75 p. 298

[146] K. Mizuno et al. - A black-body absorber from vertically aligned single-walled carbon nanotubes - National Academy of Sciences USA (2009) vol. 106 p. 6044

[147] A. Kastler - The Raman effect and multiple scattering of light - Proceedings of Mathematical Science (1938) vol. 8 p. 476

[148] O. L. Muskens et al. - Large photonic strength of highly tunable resonant nanowire materials - Nano Letters (2009) vol. 9 p. 930

[149] E. Anastassakis et al. - . Angular dispersion of "backward" Raman scattering: Weakly absorbing cubic materials (Si) - Journal of Applied Physics (1985) vol. 57 p. 920

[150] A. E. Ioffe et al. - Non-crystalline, amorphous, and liquid electronic semiconductors - Progress in Semiconductors (1960) vol. 4 p. 237

[151] R.W. Hellwarth - Theory of stimulated raman scattering - Physical Review (1963) vol. 130 p. 1850

[152] R. W. Boyd - Non Linear Optics, 2nd edition - (2003) Academic Press, San Diego

[153] A. Ashkin et al. - Observation of a single-beam gradient force optical trap for dielectric particles - Optics Letters (1986) vol. 11 p. 288

[154] D. G. Grier - A revolution in optical manipulation - Nature (2003) vol. 424 p. 810

[155] K. Dholakia et al. - Optical manipulation - Chemical Society Review (2007) vol. 37 p. 42

[156] F. Borghese et al. - Optical trapping of non-spherical particles in the T-matrix formalism - Optics Express (2007) vol 15 p. 11984

[157] Y. Nakayama et al. - Tunable nanowire nonlinear optical probe - Nature (2007) vol. 447 p. 1098

[158] F. Dutto et al. - Nonlinear optical response in single alkaline niovate nanowires - Nano Letters (2011) vol. 11 p. 2517

[159] O. M. Maragò et al. - Femtonewton force sensing with optical trapped nanotubes - Nano Letters (2008) vol. 8 p. 3211

[160] A. A. R. Neves et al. - Rotational dynamics of optically trapped nanofibers - Optics Express (2010) vol. 18 p. 822

[161] O. M. Maragò et al. - Brownian motion of graphene - ACS Nano (2010) vol. 4 p. 7515

[162] L. Jauffred et al. - Three-dimensional optical control of individual quantum dots - Nano Letters (2008) vol. 8 p. 3376

[163] K. Svoboda et al. - Optical trapping of metallic Rayleigh particles - Optics Letters (1998) vol. 28 p. 930

[164] R. Agarwal et al. - Manipulation and assembly of nanowires with holographic optical traps - Optics Express (2005) vol. 13 p. 8906

[165] P. J. Pauzaskie et al. - Optical trapping and integration of semiconductor nanowire assemlies in water - Nature Materials (2006) vol. 5 p. 97

[166] F. Borghese et al. - Radiation force and torque on optically trapped linear nanostructures - Physical Review Letters (2008) vol. 100 p. 163903

[167] P. J. Reece et al. - Characterization of semiconductor nanowires based on optical tweezers - Nano Letters (2011) vol. 11 p. 2375

[168] D. M. Carberry et al. - Calibration of optically trapped nanotools - Nanotechnology (2010) vol. 21 p. 175501

[169] D. B. Phillips et al. - Surface imaging using holographic optical tweezers - Nanotechnology (2011) vol. 22 p. 285503

[170] D. V. Petrov - Raman spectroscopy and optically trapped particles - Journal of Optics A: Pure Applied Optics (2007) vol. 9 p. S139

[171] E. Messina et al. - Manipulation and raman spectroscopu with optically trapped metal nanoparticles obtained by pulsed laser ablation in liquids - Journal of Physical Chemistry C (2011) vol. 115 p. 5115

[172] R. Di Leonardo et al. - Three-dimensional to two dimensional crossover in the hydrodynamic interactions between micronscale rods - Physical Review Letters (2011) vol. 197 p. 044501

[173] C. H. Townes - How the laser Happened - Oxford University Press (1999) Oxford, U.K.

[174] A. Ashkin - Acceleration and trapping of particles by radiation pressure - Physical Review Letters (1970) vol. 24 p. 156

[175] A. Ashkin - Forces of a single-beam gradient laser trap on a dielectric sphere in the ray optics regime. Biophysics Journal (1992) vol. 61 p. 569

[176] J. Happel, H. Brenner - Low reynolds number hydrodynamics - Springer (1981) Berlin

[177] M. M. Tirado - Comparison of theories for the translational and rotational diffusion coefficients of rod-like macromolecules. Application to short DNA fragments - Journal of Physical Chemistry C (1984) vol. 81 p. 2047

[178] S. Broersma - Viscous force and torque constants for a cylinder - Journal of Chemical Physics (1981) vol. 74 p. 6989

[179] P. H. Jones et al. - Rotation detection in light-driven nanorotors - ACS Nano (2009) 3, 3077

[180] O. M. Maragò, P. H. Jones, P. G. Gucciardi - Photonic force microscopy: from femtonewton force sensing to ultra-sensitive spectroscopy. Scanning probe microscopy in nanoscience and nanotecnology - B. Bushan (2010) Springer-Verlag

[181] F. Borghese, P. Denti, R. Saija - Scattering from model non-spherical particles - 2nd ed. Springer (2007) Berlin

[182] B. Richards et al. - Electromagnetic diffraction in optical systems II. Structure of the image field in an aplanatic system - Proceedings in the Royal Society, London Ser. A (1959) vol. 253 p. 358

[183] R. Pfeifer et al. - Momentum of an Electromagnetic Wave in Dielectric MEdia - Review of Moder n Physics (2007) vol. 79 p. 1197

[184] L. Novotny, B. Hecht - Principles of nano-optics - Cambridge University Press (2006) New York

[185] A. Pralle et al. - Three dimensional high-resolution particles tracking for optical tweezers by forward scattered light - Microscopy Research Technology (1999) vol. 44 p. 378

[186] S. H. Simpson et al. - First-order nonconservative motion of optically trapped nonspherical particles - Physica Review E (2010) vol. 82 p. 031141

[187] W. Singer et al. - Orientation of optically trapped nonspherical birefringent particles - Physical Review E (2006) vol. 73 p. 021911

[188] P. B. Bareil et al. - Angular and position stability of a nanorod trapped in an optical tweezers - Optics Express (2010) vol 18 p. 26388

[189] H. L. Pecseli - Fluctuations in physical systems - Cambridge University Press (2000) Cambridge, U.K.

[190] Y. Zhu et al. - Mechanical properties of vapor liquid solid wynthesized silicon nanowires - Nano Letters (2009) vol. 9 p. 3934

[191] T. R. Dynamics of filmanets and membranes in a viscous fluid
     - Review of Modern Physics (2010) vol. 82 p. 1607

[192] G. Volpe et al. - Torque detection using brownian fluctuations
     - Physical Review Letters (2006) vol. 97 p. 210603

Acknowledgments

Sono molte le persone che desidero ringraziare per essermi state vicine in questi anni di dottorato, con le loro capacità, la loro amicizia e il loro affetto. Poter esprimere e concretizzare idee scientifiche in un ambiente stimolante è un'occasione che sfiora solo pochi fortunati. Certe cose, forse, si comprendono appieno soltanto quando, per la prima volta, si rischia di esserne allontanati. Desidero, prima di tutto, ringraziare le figure più importanti della mia crescita scientifica e intellettuale: il prof. Francesco Priolo, il mio relatore, e la dott.ssa Alessia Irrera, il mio supervisor. Entrambi, in questi anni, hanno curato la mia formazione, dimostrandosi determinanti per quest'ultima, e a loro devo dunque la più sincera gratitudine. Il prof. Priolo è stato un costante punto di riferimento sin dai lavori della tesi specialistica, mi ha offerto la possibilità di seguire questo corso di Dottorato, nonché - ed è la cosa più preziosa - di crescere in una realtà scientifica vivace e molto ben organizzata. La dott.ssa Irrera mi ha seguito scientificamente e ha saputo guidarmi con grande impegno, e con una dedizione che non è mai venuta meno in questi anni. E ancora un grazie va a Onofrio, Barbara e Matteo, per l'indispensabile supporto scientifico nel mondo dell'optical trapping e della spettroscopia, al dott. Iacona aver condiviso le sue competenze, alla dott.ssa Franzò per avermi offerto il suo aiuto e la sua esperienza in laboratorio di luminescenza, e a Simona per il suo aiuto e professionalità nel campo della microscopia. Un pensiero di amicizia e stima va a tutti i colleghi della stanza che, si sa, passano anno dopo anno, ma con i quali ci si ritrova sempre in chat pranzo... come Emanuele, che ringrazio per aver ascoltato pazientemente, nel primo anno di dottorato, le mie interpretazioni degli esperimenti, a volte troppo naif;

e poi ancora Maria, con cui ho condiviso curiosità scientifiche, e Roberto, con il quale abbiamo sorriso spesso e volentieri del "Presidente". E ancora ringrazio Paolo, con il quale ho affrontato spesso discussioni scientifiche e con il quale mi avrebbe fatto piacere collaborare. Un pensiero va a Gabriele e Piergiorgio, che sono stati non solo ottimi colleghi, ma anche preziosi coinquilini e amici. E poi ringrazio tutti coloro con i quali ho condiviso splendidi pranzi e tornei di pallavolo piuttosto impegnativi, come (sperando di non dimenticare nessuno) Vittorio, Isodiana, Salvo M., Salvo C., Paolo S., Giuliana, Stefano, Giorgia, Francesco P. e Francesco R., Egidio, Elena, Seweryn, Antonella, Valeria e Lucia, il prof. Terrasi e la prof.ssa Simone, la prof.ssa Grimaldi e il prof. Piccitto. Ringrazio anche il prof. Giuseppe Angilella, per l'aiuto datomi in questi anni oltre che per la sua simpatia. Un grazie sentito va anche ai miei amici di Augusta, come Sebastiano e Sara, Francesco e Alessia. Infine, un grazie importante va poi a tutta la mia famiglia, ai miei genitori, che hanno sempre stimolato i miei interessi e il mio amore per la ricerca, a mio fratello Cesare e mia sorella Marina, e alle loro famiglie, alle due nipotine che ormai si sono fatte grandi, ai miei zii, e a tutta la famiglia di Laura, i suoi genitori, il nonno, gli zii... che sento essere già la mia famiglia. E poi, un grazie enorme va a Lauretta mia, che mi è stata vicina ogni giorno e sempre lo sarà.

Curriculum Vitae

Pietro Artoni was born in Augusta (SR) in September 14th 1985, and is living in Via Volturno 39, Pisa

1. Education

a. achieved, on 2004, the high school diploma with grade 100/100;

b. achieved on 2007 the Bachelor Degree in Physics from the University of Catania with full marks 110/110 cum laude with a dissertation entitled: "From perovskites to ferroelectric memory devices" (supervisor: prof. Francesco Priolo);

c. achieved on 2009 the Master Degree in Physics with full marks 110/110 cum laude with a dissertation entitled: "Heteroepitaxy of Ge Nanowires on Silicon substrates by Electron Beam Evaporation" (supervisors: prof. Francesco Priolo, Alessia Irrera);

d. has been admitted to the International PhD courses in Nanoscience at the University of Catania on 2009 (declined);

e. has been admitted to the PhD courses in Physics at the University of Catania on 2009;

f. worked, since January 2010 to October 2012 at CNR-IMM-MATIS and at the University of Catania, as a PhD student in Physics.

g. worked, since December 2012 at NEST (Pisa), as a Postdoctoral Research Fellow.

4. Additional Skills

- Excellent knowledge of analysis and simulation software , and graphical data plot software including Origin 8.0 and earlier versions, Carine Cristallography, Gatan Digital Microscope;

- I Achieved European Computer Driving Licence in 2000;

- Excellent knowledge of Microsoft operating systems Windows 7 and earlier versions, and different Linux distributions;

- Excellent knowledge of Microsoft Office 2010 and OpenOffice software;

- Good knowledge of English (European Level B1 certified) and average knowledge of French.

5. Collaborations

Collaboration with the following istitutions:

- University of Catania, Dipartimento di Fisica e Astronomia, Catania, Italy

- CNR, IMM, MATIS, Catania, Italy

- CNR IPCF Messina, Italy

6. Participation to conferences, workshops and seminars:

- XXI AIRAPT and XLV EHPRG International Conference on High Pressure Science and Technology, at the department of Physics and Astronomy of Catania, September 17th-21th 2007;

- ENEL Research, workshop on "advanced solar lab", in Passo Martino (CT), September 14th 2007;

- International school on photovoltaics and renewable energies "Materials for renewable energies" in Erice, May 28th 2010 - June 2nd 2010;

- International conference EMRS Spring Meeting, Strasbourg, June 7th -11th 2010, presenting the poster "Structure and properties of nanowires grown by Germanum Electron Beam Evaporation" in the i

- International Workshop: "Nanowire Growth Workshop" held in Rome at the CNR, presenting the poster: "Bottom-up and top-down Approaches for group-IV semiconductor nanowires growth", November 4th -5th 2010;

- International conference MRS Spring Meeting, with an oral presentation of the work: "Metal Assisted Etching Silicon nanowires as Light Emitting Devices at Room Temperature ", held in San Francisco (USA), April 25th-29th 2011;

- International school in nano-optics held in Erice, July 3rd-18th 2011;

7. Other activities

- Working at Intel Corp. from September 2012 to November 2012, as a RTX process engineer;

- President of Archimedes Chapter of the Optical Society of America since June 2012;

- President of Catania Section of the Youngminds project sponsored by the European Physical Society since October 2011;

List of publications

This research has produced the following publications in international journals:

- E. F. Pecora, A. Irrera, P. Artoni, S. Boninelli, C. Bongiorno, C. Spinella, F. Priolo, *Heteroepitaxial growth and faceting of Ge nanowires on (111) Si by electron beam evaporation*, **Electrochemical and Solid State Letters** 13, K53-K55 (2010);

- P. Artoni, E. F. Pecora, A. Irrera, F. Priolo, *Kinetics of Si and Ge Nanowires Growth through Electron Beam Evaporation*, **Nanoscale Research Letters** 6, 162 (2011);

- A. Irrera, P. Artoni, R. Saija, P. G. Gucciardi, M. A. Iatì, F. Borghese, P. Denti, F. Iacona, F. Priolo, O. M. Maragò, *Size-Scaling in Optical Trapping of Silicon Nanowires*, **Nano Letters** 11, 4879 (2011);

- A. Irrera, P. Artoni, F. Iacona, E. F. Pecora, G. Franzò, F. Priolo, *A silicon nanowire light emitting device*, **Nanotechnology** 23, 075204 (2012);

- P. Artoni, A. Irrera, E. F. Pecora, S. Boninelli, C. Spinella, F. Priolo, *Heteroepitaxial growth of Ge nanowires on Si substrates*, **International Journal of Photoenergy** 782835 (2012);

- P. Artoni, A. Irrera, F. Iacona, E. F. Pecora, G. Franzò, F. Priolo, *Temperature dependence and aging effects on silicon nanowires photoluminescence*, **Optics Express** 20, 1483-1490 (2012);

- E. F. Pecora, N. Lawrence, P. Gregg, J. Trevino, P. Artoni, A. Irrera, F. Priolo and L. Dal Negro, *Nanopatterning of silicon nanowires for enhancing visible photoluminescence*, **Nanoscale** 4, 2863 (2012)

- B. Fazio, A. Irrera, M. Galli, P. Artoni, C. D'Andrea, P. G. Guc-

ciardi, M. Patrini, C. S. Vasi and F. Priolo - *Coherent enhanced Raman backscattering from Si-nanowires fractal arrays*, Submitted (2012)